INTERFACIAL FRACTURE OF MICRO THIN FILM INTERCONNECTS UNDER MONOTONIC AND CYCLIC LOADING

A Dissertation
Presented to
The Academic Faculty

by

Jiantao Zheng

In Partial Fulfillment
of the Requirements for the Degree
Doctor of Philosophy in the
School of Mechanical Engineering

Georgia Institute of Technology
December, 2008

INTERFACIAL FRACTURE OF MICRO THIN FILM INTERCONNECTS UNDER MONOTONIC AND CYCLIC LOADING

Approved by:

Dr. Suresh K. Sitaraman, Advisor
School of Mechanical Engineering
Georgia Institute of Technology

Dr. Rao Tummala
School of Electrical and Computer Engineering
Georgia Institute of Technology

Dr. Levent Degertekin
School of Mechanical Engineering
Georgia Institute of Technology

Dr. Zhong Lin Wang
School of Material Science and Engineering
Georgia Institute of Technology

Dr. David McDowell
School of Mechanical Engineering
Georgia Institute of Technology

Dr. Gilroy J. Vandentop
Components Research
Intel Corp.

Date Approved: November 13, 2008

To my wife, my parents, and my brother

Their endless love and support make my dream come true.

ACKNOWLEDGEMENTS

It is such a long and eventful journey for me to reach this point. I would like to acknowledge all the people who helped me along the way.

I give my deepest gratitude to my advisor, Dr. Suresh Sitaraman, for giving me the opportunity to work under his guidance and placing in me the faith and trust that I would succeed.

I would like to thank my committee members, Dr. Levent Degertekin, Dr. David McDowell, Dr. Rao Tummala, Dr. Gilroy J. Vandentop, and Dr. Z. L. Wang, for their valuable time, insights, guidance, and constructive criticism.

I would like to thank all the cleanroom staff who trained me to use all the state-of-art equipments for this research. In particular I want to thank Devin Brown and Raghunath Murali for their training on E-beam lithography, and Ms. Yolande Berta in the Department of Material Science to help me to use the LEO SEM to image nano scale structures.

Thanks to all the CASPaR members, past and present, for their support and I am grateful to have been part of such a brilliant team. In particular, I would like to thank Kevin Klein, Jamie Ahmad, Gregory Ostrowicki, Mitul Modi, Raghuram Pucha, Karan Kacker, Krishna Tunga, Andrew Perkins, KJ Lee, George Lo and Nicholas Ginga for their wisdom, friendship, and professional contribution.

In addition, I would like to acknowledge the financial support from PRC, NSF (award #: CMS-0510211 and CMMI-0800037) and Georgia Tech, all who in part funded

this research. Also, I would like to thank Intel for equipment donations for supporting this research.

I feel deeply indebted to my wife, Mei. I want to give her my heartfelt gratitude. Because of her no ending love and support, I was able to appreciate this process to the fullest and have the strength necessary to conquer any obstacle it presented.

Finally, I would like to thank my parents Xiulian Gao and Xiangwen Zheng, and my brother Jianru Zheng, for standing by my side and giving me all the love and support in the pursuit of my Ph.D. degree.

TABLE OF CONTENTS

LIST OF TABLES

LIST OF FIGURES

SUMMARY

The goal of this research was to develop new experimental techniques to quantitatively study the interfacial fracture of micro-contact thin film interconnects used in microelectronic applications under monotonic and cyclic loadings. The micro-contact spring is a new technology that is based on physical vapor deposited thin film cantilevers with a purposely-imposed stress gradient through the thickness of the film. These "springs" have the promise of being the solution to address near-term wafer level probing and long-term high-density chip-to-next level microelectronic packaging challenges, as outlined by the International Technology Roadmap for Semiconductors. The success of this technology is, in part, dependent on the ability to understand the failure mechanism under monotonic and cyclic loadings. This research proposes two experimental methods to understand the interfacial fracture under such monotonic and cyclic loading conditions.

To understand interfacial fracture under monotonic loading, a fixtureless superlayer-based delamination test has been developed. Using stress-engineered Cr layer and a release layer with varying width, this test can be used to measure interfacial fracture toughness under a wide range of mode mixity. This test uses common IC fabrication techniques and overcomes the shortcomings of available methods. The developed test has been used to measure the interfacial fracture toughness for Ti/Si interface. It was found that for low mode mixity Ti/Si thin film interfaces, the fracture toughness approaches the work of adhesion which is essentially the Ti-Si bond energy for a given bond density. In addition to the monotonic decohesion test, a fixtureless fatigue test is developed to investigate the interfacial crack propagation. Using a ferromagnetic

material deposited on the micro-contact spring, this test employs an external magnetic field to be able to drive the interfacial crack. Fatigue crack growth can be monitored by E-beam lithography patterned metal traces that are 10 to 40nm wide and 1 to a few μm in spacing. The crack initiation and propagation can be monitored through electrical resistance measurement. In the conducted experiments, it is seen that the interfacial delamination does not occur under cyclic loading, and that the micro-contact springs are robust against interfacial fracture for probing and packaging applications. It is also seen that the developed test technique has the potential to characterize interfacial fracture parameters under cyclic loading for a wide range of metal/dielectric material systems.

CHAPTER 1

INTRODUCTION AND LITERATURE REVIEW

1.1 Introduction and Background

Flip Chip On Board (FCOB) technology is one of the most attractive options to meet the high performance IC needs of the next decade and beyond. Compared to wiring bonding and tape automatic bonding, the advantages of FCOB are: higher I/O density, shorter leads, lower inductance, higher frequency, better noise control, smaller device footprint, and lower cost.

Typically FCOB interconnects are formed using eutectic solders. One major challenge for FCOB is that the shorter stand off height of such interconnects would decrease the reliability driven by thermomechanical fatigue between the silicon chip and the chip carrier. At the same time a probing technology also needs to be developed that can test the high I/O densities of the near and long term future.

A new technology called “micro contact springs” that could potentially resolve the thermal-mechanical fatigue problem and the probing need have been developed by researchers at Georgia Institute of Technology, NanoNexus, Inc., and Palo Alto Research Center (PARC). This technology is based on "springs", which are sputter deposited thin films with a purposely-imposed stress gradient through the thickness of the film. Figure 1.1 shows an example of the high-density pitch achieved by this technology.

The predominant benefits of this technology are: (1) batch processing of the interconnects at the wafer level, (2) photolithography allows any possible layout and arrangement of micro-contact spring fingers and any tip shape, (3) micro-contact springs

deformation is within their elastic regime, and (4) use conventional IC production facilities.

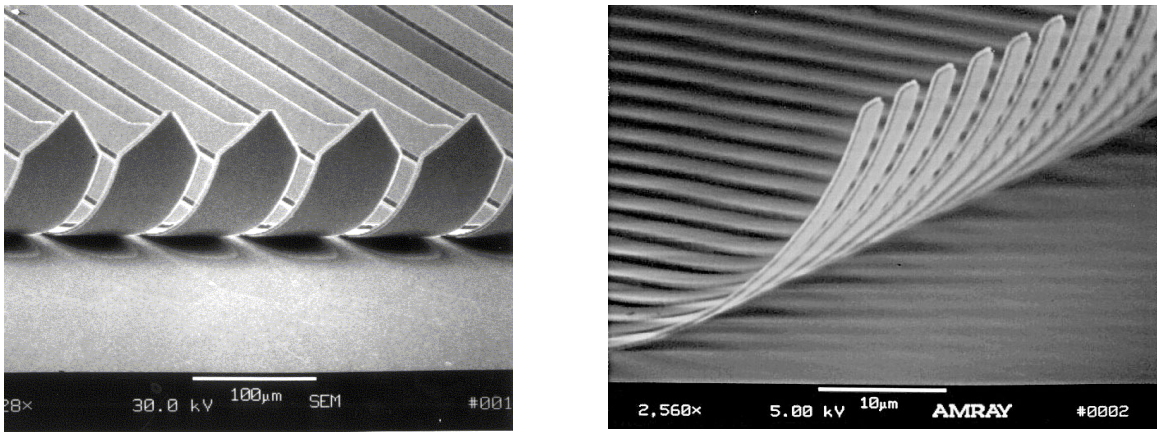

Figure1.1 Micro-contact springs at (a) 80 µm pitch and (b) 6 µm pitch [1]

When fabricated on a substrate, these interconnects become probes for wafer level packaging test and burn-in applications. Introduction of the micro-contact spring into the commercial market has already been achieved in the application of probers.

External forces during probing and packaging increase the likelihood for interfacial delamination and fracture of the springs. Issues of local plastic deformation, large displacement, various interface metallurgies, and other complexities suggest the need to understand how to measure and prevent fracture in micro-contact springs during fabrication, probing, and packaging.

To study the interfacial delamination and fracture of the micro contact springs is one purpose of this research. The methods developed are generic to many micro and nano scale thin film applications. Some of the applications are: solid-state devices, integrated electronic components, sensors, MEMS/NEMS, nanocomposite hard thin-films

in mechanical components for wear and abrasion resistance, anti-reflective optical films for better light transmission, conductive films in display technologies, thin-film coating in solar cells, magnetic coatings for media storage, and flexible and bendable lenses for space exploration.

There are more than one hundred different methods for measuring interfacial fracture toughness of thin film interface [2]. Some tests use continuous films, some require patterning, but all tests use some kind of driving force or stored energy to achieve the thin film delamination. The energy may come from the external mechanical force imposed on the film, or it can be stored in the film itself (through the internal film stress).

Most interfacial delamination tests empirically infer the adhesive strength by subjecting the specimen to some external load and measuring the critical value at which it fails [3]. While this is useful for routine quality control, these tests do not measure the interface fracture toughness, since the strain energy release rate usually can not be de-convoluted from the work of the external load.

Typical testing methods such as bimaterial cantilever, microscratch, peel, bulge, and edge lift-off are limited to organic films, cause complex stress fields, cannot achieve the large energy release rates (ERR) typical of metal thin film interfaces, and/or cannot handle sub-micro scale samples. For example, during the tests of scratch, peel, pull, blister and indentation, the interface is subjected to very high stress levels and consequent inhomogeneous deformations. Large amounts of inelastic deformation can result (especially in the peel test) and dominate the behavior during the test. The stress fields are difficult to analyze and the resulting delamination measurements tend to be qualitative and comparative.

While for some applications the qualitative comparison is good enough, quantitative interfacial fracture toughness values are desired for understanding factors contributing to thin film adhesion, for numerical simulations and for reliability studies.

Linear Elastic Fracture Mechanics (LEFM) is the discipline that provides quantitative answers to specific problems of crack propagation from stresses in different structures. LEFM can also be applied to de-convolute the energy release rate for thin film structures.

Among other challenges in studying the thin film delamination is the recreation of the interfaces. It is often not enough to know that an interface in a particular application is weak and prone to delamination because it can be difficult to accurately recreate or duplicate that interface with a bulk specimen and derive a meaningful adhesion value [4].

One more complexity for the thin film delamination is that the interfacial fracture toughness is a function of mode-mixity, which is a measure of the relative shear to tensile opening of the interface fracture surfaces near the tip. Typically, interfacial fracture toughness increases as mode mixity increases, such that the delamination is less likely to occur when the loading on the interface is shear-dominated.

Ability to handle nano scale thin films, ability to create representative interfacial conditions, ability to extract fracture parameters from the given test conditions, ability to address a wide range of mode mixities, etc. are some of the challenges associated with interfacial fracture toughness measurement tests. Therefore, appropriate test methods are needed to measure the interfacial fracture toughness for micro- and nano scale thin film interfaces.

1.2 Definition of the Interfacial Fracture Toughness

The energy required to separate an interface is often defined as the work of fracture, which is also called the interfacial fracture toughness, Γ_i . In most circumstances, this work of fracture is much larger than the true work of adhesion W_A, which is the amount of energy required to create new free surfaces from two bonded materials. The true work of adhesion is defined as:

$$W_A = \gamma_f + \gamma_s - \gamma_{fs} \tag{1.1}$$

Where γ_f and γ_s are the specific energies of the film and the substrate respectively, γ_{fs} is the energy of the interface. It is the energy required to separate the interface of interest or, more basically, to rupture atomic bonds at the interface. True work of adhesion is an intrinsic property of the film/substrate pair. It depends on the bonding type between the film and substrate, and the level of initial surface contamination, initial surface roughness, etc.

The true work of adhesion is often determined by contact angle measurements [5, 6]. If the tested particle is in thermal equilibrium on the substrate, then:

$$\gamma_{fs} = \gamma_s - \gamma_f \cos\theta \tag{1.2}$$

Where θ is the contact angle between the particle free surface and the substrate, as shown in Figure 1.2.

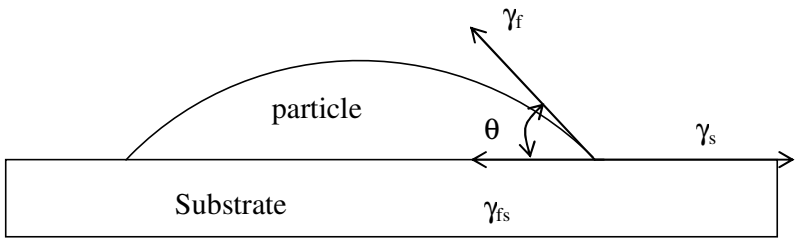

Figure 1.2 Contact angle measurements

Therefore the work of adhesion now can be expressed with the Young-Dupre equation [7]:

$$W_A = \gamma_f + \gamma_s - \gamma_{fs} = \gamma_f (1 + \cos\theta) \qquad (1.3)$$

Droplets in thermodynamic equilibrium can be obtained by the sessile drop method [8] or by annealing [5, 6] . When the surface energy of the film γ_f is known at a given temperature T_0, the surface energy at any given temperature T would be:

$$\gamma_f(T) \approx \gamma_f(T_0) + (T - T_0)\left.\frac{\partial \gamma_f}{\partial T}\right|_{T=T_0} \qquad (1.4)$$

Solving Equations 1.3 and 1.4 for the annealing temperature give the values of the true (thermodynamic) adhesive energy. Contact angle distribution can be obtained from the SEM or FRM image analysis [5, 6].

The true work of adhesion is a constant for given film/substrate pair. For metals on ceramic, the true work of adhesion is typically on the order of 0.5-2 J/m^2 [5, 6, 9, 10].

For an idealized case of Griffith fracture, the interfacial fracture toughness, Γ_i, is assumed to be equal to the thermodynamic work of adhesion, W_A:

$$\Gamma i = W_A \tag{1.5}$$

In practice, the work of adhesion leverages all other energy-absorbing processes [11, 12]. Even brittle fracture is accompanied by some energy dissipation either through plastic deformation at the crack tip, or crack face interactions such as asperity contact and ligament bridging. Therefore, small changes in interfacial bond strength can result in much larger changes in the interfacial fracture toughness. In a test method which the thin film is delaminated from the substrate, such energy dissipation makes it very difficult to extract the true adhesive energy from the total energy measured. The measured interfacial fracture toughness consists of the energy dissipated in plastic deformation, energy loss due to friction and the true work of adhesion:

$$\Gamma_i = W_A + U_{film} + U_{substrate} + U_{friction} \tag{1.6}$$

Where U_{film} and $U_{substrate}$ are the energy spent in plastic deformation of the film and the substrate. $U_{friction}$ is the energy loss due to friction. Generally, the plastic energy dissipation and the energy loss due to friction are functions of the true work of adhesion [13].

The measured interfacial fracture toughness is non-unique since it depends on the mode mixity (phase angel of loading), which is a relative measure of the amount of shear and normal stress components at the crack tip [4, 13-16]. ($\Psi=\tan^{-1}(\tau/\sigma) = \tan^{-1}(K_{II}/K_I)$).

Figure 1.3 is a schematic showing the relationship between Γ_i and Ψ . In Figure 1.3, the interfacial fracture toughness increases as the mode mixity is increased (from pure opening fracture to pure shear fracture).

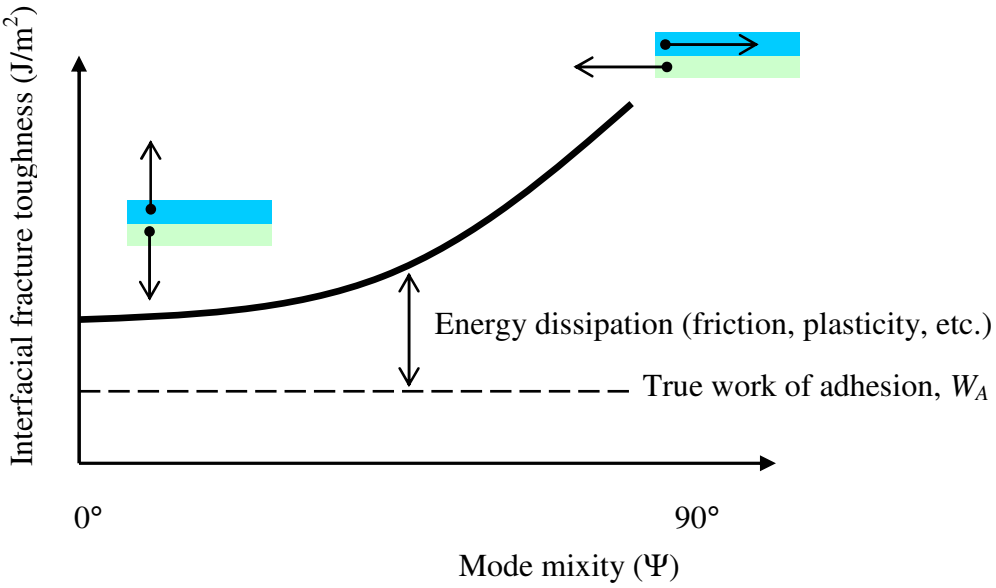

Figure 1.3 Interfacial fracture toughness as a function of the mode mixity

1.3 Overview of Interfacial Delamination Mechanics

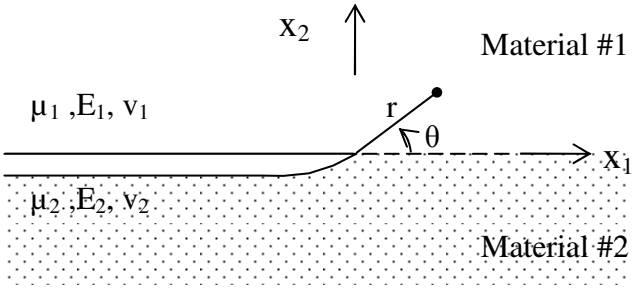

Figure 1.4 Geometry and conventions for an interface crack

Unlike cohesive fracture in bulk materials, interfacial fracture is complicated by factors such as oscillatory stress field [17], mode-mixity dependent interfacial fracture toughness [15], process dependent interfacial fracture toughness, etc. This section gives an overview of the interfacial delamination mechanics. Consider a crack tip region for an interface crack formed between two linearly elastic, homogenous, isotropic materials as shown in Figure 1.4, where μ, E, v are the shear modulus, Young's modulus and Poisson's ratio of the respective materials.

Dundurs [18] observed that the elastic dependence for the bi-material system could be expressed by using the following two non-dimensional parameters. With the conventions in Figure 1.4, the Dundurs' elastic mismatch parameters are:

$$\alpha = \frac{\mu_1(\kappa_2+1)-\mu_2(\kappa_1+1)}{\mu_1(\kappa_2+1)-\mu_2(\kappa_1+1)}, \quad \beta = \frac{\mu_1(\kappa_2-1)-\mu_2(\kappa_1-1)}{\mu_1(\kappa_2+1)-\mu_2(\kappa_1+1)} \tag{1.7}$$

Where $\kappa_i = 3 - 4v_i$ for plane strain and $\kappa_i = (3 - v_i) / (1 + v_i)$ for plane stress. The parameter α is a measure of the mismatch in the plane tensile modulus across the interface. It approaches +1 when material 1 is extremely stiff compared to material *2*, and approaches -1 when material 1 is extremely compliant. The parameter β is a measure of the mismatch in the in-plane bulk modulus. Both α and β vanish when there is no mismatch, and both change signs if the two materials are switched.

As a bi-material interface fractures, the mechanical property mismatch between the two materials results in shear stresses being induced by tensile stresses, and vice versa. Therefore, a bi-material interface under pure mode *I* loading, K_I, will yield both K_1

and K_2 locally at the crack tip [19]. For a two-dimensional system the complex stress intensity factor (SIF) is given by:

$$K = K_1 + iK_2 \tag{1.8}$$

Williams initially identified that an oscillating stress singularity behind the crack tip at a bimaterial interface exists [17]. Sih and Rice related the crack tip singularity, identified by Williams to a complex stress intensity factor [17, 20-22]. The stress field near the interfacial crack tip between dissimilar materials is a coupled oscillatory field scaled by K:

$$\sigma_{ij} = \frac{\mathrm{Re}(Kr^{i\varepsilon})}{(2\pi r)^{1/2}}\sigma_{ij}^{I}(\theta;\varepsilon) + \frac{\mathrm{Im}(Kr^{i\varepsilon})}{(2\pi r)^{1/2}}\sigma_{ij}^{II}(\theta;\varepsilon) \tag{1.9}$$

Where r and θ are the polar coordinates shown in Figure 1.4 and the dimensionless angular functions $\sigma_{ij}^{I}(\theta;\varepsilon)$ and $\sigma_{ij}^{II}(\theta;\varepsilon)$ correspond to traction across the interface at θ=0 of tensile and in-plane shear respectively. The parameter ε is defined as:

$$\varepsilon = \frac{1}{2\pi}\ln\left(\frac{\kappa_1/\mu_1 + 1/\mu_2}{\kappa_2/\mu_2 + 1/\mu_1}\right) \tag{1.10}$$

As $r^{i\varepsilon} = cos(\varepsilon lnr) + i*sin(\varepsilon lnr)$, Equation 1.9 represents an oscillatory stress singularity as the crack tip is approached ($r = 0$). If $\varepsilon = 0$, both K_1 and K_2 play similar roles as the classical, homogenous stress intensity factors K_I and K_{II}, which measure the normal and shear stress singularity respectively.

Since K is a complex number with a material dependent dimension, it is more convenient to evaluate the state of stress at a fixed length, L, from the crack tip [20]:

$$\left(K_1 + iK_2\right) \cdot L^{i\varepsilon} = \left|\left(K_1 + iK_2\right)\right| \cdot e^{i\psi} \tag{1.11}$$

With the mode mixity being defined as:

$$\psi = \tan^{-1}\left(\frac{\mathrm{Im}(KL^{i\varepsilon})}{\mathrm{Re}(KL^{i\varepsilon})}\right) \tag{1.12}$$

The choice for L is arbitrary, but should be selected as a fixed length and reported with the calculated values for the mode mixity.

Interface fracture toughness is defined as the critical value of the energy release rate (ERR), G_c, at which the bimaterial interface will begin to delaminate. As mentioned in the last section, it is not a single material parameter, but rather a function of the mode mixity, ψ, which measures the relative amount of "mode 2" to "mode 1" acting on the interface [15]. Malyshev and Salganik, Hutchinson, and Rice related the complex stress intensity factor to the energy release rate, crack tip normal and shear stress at some

length, and to the classical meanings of K_I and K_{II}, respectively [20, 23, 24]. The relation between the stress intensity factor and the energy release rate is [24]:

$$|K| = \sqrt{GE^*}\cosh(\pi\varepsilon) \tag{1.13}$$

Where G is energy release rate and E^* is effective Young's modulus. The E^* is given by:

$$E^* = \frac{2E_1^{'}E_2^{'}}{E_1^{'} + E_2^{'}} \tag{1.14}$$

With $E' = E/(1-\nu^2)$ for plane strain and $E' = E$ for plane stress.

G_c, the critical energy release rate, increases with mode mixity such that the delamination is less likely to occur when the interfaces is shearing-dominated.

Evans et al., He and Hutchinson, Thouless, and Akisanya and Fleck, based on the understanding of the oscillatory nature of the crack tip, have established guidelines to predict crack kinking out of a bimaterial interface [25-30]. Based on their work, crack kinking is reduced to a function of mode mix, stiffness of materials, and interfacial toughness of the interface materials. Once a crack has kinked, predicting its following path is done through applying a homogeneous crack growth criterion, that is, a crack attempts to grow with $K_{II}=0$.

1.4 Overview of Interfacial Delamination Testing

This section gives an overview of the most accessible methods used in the literatures with a focus on identifying the strengths and weakness of each method. These tests cover most of the tests that can give a quantitative or semi-quantitative measurement for the interfacial fracture toughness. The tests reviewed here include the superlayer test, the peel test, the pull test, the nano-indentation test, the blister test and the sandwiched specimen test. The superlayer test will be discussed first and in the most detail since this research is developed from this test.

1.4.1 Superlayer Test

Utilization of a stress-engineered superlayer to propagate an interface delamination was first described and implemented by Bagchi, Suo and Evans [31]. The essential features of the test include a thin film strip containing the interface of interest, a highly stressed superlayer, and a release layer, serving as a pre-crack or weakly adhering region that eases delamination initiation. The driving force for delamination is the residual stress in the highly stressed superlayer film in addition to the stress in the film of interest.

Figure 1.5 shows the superlayer test schematically. First a thin carbon release layer is thermally evaporated and patterned using the bilayer photolithography technique. This layer acts like a pre-crack for the test structure due to the weak bonding between carbon and the substrate. Its width is at least twice the Cu film thickness to avoid edge effects on the energy release rate.

In the second step the film of interest (Cu) and the superlayer (Cr) are deposited and patterned to form strips perpendicular to the carbon lines. In order to produce a range

of strain energy release rate, the thickness of the superlayer is varied. The metal bilayer structure is cut by wet etching or ion milling during the third step. If the strain energy release rate exceeds the adhesion energy, the strip decoheres or delaminates. If the films stay attached, the adhesion energy was not exceeded and a thicker superlayer should be used.

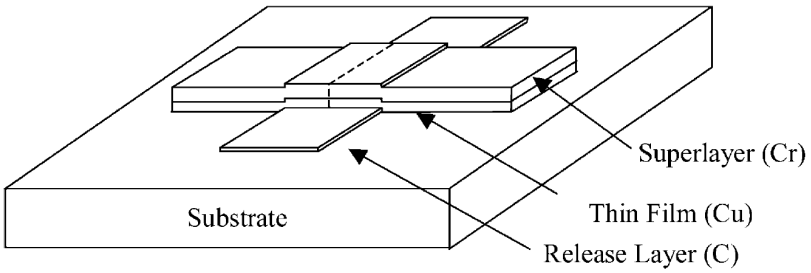

Figure 1.5 Schematic for superlayer test [31]

The interfacial fracture toughness is found when the superlayer thickness exceeds certain critical value, making the preparation of a number of samples necessary and limiting the efficiency of the test.

If the thin-film material does not delaminate from the substrate upon the application of the superlayer, their test will call for the processing of another substrate with the thin-film material and the deposition of a thicker superlayer to facilitate the delamination propagation. If the thin-film material layer does delaminate, their test will call for the processing of one more substrate and the deposition of a thinner superlayer to determine the lower bound for the interfacial fracture toughness. Such a trial-and-error repeated processing approach is tedious and could take several weeks to measure one interfacial fracture toughness data. Since there is no freedom to control the superlayer

thickness, the mode mixity for the superlayer test is limited, or the mode mixity relies on the test results. Because of this serious drawback of multiple processing of substrates and the less control over the mode mixity, their work [32] has not been actively pursued beyond 1996.

A similar idea of using the superlayer residual stress to drive thin film delamination was employed by Kinbara et al. [33] to debond Ti films with a Ni superlayer. In Kinbara's study, a normal stress was used for the adhesion measurement, and the mode mixity effects were not taken into account.

For superlayer with compressive stress, the thin film may buckle and relieve the stress. The strain energy with compressive stress is calculated by Hutchison and Suo [15]. Due to more complicated nature of this delamination such as the friction between the film and the substrate, compressive superlayer is not studied in this research.

Zhuk et al. [34] have measured the interfacial fracture toughness using the superlayer test and related it to the true work of adhesion from contact angle measurements. Xu et al. [35] used a 1*um* thick Cr superlayer with 1*GPa* residual stress to form cracks at the end of thin film strips.

As discussed, the superlayer test gives accurate adhesion energy values, but the implementation of this technique is very tedious and time consuming. One objective of this research is to find ways to overcome this limitation.

1.4.2 Peel Test

Peel test is the most common adhesion test to delaminate flexible coatings or thick films [36]. Figure 1.6 show the schematic of two peel tests for thin films on

substrate. The 90° peeling is the most prevalent and most thoroughly studied of all peel tests. Generally the peel test can be performed at any angel between 0 and 180°.

As discussed, the interfacial fracture toughness is a function of mode mixity. When performing a peel test, the interfacial region is subjected to both tensile and shear loads. The same interface tends to be much stronger in shear than in tension, which implied that the interface exhibit much higher in a predominantly mode II test as opposed to a mode I test.

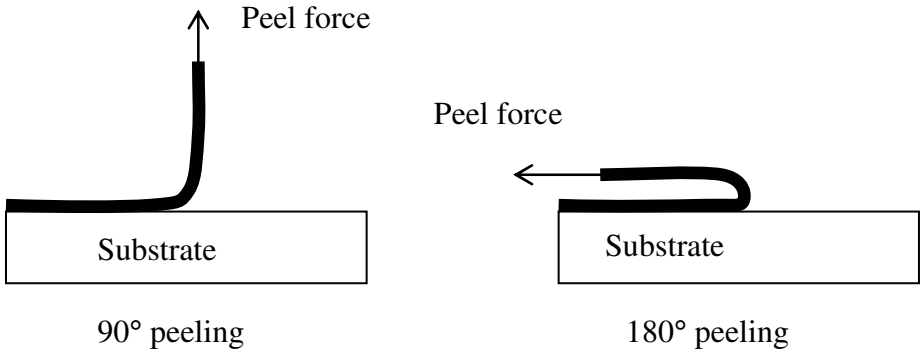

Figure 1.6 Schematic for the peel test

The advantage of the peel test is that the sample preparation is typically reasonably simple and straightforward. It gives a semi-quantitative measure of the coating adhesion strength to the substrate, which can be readily used for quality control purpose. Another advantage of the peel test is that the rate of delamination and the locus of failure can be controlled very precisely. Because of this, studied of the rate dependence of adhesion strength can be easily carried out using peel test. Also, the peel test can be readily implemented under conditions of controlled temperature and environment such as humidity conditions.

The main disadvantage of the peel test is that the films were subjected to very high strains during peeling. For metal films, this involves large inelastic deformation and the adhesion strength can be highly overestimated. Farris and Goldfard [37] studied the partitioning of the mechanical energy expended during a peeling test. In their work, they tested the adhesion of polyimide films to aluminum and demonstrated that the peel strength value is in the range of 500 to 900J/m^2. However, the same coating self-delaminated at an adhesion strength of 23J/m^2 when the coating thickness was increased to 120um. Further limitation of the peel test is that it is applicable only to tough flexible coatings or films. A thin film of a few microns is often fractured before any delamination. For nano scale thin films, it is almost impossible to grip the samples. Also, for thin film with strong adhesion, initiation a peel strip could make the sample preparation so straight forward, which is the main advantage of peel test.

1.4.3 Pull Test

Similar to the peel test, pull test is another test easy to perform. Figure 1.7 shows the schematic of a pull test. Sickfeld [38] gave an excellent review of the pull test and applied the pull test to paint coatings.

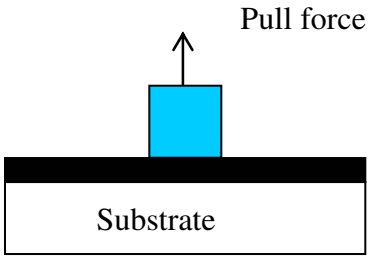

Figure 1.7 Schematic for the pull test

The pull test involves two additional materials besides the thin film and the substrate. A test stud, usually made of high modulus metal, is needed to apply the pull force. An adhesive is required to attach the test stud to the film under test. After the test stud is appropriately attached, it is pulled off under some controlled conditions using a tensile test apparatus.

Because of the nature of the loading, any off-axis loading component could impose a bending moment to sample and complicate the measuring results. Also since the film/substrate interface can not be perfectly uniform, the failure initiation would start with the region with defects or the regions with weaker adhesion. Further complexity is that the failure mode in most of the time is a combined mode of cohesive and adhesive failure. This all contribute to the wide variation of the test result, which is one of the main weaknesses of the pull test.

Pull test is very effective and efficient in qualitative and semi-quantitative evaluation of the interfacial fracture toughness, even though the mode mixity is limited to mode I tensile loading. However, the wide scatter in the test data makes it difficult to be a good tool to differentiate the factors contributing to the interfacial integrity.

1.4.4 Nano-indentation Test

Nanoindentation or indentation test is normally used for measuring thin film mechanical properties such as the modulus and hardness. It was also used to delaminate a weakly bonded brittle film from a substrate [39-47]. Figure 1.8 shows the schematic of the nano-indentation test. The indenter geometry could be in the shape of cone (plane stress) or wedge (plane strain). Marshall and Evans [42] provide the analysis for the conical indentation induced thin film delamination. De Boer and Gerberich [46, 47]

proposed a micro-wedge indentation test and analytical solution for the interfacial fracture toughness.

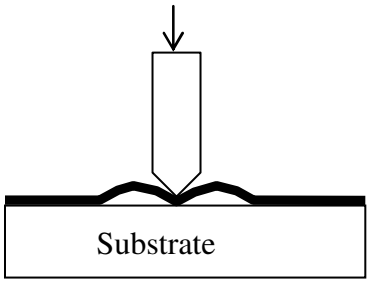

Figure 1.8 Schematic for the nano-indentation test

The advantage of the nano-indentation test is very obvious. It can be easily implemented for a wide variety of films, and literally no complicated sample preparation is involved other than the deposition of the films. The indentation test can be analyzed to provide quantitative results.

Unfortunately, nano-indentation test can not be used for ductile films on brittle substrates. A ductile film with strong adhesion most often yields first before delamination occurs. Even if the film delaminates from the substrate, the results are not reproducible [48]. For nano scale thin films, the delamination becomes unlikely due to the compressive load. Also, the excessive deformation in the substrate makes nano-indentation one of the most difficult methods to de-convolute the analytical solutions. A modified version of indentation calls for the addition of another layer which leads to often inconsistent and inclusive interfacial fracture data [48].

1.4.5 Blister Test

The peel test, the pull test and the nano-indentation test all involve a mechanically complex process with large in-elastic deformation in the film or the substrate. An immediate consequence is that the analysis of these systems in terms of continuum and fracture mechanics is very challenging, if not impossible. The blister test is an attempt to circumvent this difficulty by developing a blister in the thin film in a well-defined manner that can delaminate using moderate deformations and strains. Figure 1.9 shows some schematic of the blister test [36].

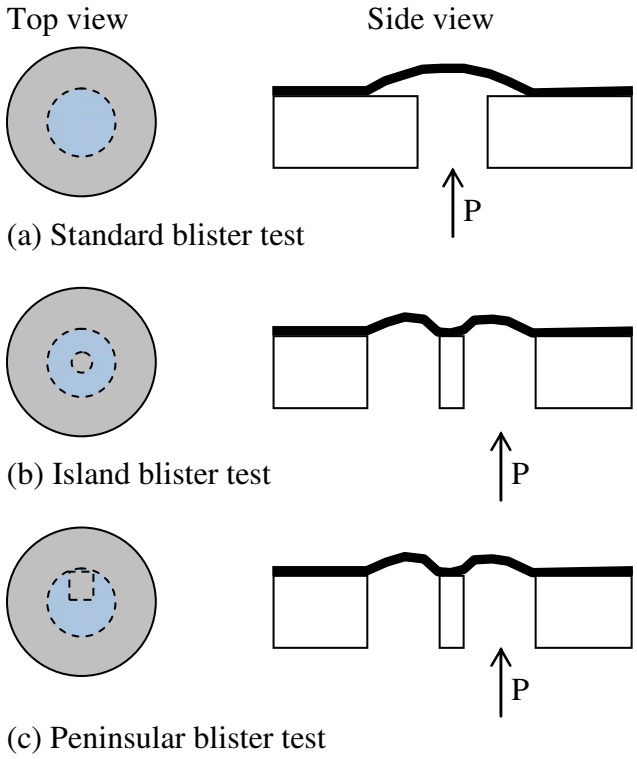

Figure 1.9 Schematic for the blister test

Dannenberg [49] was the first researcher to use this technique to measure the adhesion of polymer coatings. Lai and Dillard [50] gave an insightful account of the mechanics of this test. The main limitation of the blister test in Figure 1.9 (a) is that the film very often ruptures before any delamination occurs. Allen and Senturia [51, 52] circumvented this problem by using a modified island blister test shown in Figure 1.9(b). Due to a much smaller debond front by the inner island, the delamination occurs at a much lower applied pressure than would be required in the standard blister test. Further modification is done by Dillard and Bao [53] to overcome the instability problem in the island blister test.

One main advantage of the blister test is that a fully quantitative analysis exists based on fracture mechanics methods. This is due to the fact that relatively low strains were imposed to the films or the coating materials.

Compared to the peel test, pull test and indentation test, blister test requires a much complicated sample fabrication process. Drilling a hole at the center of the blister usually requires the use of an etchant. Besides, the blister test is limited to fairly flexible coating or films, such as polymer based paints and soft metals. Also, when the films bear very compressive residual stress, the film tends to buckle first before applying pressure. Apparently, for nano scale thin films, the sample preparation is very challenging.

1.4.6 Sandwiched Specimen Test

A number of sandwiched specimen test exist [13, 14, 54-57]. Figure 1.10 shows a few variations of such test. A general feature of these tests is that the interface of interest is sandwiched between two large elastic substrates. Of the various sample geometries

that can be made, three are briefly discussed here: the four-point bending test, the double-cantilever beam test and the brazil nut test.

The four-point bending geometry is first described by Charalambides et al. [54]. The stain energy release rate is a function of only the specimen geometry and the critical load for delamination growth. Since the delamination length does not enter into the calculation, it dose not have to be measured, greatly simplifying the test. While for the double-cantilever beam geometry [56], the energy release rate depends on both the load and the delamination length, making the data collection more problematic because the crack length is difficult to determine accurately when dealing with small samples. The mode mixities in these two tests are generally fixed. The third test, the brazil nut test, has the advantage of varying the mode mixities, which is done by rotating the sample relative to the axis of the applied load. The brazil nut test has been in use for quite some time to test homogeneous solid specimen and was first adapted to test interfacial fracture toughness by Wang and Suo [13]. This test has a strong advantage when one is interested in testing the interfacial fracture toughness as a function of the mode mixity.

The major advantage of the sandwiched specimen tests is that they lend themselves relatively easily to quantitative analysis using the fracture mechanics approach.

There are some disadvantages to the sandwiched specimen test. First, the sandwiched specimens are often made by a diffusion bonding process or with an epoxy. The diffusion bonding process often involves high temperatures for extended periods of times [57]. This introduces the possibility of altering the interface during the sample preparation step. In the case of an epoxy bond, the in-elastic deformation in the bond

layer in most cases can not be avoided and the interfacial fracture toughness measurement could be problematic. The sample preparation of the sandwiched specimens could be tedious and often requires polishing of the side face if the substrate is brittle. Lastly, the residual stress in the sandwiched thin film is not considered in these tests.

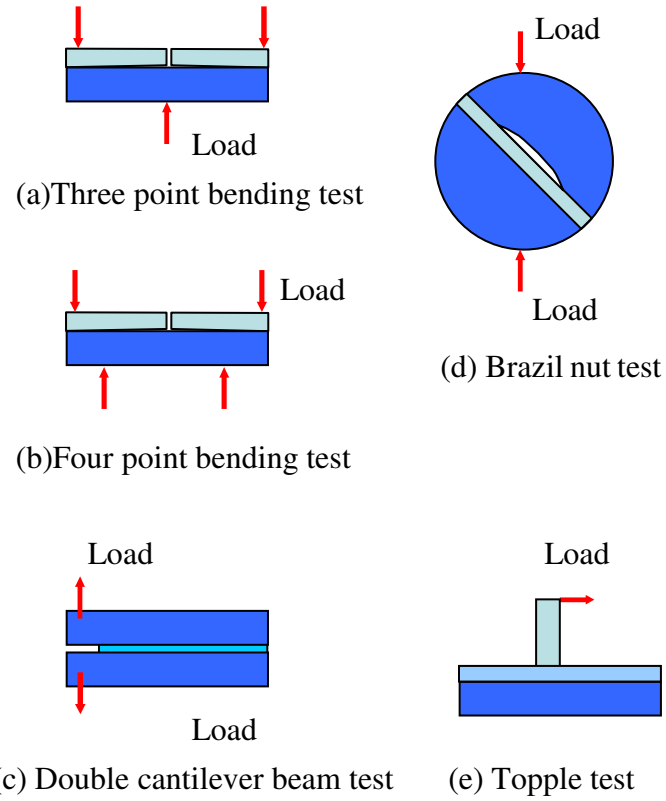

Figure 1.10 Schematic for the sandwiched specimen test

1.5 Criteria for a Good Adhesion Test

Each of the above tests provides useful and reliable data when applied in a conscientious manner. A good decohesion test should be able to provide sufficient energy to drive interfacial delamination, and should be able to relate the change in interfacial

fracture toughness with the change in mode mixity. Also, the test should meet the following criteria:

(a) Quantitative: The test method should preferably lead to a mechanics-based analytical solution to extract fracture parameters.

(b) Representative: The test sample should be prepared using the actual fabrication method to be able to create a representative interface.

(c) Relevant: The test method should simulate the actual usage stress conditions as closely as possible, both in sample preparation and in measurement. Final data must have relevance to the field use condition.

(d) Characteristic: The method should be able to cover a wide range of mode mixity.

(e) The test should be easy to perform, repeatable, and efficient.

When existing test methods are reviewed, it is seen that the existing test methods satisfy some of the above criteria, but not all of the above criteria.

For example, in peel, pull, blister and nano-indentation tests, the interface is subjected to very high stress levels and consequent inhomogeneous deformations. Large amounts of plastic deformation can result (especially in the peel test) and dominate the behavior during the test. The stress fields are difficult to analyze and the resulting measurements tend to be qualitative.

Test methods such as bimaterial cantilever, microscratch, peel, bulge, and edge lift-off are limited to flexible organic films, can only measure a single mode mix, cannot

achieve the large energy release rates (G) typical of metal thin film interfaces, and/or cannot handle micro-scale and nano scale samples.

Tests such as Unsymmetrical Double Cantilever Beam (UDCB), Single-Leg Bending (SLB), and Unsymmetrical End-Notched Flexure (UENF) require different fixtures and loading conditions to achieve different mode mixities and cannot handle micro-scale and nano scale samples.

Nanoindentation produces very high stress levels and consequent inhomogeneous deformations with a large amount of plastic deformation. Nanoindentation cannot achieve a wide range of mode mixity.

As seen, most of the existing tests require extensive fixtures to hold and apply loads, and therefore, cannot handle micro-scale thin films, and certainly not nano scale thin films.

In this research, the superlayer test is chosen based on the literature review. Another reason the superlayer test is chosen is based on the technical relevance between the superlayer test and the mico-contact springs. Figure 1.1 shows one example of the high-density pitch micro-contact springs developed for flip chip packaging and for circuit probing [1]. These micro-contact springs are thin film cantilevers with a stress gradient that biases them to an upward-bending position. These micro-springs are highly resistant to thermal fatigue and may permit the fabrication of a solder free solution for flip chip interconnects.

One challenge with the micro-contact springs is that the large stress concentration at the spring/substrate interface makes them susceptible to interfacial fracture. External forces during packaging and probing increase the likelihood of such failure.

As said, the method used in this research is developed from Bagchi's superlayer test which uses a stress-engineered superlayer to drive the interfacial delamination. Modi and Sitaraman [58] improved Bagchi et al.'s method using just one substrate with columns consisting of several thin film strips to determine the interfacial fracture toughness. By determining which of the strips delaminated and which of the strips did not delaminate, their method would provide a narrow range within which the interfacial fracture toughness would fall.

This research provides another approach to measure the interfacial fracture toughness using just one strip by introducing an etchable release layer design. Unlike the multiple strips used by Modi and Sitaraman, the proposed test method uses only one strip. Also, unlike the narrow range obtained by Modi and Sitaraman for the interfacial fracture toughness, the proposed test method can provide the exact magnitude of the interfacial fracture toughness by knowing where the delamination ceases to propagate.

1.6 Overview of Interfacial Fatigue Test

While measuring critical interfacial fracture toughness is an appropriate initial step in evaluating the integrity of an interface, the long-term interface reliability will actually be dependent on the subcritical delamination behavior. In measuring the subcritical delamination, one measures the actual interfacial crack growth as a function of time or loading cycle. The crack growth rate is measured as a function of the applied delamination driving force. Under cyclic loading, the interface delamination grows at levels of ΔG significantly lower than G_C.

Although many studies, both experimental and numerical modeling, have addressed delamination of thin film interfaces under quasi-static loading, interfacial

fatigue crack growth (FCG) remains largely unexplored. Only a limited amount of experimental data has been reported. Investigations on interface FCG are reported in [59-62] for metal-ceramic systems, in [63, 64] for polymer-glass, in [65, 66] for metal-metal, in [67-72] for polymer-metal, and in [70] for polymer-ceramic interfaces. In all of these studies, the initial crack size is in tens of millimeters and the specimen dimensions are typically more than tens of centimeters. Furthermore, fatigue crack growth rates (FCGR) are described by use of the Paris equation, which relates the applied strain energy release rate range, $\Delta G = \Delta G_{max} - \Delta G_{min}$, to the FCGR, da/dN, via a power law.

$$da/dN = C(\Delta G)^m \tag{1.9}$$

Where da/dN is the crack growth rate, ΔG is the range of energy release rate for the fatigue cycle and C and m are experimentally determined constants.

The most often used methods to perform the interfacial fatigue are four-point-bending tester [59, 61, 63, 64], double cantilever beam [59, 69, 71], and compact-tension [59]. Shang developed a flexural peel technique to study the crack growth behavior along a metal/ceramic interface [73]. This flexural peel test is fundamentally same to double cantilever beam in which the peeling force is applied to only one cantilever. Most of the reported tests do not consider the mode-mixity effect on the interfacial FCGR, which is found to be mode mixity dependent [74]. Also, all the listed tests do not account for the effect of the residual stresses in thin films, which is an inevitable factor during interfacial fatigue crack propagation. Finally, all these tests cannot capture the small crack effects of thin film interfacial fatigue.

Recent advances in nanoindentation and micro- and nano-tensile tests [75] have facilitated the measurement of mechanical properties of thin films such as young's modulus, hardness, fracture strength, etc. using monotonic loading. However, these tests have not been and cannot be used for the measurement of interfacial fracture properties of nano scale thin films, especially under cyclic loading. With nano-tensile tests, fixturing and holding of nano scale thin films without slippage is a problem. Also, the test cannot be used for compressive loading. Nanoindentation has been used by some researchers [48] to measure interfacial fracture properties of nano scale thin films. However, nanoindentation produces very high stress levels and consequent inhomogeneous deformations with a large amount of plastic deformation. When used on ductile metal films, nanoindentation often deforms rather than delaminates the thin film. Also, interfacial fracture data extraction based on nanoindentation is often cumbersome. Furthermore, nanoindentation introduces predominantly compressive stresses on the thin film. Also, it is necessary to isolate the effect of the substrate from the thin film properties when nanoindentation load is applied. The use of this test for a wide range of mode mixity and for cyclic loading is impossible.

Interfacial fatigue tests could also be performed by tests used for thin film material characterization (young's modulus, hardness, etc.). Table 1.1 lists some of such tests used for thin film fatigue testing. These methods could potentially be used for fatigue test of thin film interfaces. The disadvantage and advantage are listed in the table.

Table 1.1 Fatigue tests for thin film

Method	Description	Advantages	Disadvantages
Film on substrate	Subject the film/substrate composite to a thermal cycle and monitor the stress evolution in the film	easy sample preparation	• the thin film and the substrate is temperature dependent • low-cycle fatigue • Small strain range • Large thermal expansion coefficient difference between the film and substrate are needed • Need large film sample (several square millimeters), data are for averaging behavior
Microtensile testing	A dog-bone-shaped freestanding film specimen is mounted and aligned in the tensile tester	Straightforward	• Only tensile stress could be applied, compressive stress could not be applied • No interfacial crack study • Fixturing
Mircobeam (cantilever) by nanoindentation	A freestanding microbeam is deflected by indentation force	Easy to measure force and deflection	• Can only applied force in one direction(compressive stress • Lateral deflection of the beam could cause errors • Penetration of the beam material by the indenter tip • Difficult to study interfacial cracking
Nanoindentation	Apply cyclic motion of the nanoindenter to a film on substrate	Easy sample preparation	• Only compressive force • The film more often fractures rather than delaminates from the substrate • Complicated stress status
MEMS or piezo-actuator	Fabricate MEMS device or piezo-actuator to handle and apply force	Straightforward on-chip testing	• Complicated calibrations to obtain the absolute value of the forces and displacement • The maximum force is limited by the design of the actuator

CHAPTER 2

OBJECTIVES AND APPROACH

2.1 Objectives and Approach

The objective of this research is to understand the interfacial integrity of thin film structures by developing innovative fixtureless decohesion tests. By using the developed tests and numerical models, this research also aims to study various factors contributing to the interfacial integrity of the thin films.

The first decohesion test focuses on the interfacial fracture under monotonic loading. This test uses a superlayer to measure the interfacial fracture toughness of a thin film deposited on a substrate. The proposed method, single-strip decohesion test (SSDT), is a fixtureless test method, uses common IC fabrication techniques and overcomes the shortcomings of available methods. This test employs a stress-engineered super layer to drive the interfacial delamination between the thin-film and the substrate. An innovative aspect of the proposed test is to introduce a release layer of varying width between the thin-film and the substrate to control the amount of energy available for delamination propagation. The proposed test method will be applied to characterize Titanium (Ti)/ Silicon (Si) interface. Ti adhesive layers are commonly used in microelectronics and MEMS applications to help improve the adhesion of otherwise weakly adhering metal layers to a silicon substrate.

In addition to the monotonic decohesion test, a fixtureless interfacial fatigue test is developed. In this test, a micro-contact spring is fabricated with ferromagnetic

material deposited on top of the spring. An external electromagnet interacts with the spring to drive the interface crack initiation and crack propagation along the interface of the spring and the supporting base. Fatigue crack growth is monitored by E-beam lithography patterned metal traces that are few nm wide. The crack initiation and propagation can be monitored through electrical resistance measurement.

The research also aims to employ the results from both decohesion tests to study the interfacial integrity of thin-film spring structures that are used for microelectronic probing and packaging applications. Although this research is being specifically catered to thin films used in microelectronics probing and packaging applications, the approaches developed in this research are generic to many thin film applications, and thus can be generalized. Also, the final guidelines are extensible to the MEMS actuator and sensors fields for applications such as cantilever sensors and micro mirror stages.

2.2 Dissertation Outline

The outline for this dissertation is shown in Figure 2.1.

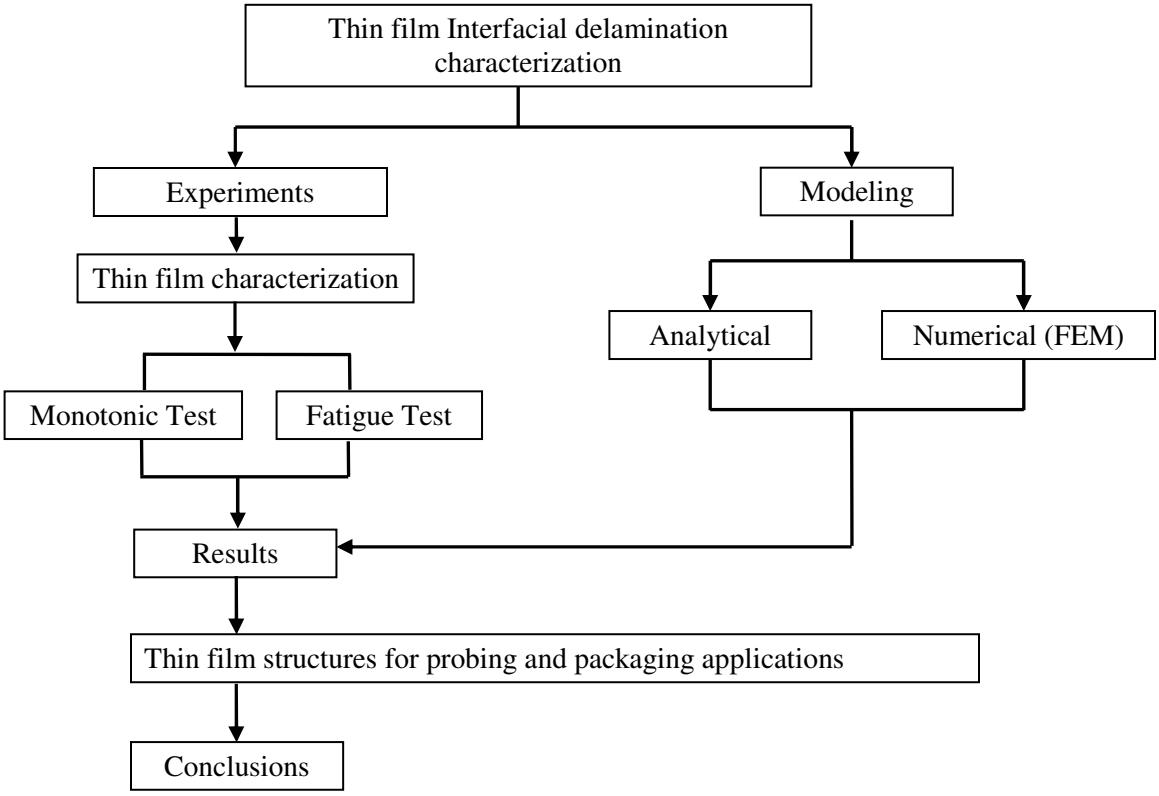

Figure 2.1 Dissertation outline

CHAPTER 3

INTERFACIAL DECOHESION TEST

3.1 Summary

This chapter discusses the details of the interfacial decohesion test under monotonic loading. The next chapter will discuss the thin film characterization and decohesion test results.

3.2 Stress-engineered superlayer in the fixtureless delamination test

Before discussing the fixtureless delamination test, it is essential to discuss the concept of the stress-engineered superlayer, and how the superlayer can be used to provide the energy for delamination propagation without using external fixtures and mechanical loads.

Intrinsic stresses can be intentionally introduced into thin film metals by changing the deposition condition, such as the argon pressure during the direct current (DC) magnetron sputtering [76]. Windischmann [77] used atomic peening model as well as grain boundary relaxation model to explain such stress engineering in thin film metals. When the argon pressure is low in the sputtering chamber, the target metal atoms collide less with the argon ions, and therefore, due to less scattering, the target metal atoms tend to deposit in a condensed pattern on the substrate. Due to this condensed deposition, the interatomic distance is less than the equilibrium spacing, and thus, compressive intrinsic stress is induced in the deposited metal layer. On the contrary, if the sputter chamber argon pressure is higher, the target metal atoms collide more with the argon ions, and

therefore, the metal atoms tend to deposit on the substrate in a coarser pattern. Due to the larger interatomic distance than the equilibrium spacing, tensile intrinsic stress is created in the deposited thin film metal. Figure 3.1 shows an example for Titanium-Tungsten (Ti-W) deposition where we were able to introduce stresses ranging from -1.25 GPa to +0.6 GPa in the Ti-W layers by changing the sputter chamber argon pressure from 2 to 20 mTorr (0.27 to 2.7 Pa). Similar results have already been demonstrated by others [76] for various other materials. Thus, by controlling the argon pressure in the sputter chamber, a uniform tensile stress or a stress gradient can be induced by depositing the metal layer-by-layer, starting with an intrinsic compressive stress and gradually changing it to an intrinsic tensile stress.

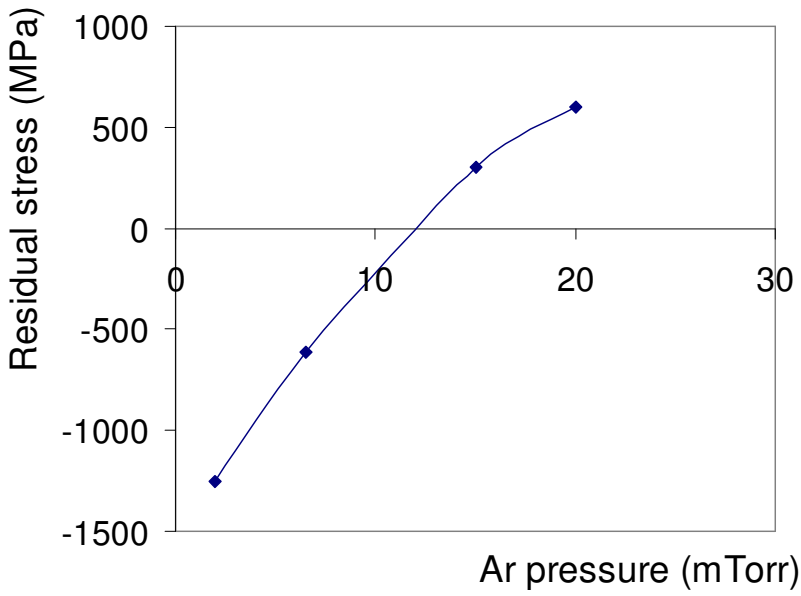

Figure 3.1 Residual stresses in Ti-W (10% Ti, 90% W) as a function of the Argon pressure during physical vapor deposition.

Such a stress-engineered layer is called a "superlayer", and the tendency for the superlayer is to peel off from the substrate due to the presence of a tensile stress or a compressive-to-tensile stress gradient. If the superlayer is to be deposited on top of a substrate with another thin-film material, the superlayer will try to peel off the underneath thin-film material layer from the substrate as shown in Figure 3.2.

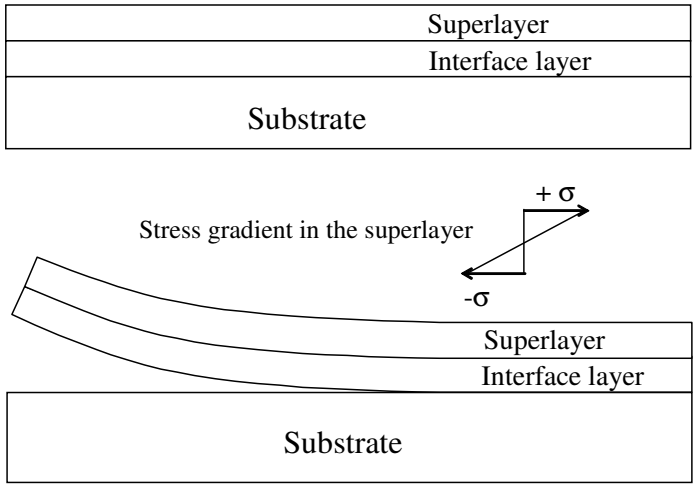

Figure 3.2 Delamination of the thin-film material under stressed superlayer

As mentioned earlier, the utilization of a stress-engineered superlayer to propagate an interface delamination was first described by Bagchi et al. [31]. For the successful implementation of the delamination test, the superlayer should supply enough energy, and at the same time, the deposition of the superlayer should not affect the interface of the thin-film material/substrate. This requires the superlayer to have the following characteristics:

(1) The superlayer must be deposited at ambient temperature;

(2) The superlayer must not react with the underneath thin-film material layer;

(3) The intrinsic stress in the superlayer should be able to provide sufficient energy to propagate delamination;

(4) The adhesion between the superlayer and the thin-film should be stronger than that of the adhesion between the thin-film and the substrate to ensure that no unwanted delamination occurs at the superlayer and the thin-film material interface

(5) The fracture toughness of the superlayer should be large enough to ensure that the superlayer does not crack before the delamination.

Cr or TiW superlayer, deposited by physical vapor deposition (PVD) sputtering, meets all of these criteria. Cr was also used by Bagchi's in his work on Cu/SiO_2 interfacial delamination study.

3.3 Single Strip Decohesion Test

As a stressed superlayer can be used to drive the delamination, the contact area of the interface will be changed to be able to modify the energy release rate. This is different to Bagchi's superlayer test in which the thickness of the superlayer is changed. This would mean that by using only one strip on one substrate, the interfacial fracture toughness can be measured, rather than processing several strips and several substrates. The change in the interface layer contact area will be accomplished through the introduction of a chemically etchable release layer between the substrate and the thin film of interest. The process steps associated with the proposed technique are summarized below and are illustrated in Figure 3.3.

- A release layer material is first deposited on a substrate. The release layer is patterned into a flat ribcage-like or coconut palm leaf-like structure where width of the ribs linearly decreases from the central sternum, as shown in Step

1. The patterning is done in a microelectronics cleanroom using photolithography and etching. The release layer is normally 5-10 nm thick.

- The interface material layer of interest is then deposited on the substrate and a stressed superlayer is deposited on top of the interface layer. Both the interface layer and the stressed superlayer are simultaneously patterned into horizontal strips with uniform width. The interface layer and the stressed superlayer are centered over the release layer strips, as shown in Step 2.

- A third photolithography and etching process is used to create a transverse bi-layer cut through the interface layer and the superlayer in the central region, as illustrated in Step 3. The etchant will selectively etch only the superlayer and the interface material layer.

- The entire sample is then dipped into another etchant, which will selectively etch away the release layer. When the release layer is etched, the interface material will start to delaminate from the substrate, due to the presence of the superlayer. The delamination will start at the central sternum region and is illustrated in Step 4.

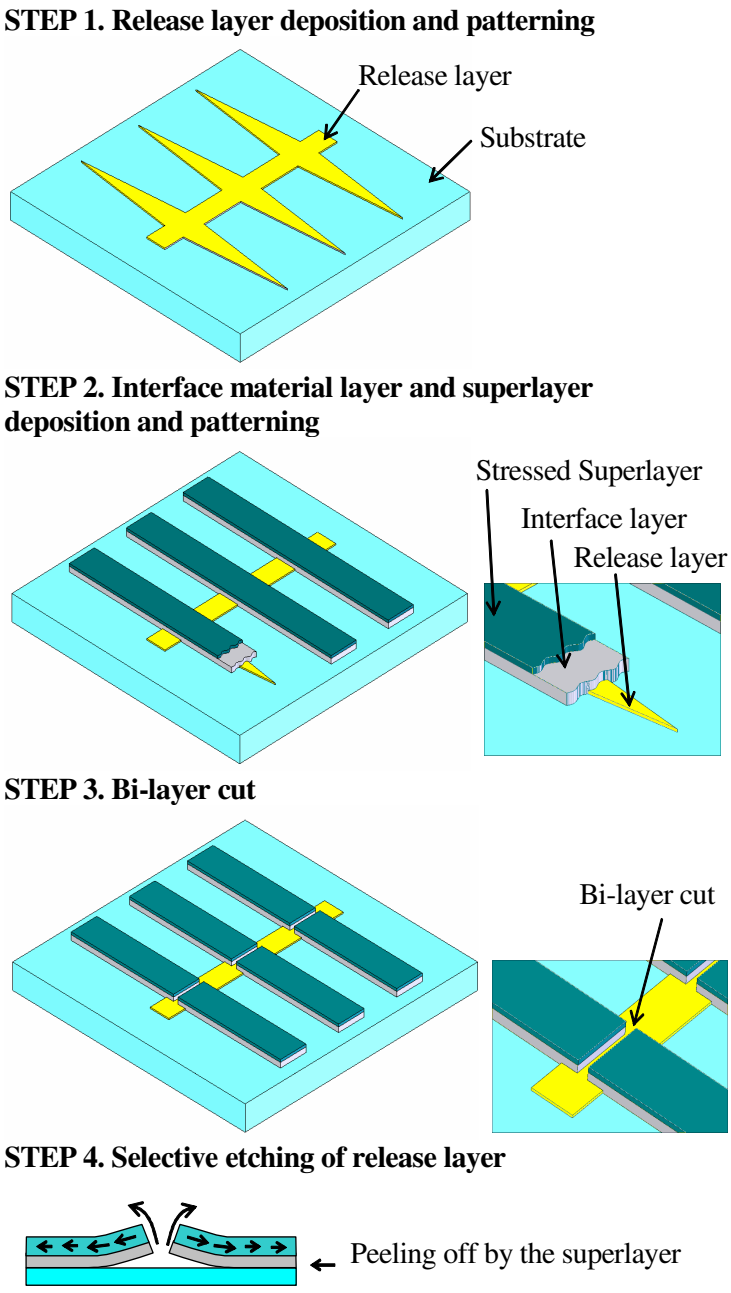

Figure 3.3 Procedure to perform the fixtureless superlayer delamination test using photolithography and etching technique. Step 1: Release layer deposition and patterning. Step 2: Interfacial material layer and superlayer deposition and patterning. Step 3: Bi-layer cut of the superlayer/interfacial layer. Step 4: Selective etching of the release layer.

Figure 3.4 shows the top view of the film strip in the test. As shown in Figure 3.4, the release layer of an isosceles triangle shape is sandwiched between the interface material layer and the substrate.

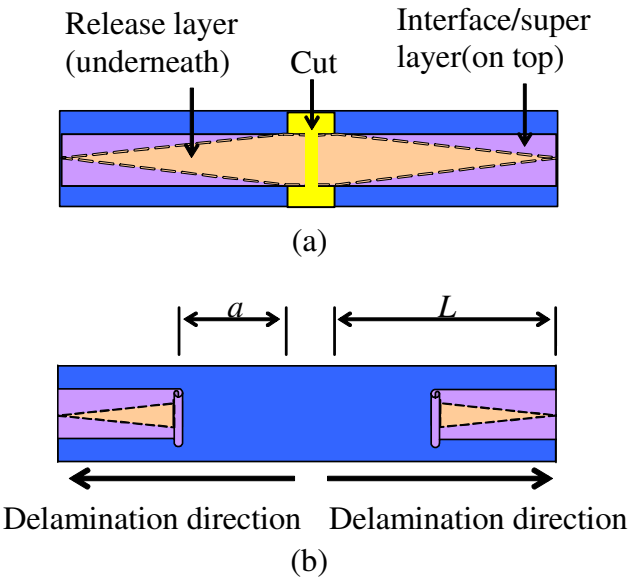

Figure 3.4 Schematic of the delaminated thin film strip. (a) The bi-layer cut before etching the release layer. (b) Delaminated strip after release layer etching. *L* is total length of the thin film strip, while *a* is the delamination length of the strips.

As one traverses along the strip axis from the delamination starting line (the transverse cut), the adhesion area between the interface material layer and the substrate increases, while the thickness and the stress magnitude in the superlayer, and thus the driving energy remains the same. With the increasing interface material area and the constant driving force, the available energy per unit area will decrease, as the delamination propagates along the strip axis. When the available energy per unit area can no longer overcome the interfacial delamination, the delamination will be arrested. The

energy release rate at a location where the delamination ceases to propagate will provide the interfacial fracture toughness.

In this method, only one thin film strip is needed. It is necessary to underscore that the superlayer stress magnitude and the thickness of the superlayer should be designed such that the delamination does not propagate all the way to the end of the strip.

3.4 Mask Set for the Single Strip Decohesion Test

Three photolithography masks are used in the test. Mask 1 is used to pattern the release layer. Mask 2 is used to pattern the interface layer and the superlayer simultaneously with uniform width. Mask 3 is used to create a transverse cut through the superlayer and the interface layer to create the crack initiation zone.

Figure 3.5 shows the mask set used to perform the decohesion test. The 5" mask allows the fabrication of 8 samples on a standard 4" wafer. Each sample independently provides enough information to measure the interfacial fracture toughness.

Within each sample there are 4 columns of strips. Each column has 27 rows of various release layer designs. Each column of strips is cut in the middle to create a pre-crack region as in Figure 3.4. Once it is cut, the test strip can delaminate to the left and to the right, creating two test strips. If all the test strips are identical and all the columns are summed, there are 1728 (27 x 2 x 4 x 8) independent sources or test strips (4 test site columns per sample and 8 samples per wafer), which allows for very good statistical confidence. It should be pointed out that a number of geometrical and dimensional variations in the release layer can be designed in Figure 3.5(a), and some of the variations will be discussed in detail in the following sections.

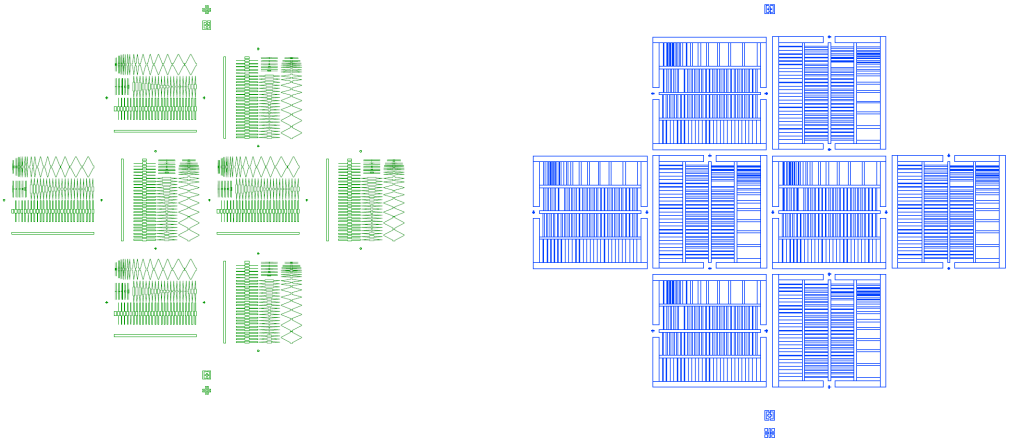

(a) Mask 1 for the release layer

(b) Mask 2 for the interface layer and the superlayer

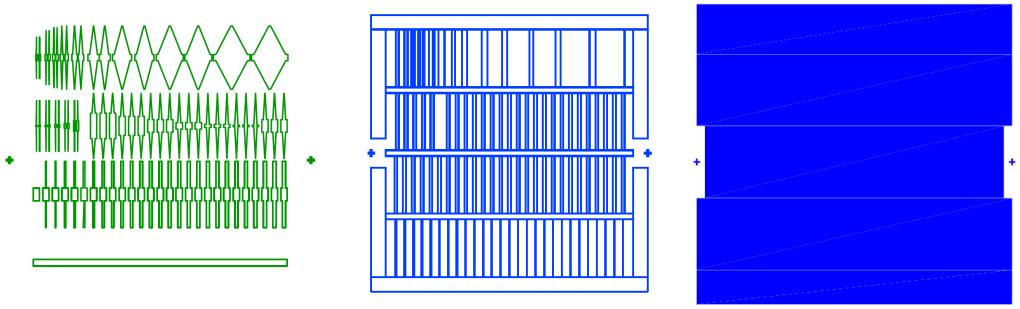

(c) Release layer

(d) Interface layer and super layer

(e) Crack initiation cutting layer

Figure 3.5 Mask set for single strip decohesion test. (a) Mask 1 used for patterning the release layer. (b) Mask 2 used for patterning the interface layer and the superlayer. (c, d, e) One sample site from each of the three masks is shown in greater details.

3.5 Variations in the Release Layer

The geometry of the release layer is critical to the delamination test because the geometry of the release layer will affect the delamination propagation. The release layer discussed thus far is in the shape of a triangle. But the shape of the release layer need not be limited to the shape which consists of triangles. Any shape that can vary the effective

adhesion area along the delamination direction could be used in the decohesion test. This section will discuss some variation in the release layer that was used in SSDT.

3.5.1 Triangle Release Layer

Triangle shape is one of the simplest shapes for the release layer. Figure 3.6 shows a few designs for the release layer using the triangle shape.

Design (1) in Figure 3.6 is used to study the effect of the triangle length (or height) to the interfacial delamination. The apex angle of the triangular area can be changed either by changing the height and/or the width of the triangle. Design (1) in Figure 3.6 illustrates examples where the apex angle is changed by changing the height or the length of the triangle. As the apex angle becomes smaller, the delamination needs to propagate through a longer distance to achieve the same reduction in release area. However, under ideal conditions, the location where the delamination ceases to propagate should have the same interface layer contact area regardless of the apex angle of the triangle. Although the apex angle should not influence the results, very small apex angle and thus longer length of delamination is not preferable for various reasons: 1) when the delamination length increases, the delaminated strip will curl upon itself absorbing more energy and also will touch the undelaminated flat area of the strip bringing additional frictional effects into consideration. 2) When the delamination length increases, extreme care needs to be taken to ensure that the entire strip does not have unintended voids or defects. Thus, in this work, the apex angle was kept between 5.46° and 16.26°

Design (2) is used to study the effect of the triangle width (or the strip width) on delamination propagation. In deriving the analytical solution of the energy release rate and mode mixity, the residual stress in the superlayer is assumed to be bi-axial. This is

generally true since the width of the thin film strip is usually much larger than the thickness of the strip. When the thin film strip gets narrower, bi-axial stress in the superlayer will be gradually changed to uniaxial stress. Design (2) will study how narrow the strip can be in order not to invalidate the biaxial assumption.

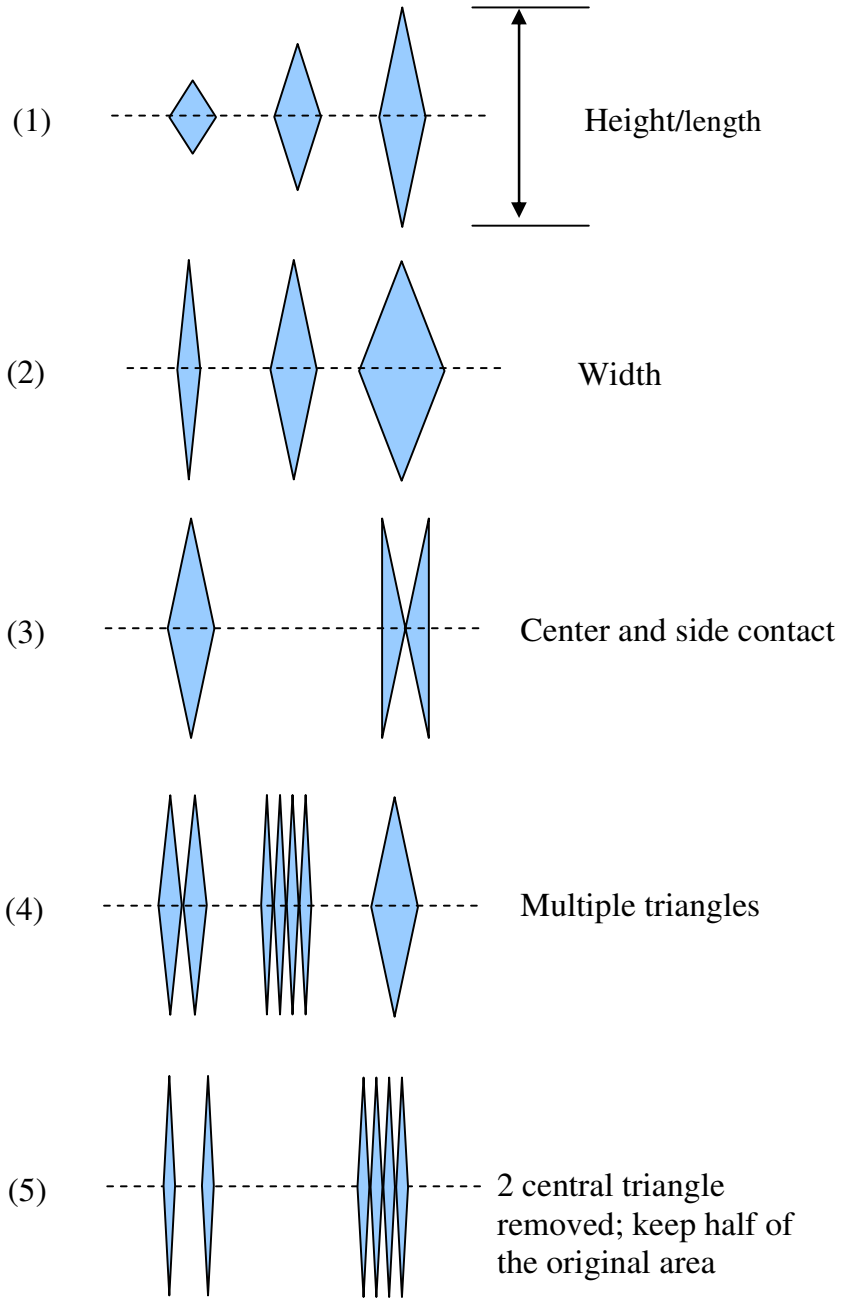

Figure 3.6 Different shapes in the release layer

Design (3) is used to study two different delamination due to the release layer difference. In Figure 3.6 (3), the two different shapes will initiate the delamination either from the strip center or from the strip side. In the cases discussed so far, the interface layer has two crack fronts on the two sides of the release layer and thus the release layer has four edges in total. However, when the release layer is shaped into two edge triangles, there is only one crack front in the interface layer. Although this sounds beneficial, this design has an inherent weakness, as this design may facilitate the delamination from the edge of the strip toward the center, rather than along the strip length. In other words, this design may facilitate delamination along both the length and the width directions of the strip and thus will make the computation of fracture parameters difficult. Design (3) will test this expectation.

Design (4) is used to study the effect of the multiple triangles. The intention to use multiple triangle release layer is to distribute the energy release more uniformly during delamination. In Figure 3.6(4), the effective adhesion area for different release layer is kept the same. In other words, the difference between one triangle and two triangle release layer is to break one triangle into two smaller triangles while the height of the triangle is kept the same. It is expected the delaminated length will be roughly the same with the same super layer if the strip width is very narrow. While for wider strips, some difference might be expected.

Design (5) is used to study the effect of the adhesion area. Due to the adhesion area difference, the delamination length is expected to vary accordingly. Pattern (5) is designed in the way that one delamination is expected to be twice longer than another delamination.

Figure 3.7 shows how these designs consisting of triangle release layer are incorporated in the Mask (1).

Figure 3.8 shows the optical image of the patterned release layer with design (1), design (2) and design (3). These release layers are 10nm thick gold layer patterned with mask (1). Figure 3.9 shows the optical image of the patterned release layer with design (4).

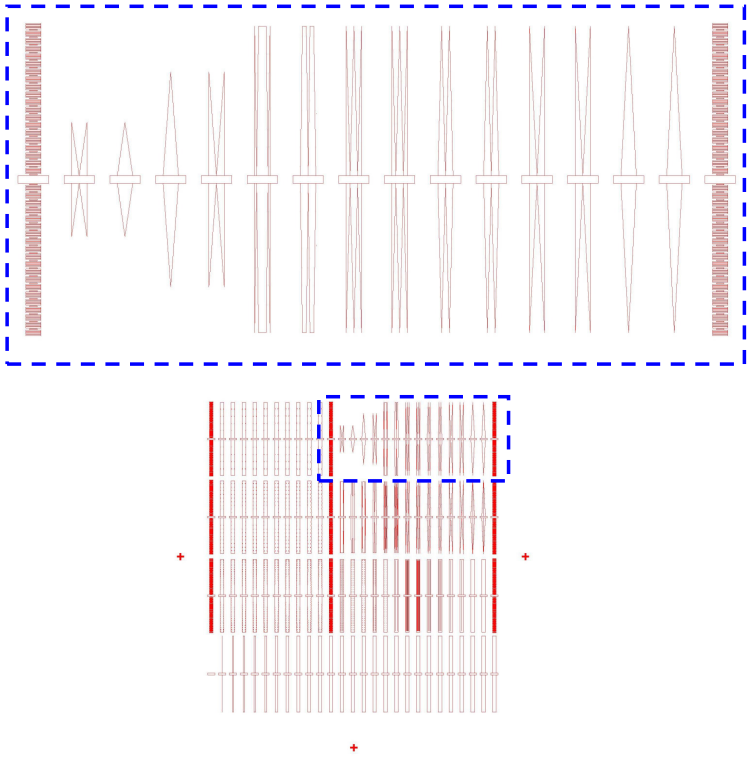

Figure 3.7 Triangle release layer in the mask set

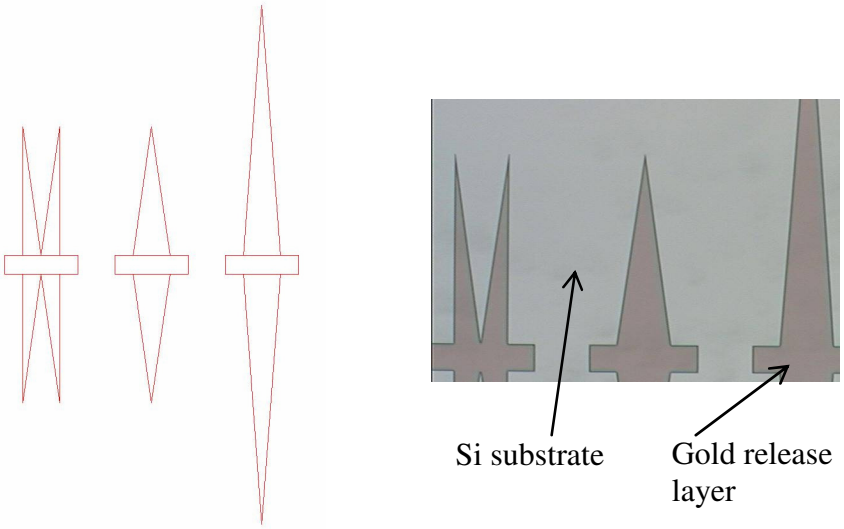

(a) Pattern used in the Mask (b) Optical image of the release layer (gold on silicon wafer)

Figure 3.8 Patterned release layer for design (1), (2) and (3)

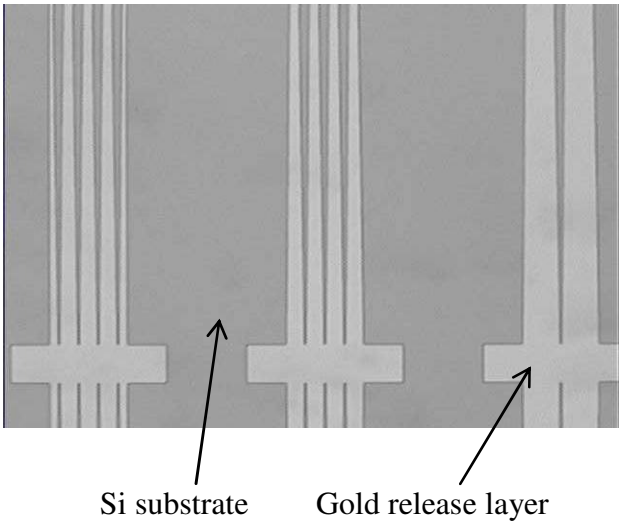

Figure 3.9 Optical image of the patterned release layer with design (4)

3.5.2 Release Layer Consisting of Other Shapes

Some other kind of shapes such as discrete circles, discrete rectangles and stepped triangle can also be used as long as these shapes can continuously or discretely vary the effective adhesion area along the delamination direction. Other shapes, like parabolic curve, could also be considered. Due to the technical difficulty to make these shapes with the conventional photolithography, these shapes were not pursued in this research.

Figure 3.10 demonstrates some of the other shapes used for the release layer. In all these three cases, the effective adhesion area between the interested layer (interface layer) and the substrate increases along the delamination direction increases. Figure 3.11 shows some optical image of the patterned release layer based on the design of Figure 3.10.

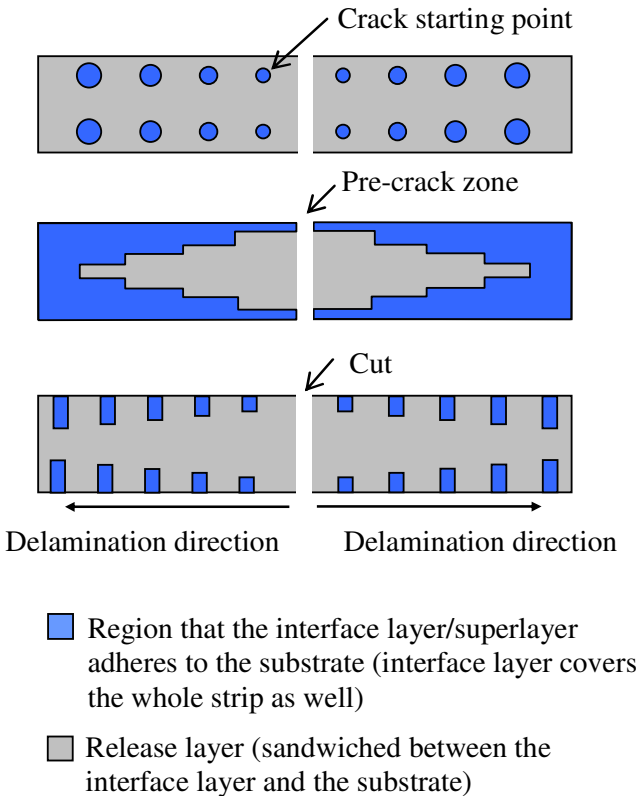

Figure 3.10 Some other shapes of the release layers

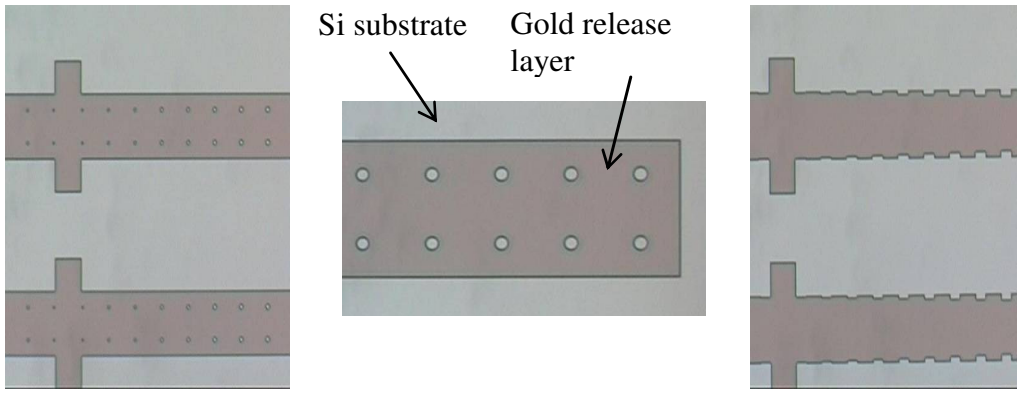

(a) Release layer containing discrete circles

(b) Magnified release layer for case (a)

(c) Release layer containing discrete rectangles

Figure 3.11 Optical image of the patterned release layer with discrete shapes

Further variations in the release layer include the number of rows of such shapes in the release layer, the distance change between discrete shapes, and whether the discrete shapes are connected or not. Figure 3.12 shows some optical image of the patterned release layer in which the discrete circles are connected. The intention to connect the discrete circles is to smooth the energy release rate to avoid any driving force jump during the delamination propagation.

Figure 3.13 shows some optical images of the patterned release layer in which multiple rows of connected circles are included.

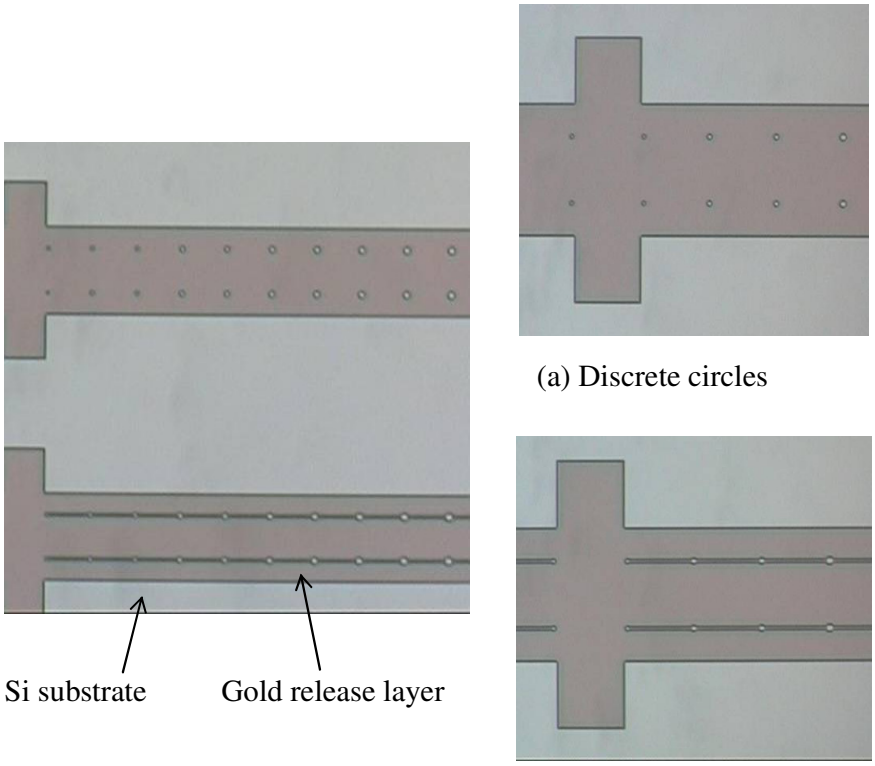

(a) Discrete circles

(b) Connected circles

Figure 3.12 Connected discrete circles in the release layer

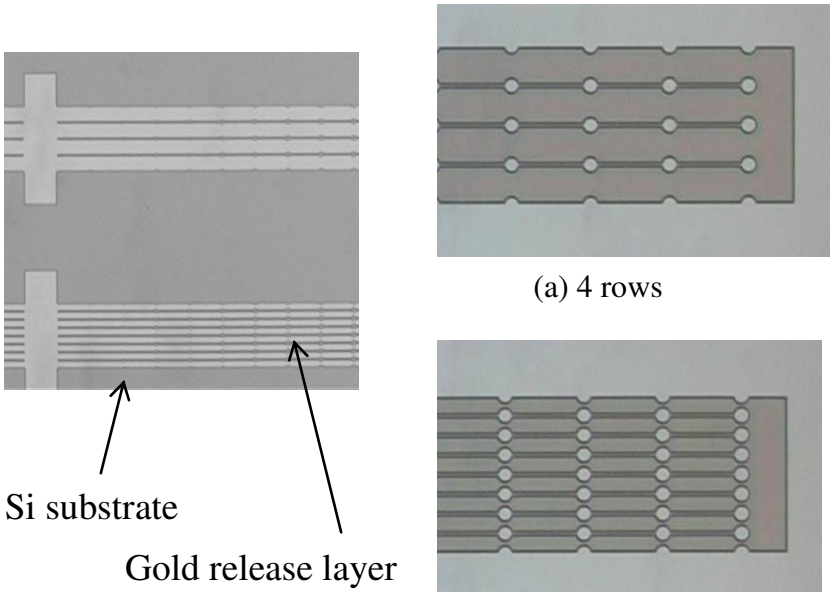

(a) 4 rows

(b) 8 rows

Figure 3.13 Multiple rows in the release layer

Due to the high fidelity features created by the photolithography, it is possible to investigate a number of possibilities. Other variations considered in this work include the shape change in the discrete patterns, for example, square and diamond shapes; the distance variation between the discrete patterns; the size of the discrete shapes, etc.

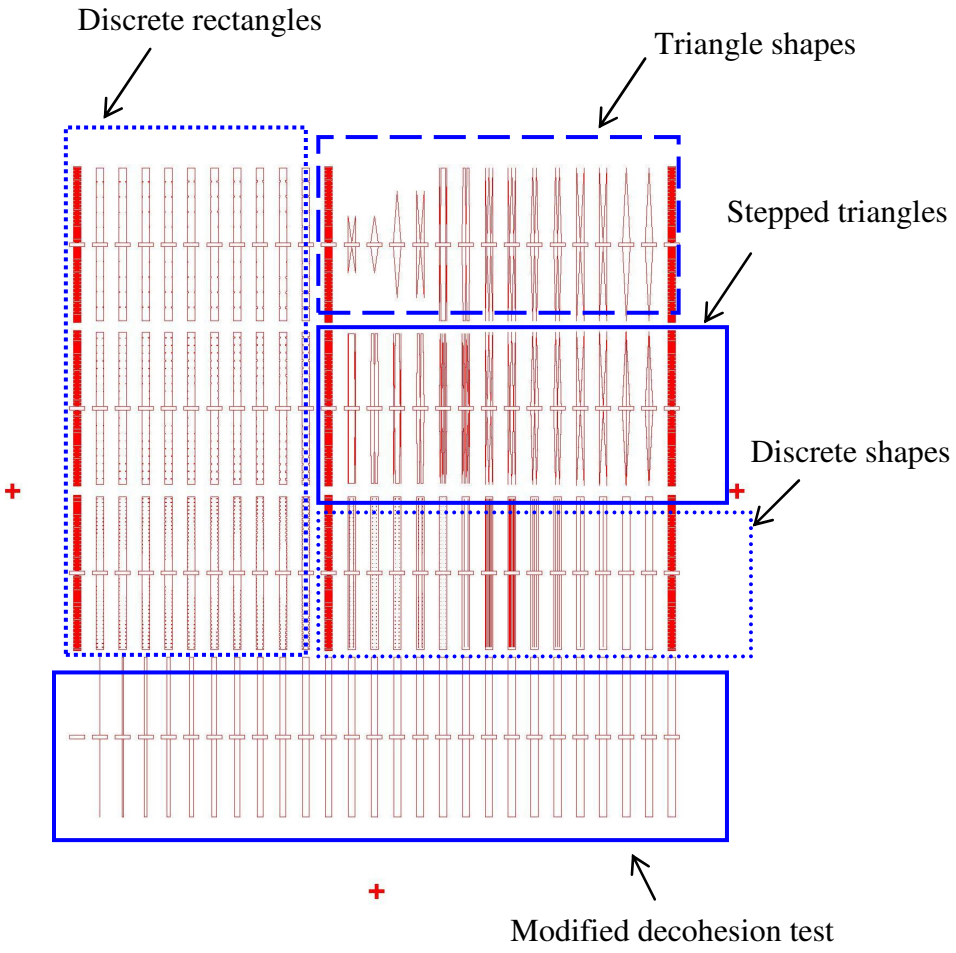

Figure 3.14 Mask layouts in one sample site to incorporate all proposed design variation in the release layers

CHAPTER 4

EXPERIMENTAL RESULTS FOR INTERFACIAL DELAMINATION TEST

4.1 Summary

This chapter presents the experimental results for the interfacial delamination test with a focus on the test using a triangle release layer. This chapter starts with the residual stress measurement in the superlayer. Then it shows the test results for Ti/Si interface. The outline for the test procedure is shown in Figure 4.1

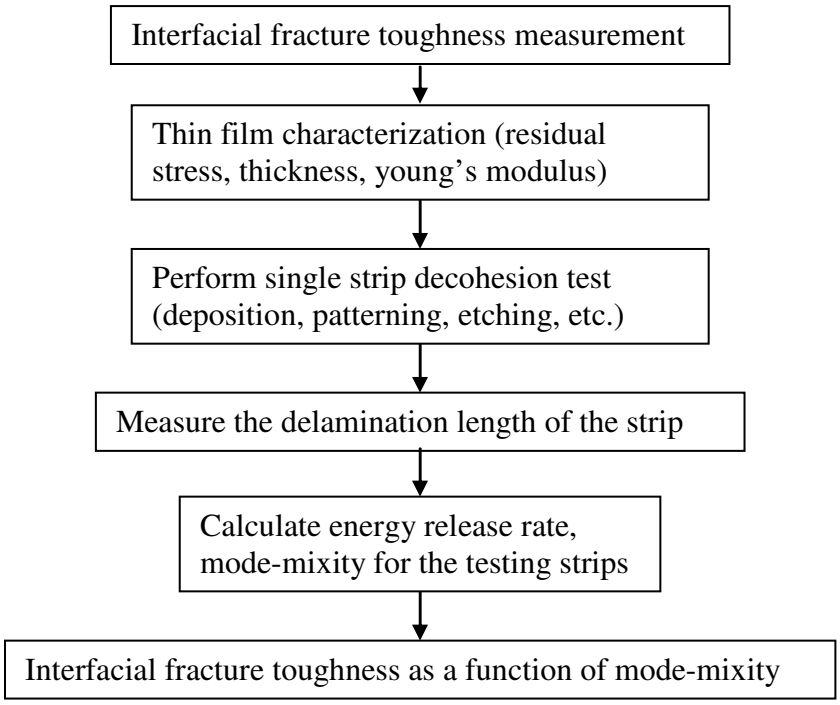

Figure 4.1 Outline of the interfacial fracture toughness measurement

4.2 Residual Stress Characterization for Test Film

4.2.1 Compressive and Tensile Residual Stress

Accurate measurement of residual stress in the superlayer as well as in the interface layer is critical to calculate the energy release rate for the decohesion test. This section describes the measurement of the residual stress in films used in the decohesion test.

Stress in thin films comes from differences in thermal expansion (thermal stress) or from the microstructure of the deposited film (intrinsic stress). Thermal stress occurs because film depositions are usually made above room temperature. Upon cooling from the deposition temperature to room temperature, the difference in the thermal expansion coefficients between the substrate (wafer) and the film causes thermal stress. The terms “substrate” and “wafer” will be used interchangeably in this work. Intrinsic stress results from the microstructure created in the film as atoms are deposited on the substrate. Either compressive or tensile stress can be generated depending on the deposition pressure. The deformation of the thin film can create bending and compressing, or expansion of the substrate surface. The result is a slight concave or convex curvature of the wafer as shown in Figure 4.2.

(a) (b)

Figure 4.2 (a) Compressive stress. The film wants to be "larger" than the substrate since it was "compressed" to fit. (b) Tensile stress in the film. The film wants to be "smaller" than the substrate since it was "stretched" to fit.

4.2.2 Stoney Equation for Stress Measurement

In the Single Strip Decohesion Test, the residual stress in the superlayer is the sum of the thermal stress and the intrinsic stress. The stress is measured indirectly by measuring the curvature of the wafer. By measuring the wafer curvature before and after deposition of the film, the stress can be calculated using Stoney's equation [78]. This is accomplished by creating a reference scan before deposition, and comparing it with the post deposition scan of the same wafer at the same temperature, in the same position, using the same scan recipe.

The stress in the thin film is calculated using Stoney's equation [78]:

$$\sigma = \frac{1}{6R}\frac{E}{1-\nu}\frac{t_s^2}{t_f} \tag{5.1}$$

σ: stress

t_s, t_f: substrate and film thickness;

R: radius of curvature;

E: young's modulus for the substrate;

v: poisson's ratio of the substrate;

4.2.3 Precision Wafer Locator for Stress Characterization

The location and orientation of the wafer is precisely controlled by a precision locator in the KLA-Tencor® profilometer. This precision locator, as shown in Figure 4.3, guarantees the pre-deposition scan and post-deposition scan start from the same position on the wafer. Therefore, the curvature change can be calculated based on the

difference in two scans. Also, this locator can be rotated precisely by 90°. The residual stresses in two directions perpendicular to each other can be measured.

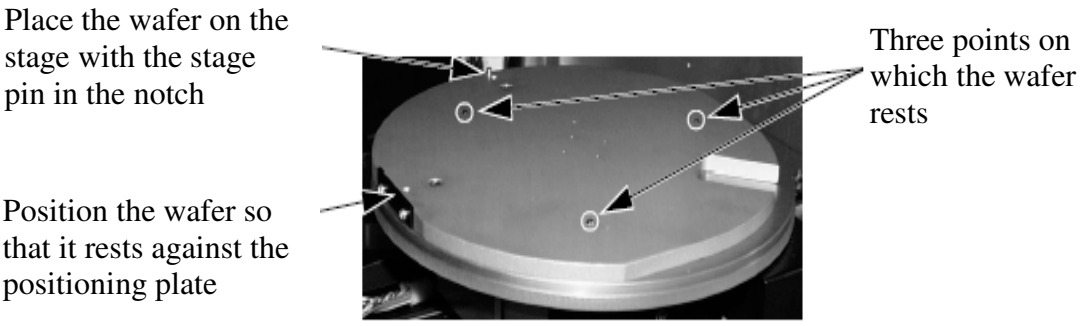

Figure 4.3 Precision wafer locator on the stage during residual stress measurement

Figure 4.4 shows an example the original scanning and post-stress scanning for TiW thin film. The scan length is about 80mm. The difference between these two scans is the net effect due to the compressive stress in the film. The program calculates the stress in the film based on the input such as film thickness, young's modulus of the wafer. Also shown in Figure 4.4, the average residual stress in the film is -1.414GPa. The radius of curvature is 29.2 meters.

4.2.4 Residual Stress in Cr Film

Cr is the super layer film used in this test. Accurate characterization of Cr is critical. The stress is measured for Cr film with different thicknesses. The purpose of doing this is to check the thickness dependency of the residual stress in Cr film. Table 4.1 gives the residual stress measurement of Cr thin films for different thickness used in the test. In Table 4.1, the stress is measured along two directions, in which one is

perpendicular to another. The purpose of doing this is to decrease the effect of the "primary or secondary flat" in the wafers.

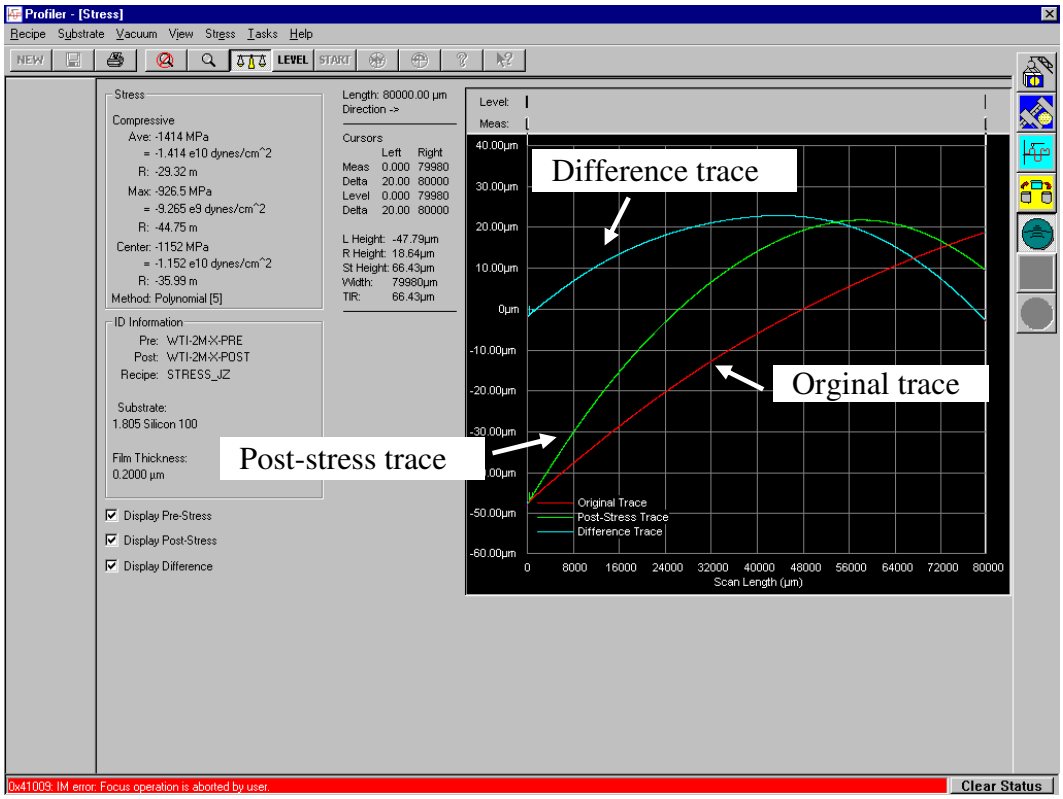

Figure 4.4 An example of the original scanning and post-deposition scan. The curve difference is used to calculate the curvature of due to wafer.

All Cr films are deposited at 3mTorr. The results show that at this pressure, the residual stress in Cr film is roughly 1GPa and is independent to film thickness. Other residual stress measurement on Nickel/TiW/Ti film also verifies this independency.

From the Table 4.1 it can be concluded that the stress from the x-direction scan is always larger than that in the y-direction because the primary flat is perpendicular to the x-direction, which makes the x-direction easier to be deformed. For this reason, same

stress yields a larger curvature in x-direction, therefore, larger residual stress based on the Stoney equation.

Table 4.1. Residual stress measurement by KLA profilometer

Nominal thickness (Å)	X direction (MPa)	Radius of curvature X direction(m)	Y direction (MPa)	Radius of curvature Y direction(m)	Mean (Mpa)
4000	1022	25.05	958	26.72	990
2500	1009	40.91	954.1	43.27	982
2000	1010	51.1	968.5	53.20	989
1500	1149	59.85	1088	63.25	1119
500	1028	200.9	980	210.6	1004

4.2.5 Cr Film Residual Stress as a Function of Deposition Pressure

Figure 4.5 shows the Cr film residual stress as a function of the deposition pressure. At low pressure, the residual stress in Cr film is about 1.2 to 1.5GPa.

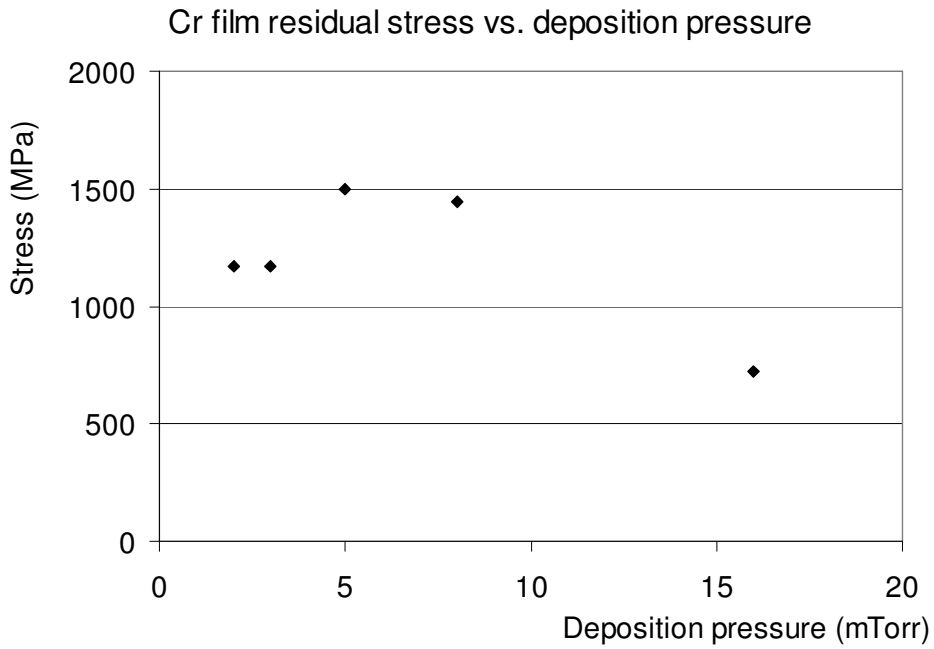

Figure 4.5 Residual stresses in Cr film as a function of deposition pressure

4.3 Procedure of the Decohesion Test

Careful substrate cleaning is essential for the test. Before the test, bare test wafers are solvent cleaned in trichloroethylene, acetone, and isopropyl alcohol in order to remove organic contaminants. Then they are rinsed in de-ionized (DI) water and submerged in BOE (buffered hydrofluoric acid) for 2 minutes to remove inorganic contaminants. Finally the wafers are de-ionized, dried off by the nitrogen gun, and dehydrated for 10 minutes in an 110˚C oven.

A very thin gold layer (10nm) was used as the release layer. Au, Ti and Cr were all deposited using a Unifilm™ DC sputter (PVD-300 from Unifilm™ Technology). This deposition chamber achieves 99% film thickness uniformity (from center to edge) and very little biaxial planar stress anisotropy.

Figure 4.6 shows the flow chart of the single decohesion test for Ti/Si interfaces. In this test, the superlayer layer is Cr, the interface layer is the Ti, and the release layer is Au. The detailed recipe for performing this decohesion test is attached in Appendix 4-2.

4.4 Ti/Si Interfacial Decohesion Results

4.4.1 Ti/Si Interfacial Delamination

Based on the design discussed thus far, Cr superlayer with different thicknesses was used for the Ti/Si delamination test. Figure 4.7 shows some SEM images of the delaminated strips, which are 2100μm long and 200μm wide.

Figure 4.7 (a) shows the optical image after the bi-layer cut in which the delamination has not been initiated. Figure 4.7 (b) and (c) show the delaminated thin film strip. As seen, the delamination propagates up to some distance and ceases to propagate

when the available energy for delamination propagation is balanced by the interfacial fracture resistance. From the location where the delamination ceases to propagate, the interfacial fracture toughness can be obtained.

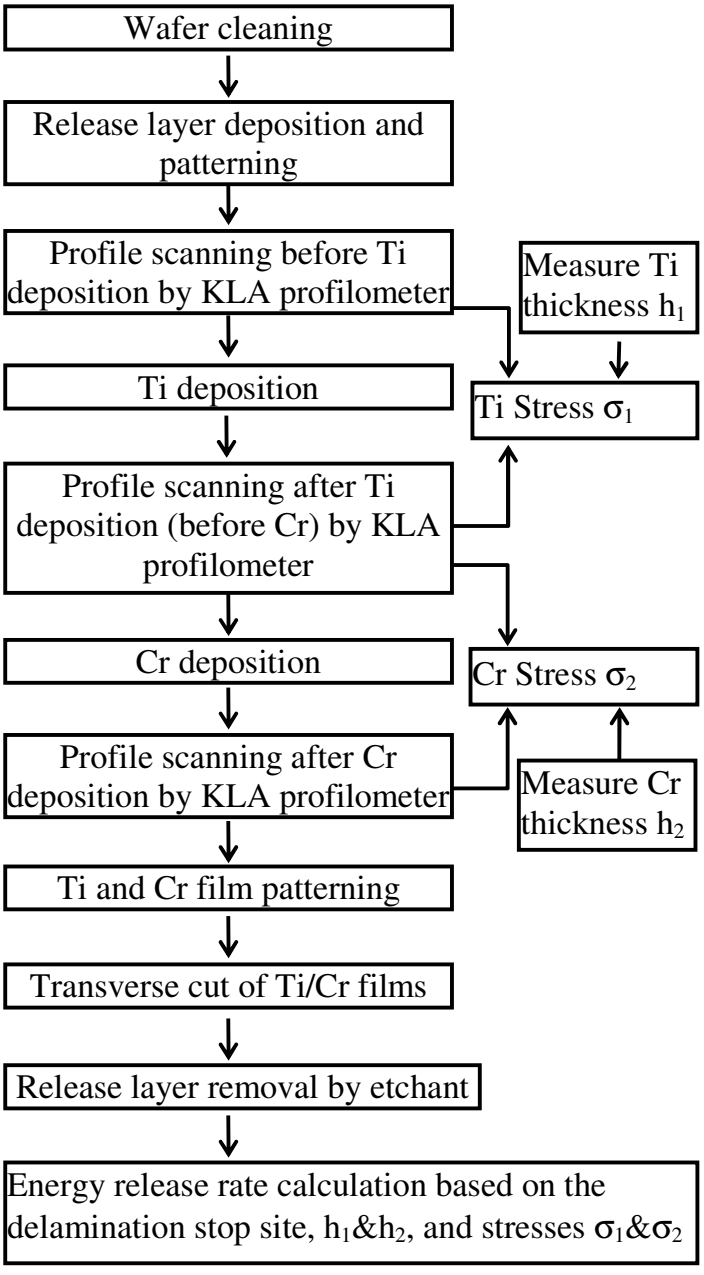

Figure 4.6 Flowchart of the single strip decohesion test

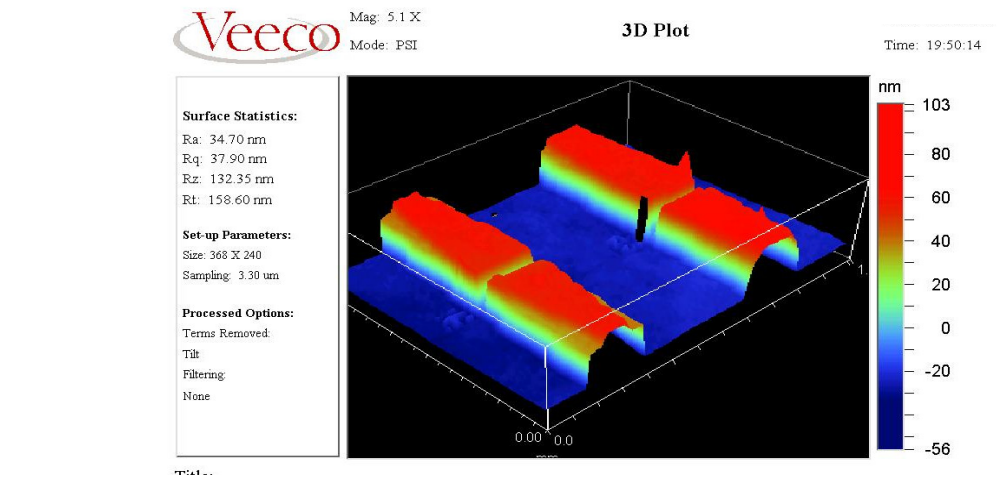

(a)

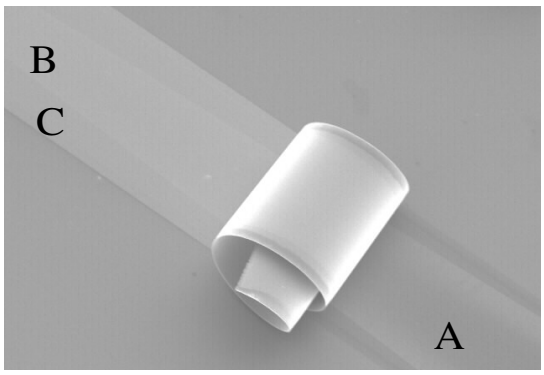

(b)

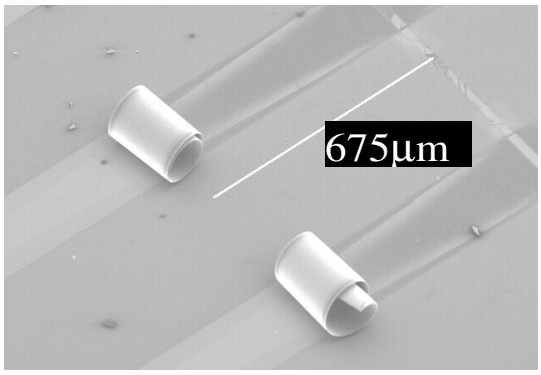

(c)

Figure 4.7 (a) Optical image after the bi-layer cut and before the delamination test. (b)SEM images of delaminated strips. Region A in (a) is the delaminated region. Region B and C are the undelaminated regions. (c) The total delamination length of the film strips in (c) is about 675µm. Particles in the image is the silicon particles from the dicing of the substrate.

Table 4.2 shows the interfacial fracture toughness for Ti/Si interface. It shows that the film strip tends to delaminate a longer distance with thicker Cr superlayer. This is to be expected, as the available energy for delamination propagation is greater for a thicker

Cr superlayer, and therefore, the balance between interfacial fracture toughness and the energy release rate occurs at a longer delamination length a. The mode mixity was shown in the table. The detailed procedure to calculate energy release rate and mode mixity will be shown in the next chapter. Table 4.2 shows that the interfacial fracture toughness increases with the mode mixity.

Table 4.2 Energy release rate (ERR) and mode-mixity for the Ti/Si interface

Ti thickness (Å)	Cr thickness (Å)	Steady ERR (J/m^2)	Delaminated length (μm)	Interfacial Fracture toughness G (J/m^2)	Mode mixity (°)
900	500	0.2281	129	3.45	6.8
900	1500	0.7540	414	3.55	22.6
900	2000	1.0055	527	3.72	27.5
900	3000	1.5145	649	4.55	34.2
900	4000	2.0345	696	5.70	38.4

For most interfaces, the measured interfacial fracture toughness will be greater than the work of adhesion [11, 79-81]. However, for low mode mixity loading and when plastic and visco-plastic dissipation is negligible, the fracture toughness should approach the work of adhesion which is essentially the Ti-Si bond energy for a given bond density. Using Si-Si bond energy of 325 kJ/mol and a bond density of 7x1014 bonds/cm^2, a conservative estimate for Ti-Si work of adhesion can be obtained as 3.77 J/m^2. In this paper, the measured interfacial fracture toughness for Ti-Si interface is 3 to 6 J/m^2 when the mode mixity approaches zero. This indicates that the proposed delamination test technique is a viable technique.

More SEM images for delaminated test strips are attached in Appendix 4-1.

4.4.2 Delamination Path Verification

One question should be answered in any delamination test is the whether the fracture occurs along the interested interface. To verify that the delamination did occur along the Ti/Si interface, an energy dispersive X-ray spectroscopy (EDS) was used to check the composition of the thin film strips before and after delamination.

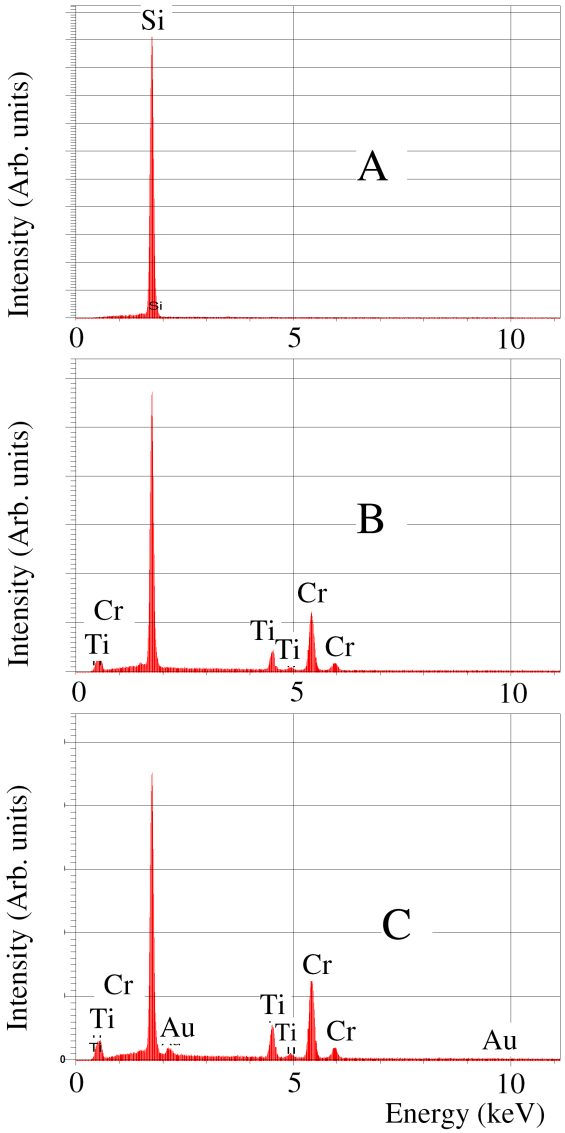

Figure 4.8 EDS spectra of the delaminated region (A), central (B), and undelaminated lateral (C) regions shown in Figure 4.7

As shown by Figure 4.8, in the region where the thin film strip was peeled off from the substrate, only Si appears as designed. In the central region of the undelaminated thin film strip (region B), Si, Au, Ti, and Cr appear, and in the two edge regions of the strip (region C), all materials (Au, Ti, and Cr) are present except Au, which appears only in the central region of the strip. It can be concluded that the delamination did occur along the Ti/Si interface but not along other interfaces. Also, there was no cohesive fracture in Ti or Si.

4.5 Effect of the Release Layer Shape

This section discusses how the release layer affects the delamination test.

4.5.1 Curling of the Test Strip as a Function of the Release Layer Shape

In implementation of the single strip decohesion test, the test strips usually curl up and therefore the crack front is perpendicular to the delamination direction. This does not always happen. The curling of the test strips depends on the shape of the release layer. If the release layer initiates the delamination from the strip center only, the test strip usually will not curl up due to the loss of adhesion from the strip side. When the release layer initiates the delamination from the strip side, the test strip will curl up since the test strip was constrained perpendicular to the delamination direction; the only deformation allowable is curling up.

Figure 4.9 shows the curling of the test strips with different release layer designs. Whenever the release layer shape is like (a) in Figure 4.9, the film strip tends not to curl up. In design (a), the driving force for delamination was lost due to the etching of the release layer along both sides of the strip. The film will not start delamination; rather the

superlayer curls towards to the center of the strip. While for design (b), the driving force will be kept and the thin film will start to peel off from the substrate with the gradual removal of the release layer. There is another design which also can have a successful delamination and will be discussed later.

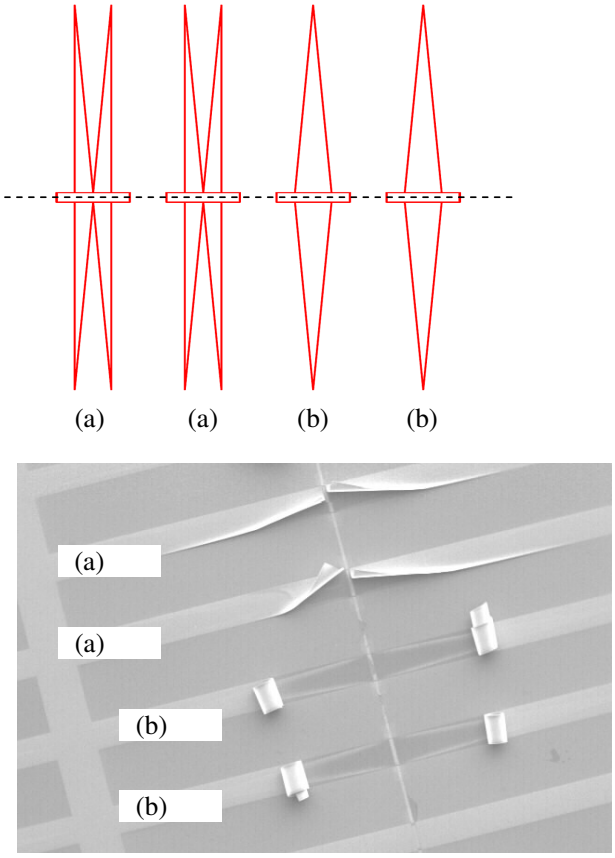

Figure 4.9 Relationship between curling and the release layer design

Figure 4.10 shows an optic image of the delaminated thin films strips corresponding to different release layer shapes. As shown in Figure 4.10, the thin film strips were either delaminated and curled up, or delaminated but without curling up. Whenever the thin film curls up, we call it a successful delamination test since all the

energy was used to overcome the interfacial fracture. Also the interfacial crack front is perpendicular to the delamination direction. While for an unsuccessful delamination, the crack front is more complicated. From Figure 4.10, it can be concluded that when the delamination was not initiated at the strip side, the test strip will not curl up.

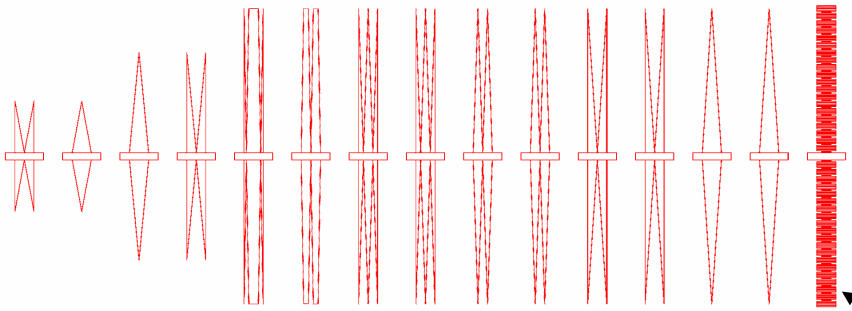

(a) Shape of the release layer

A fabricated ruler used to check delamination length

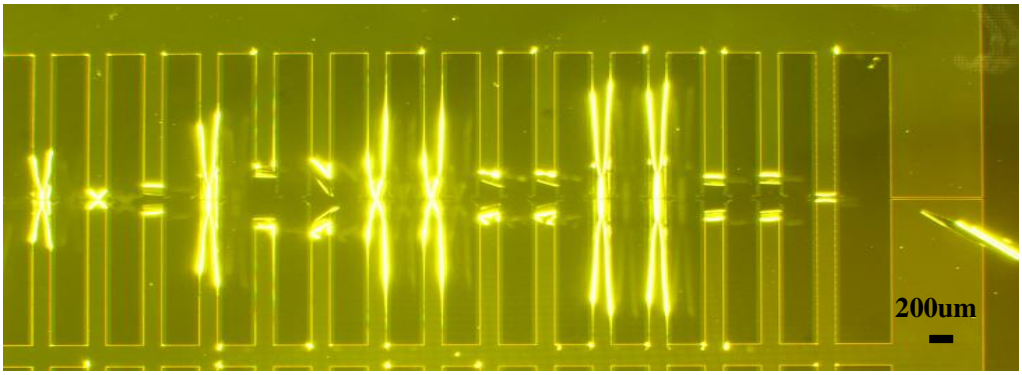

(b) Optical image of the delaminated strips

Figure 4.10 (a) Various shapes of the release layer (b) delaminated strips, corresponding to different release layer designs.

4.5.2 Effect of the Release Layer Height

As discussed in chapter 3, release layer with different triangle heights were designed and tested. As shown in Figure 4.11, release layer triangles with apex angles of 8.17º and 16.26º were tested. The heights of these triangles (i.e., the length of the release

layer) are 1400 µm and 700 µm respectively corresponding to the two apex angles. It is expected that with shorter release layer length, the delamination will be arrested at a shorter distance. The SEM images in Figure 4.11 demonstrate such expected behavior.

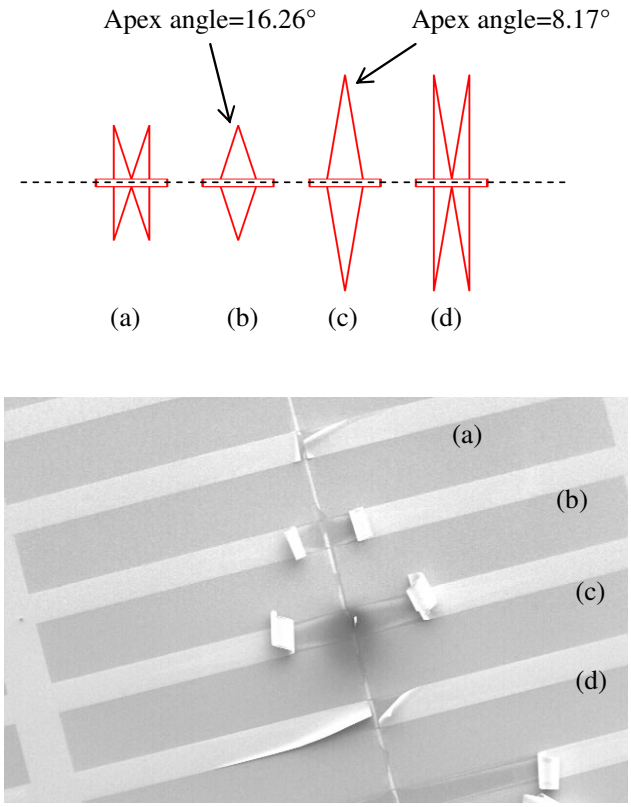

Figure 4.11 SEM images of delaminated strips with apex angles of 8.17 ° and 16.26º. The delaminated lengths are about 440 µm and 220 µm respectively.

As seen, when the apex angle is larger, the delamination was arrested at a shorter distance (about 220 µm in this sample). When the apex angle is smaller, the delamination propagates further to a distance of about 440 µm. At the location where the delamination ceases to propagate, the area of contact between the interface layer and the substrate is roughly the same for all triangles, irrespective of the apex angle, and this shows that the

apex angle of the triangle does not play a role in the interfacial fracture toughness value. However, it should be pointed out that in the cases tested, the crack area changes gradually as the delamination propagates, and therefore, the available energy for delamination propagation decreases gradually. Also, due to the triangular shape of the release layer, the interface contact area varies linearly with crack propagation.

4.5.3 Effect of the Adhesion Area in the Release Layer

In Figure 4.12, the release layer is designed in the way that the adhesion area of (a) and (b) is half of (c).

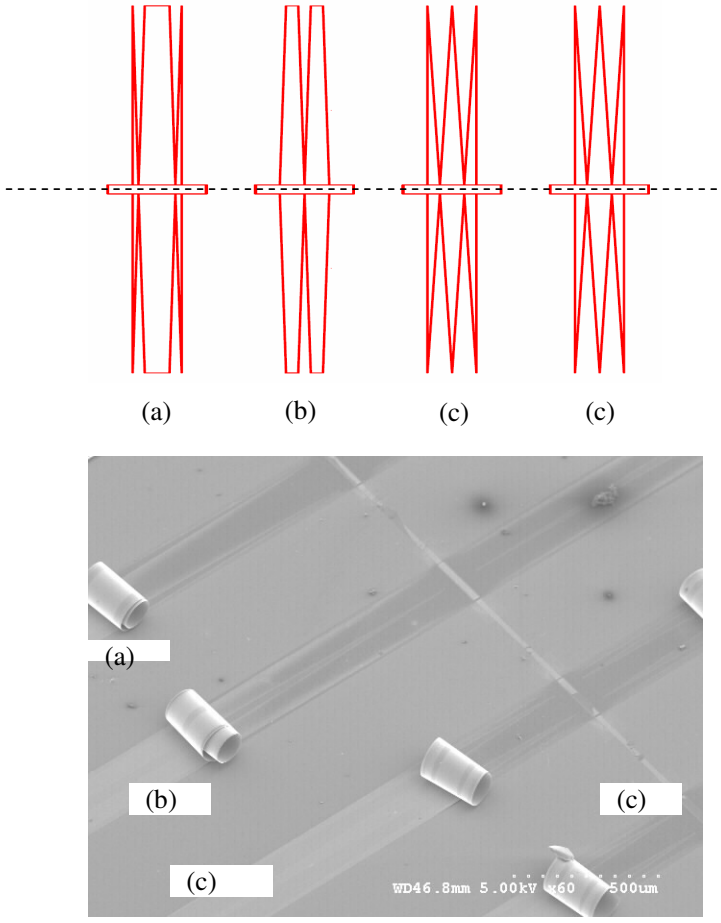

Figure 4.12 SEM images of delaminated strips with different contact area

The delamination shows that (a) and (b) delaminate the same length, which is about two times of (c). Again, it proves that the delaminated length is inversely proportional the adhesion area. Also, it should be noted that in design (a) and (c), even though the film strip edge is etched away, the film strip still curls up. The reason is that the delamination driving force is not lost due to adhesion area close to both sides of the strip. Because of that, the delamination prefers going along the direction perpendicular to the cut.

4.5.4 Effect of the Release Layer Width

To test the width effect to the interfacial fracture toughness, test strips with different width were tested. Table 4.3 shows that the width of the test strips starts from 100um wide all the way down to 4um.

Table 4.3 Test strip width

Test strip number	Strip width (μm)	Test strip number	Strip width (μm)
1	100	14	24
2	90	15	22
3	80	16	20
4	70	17	18
5	60	18	16
6	50	19	14
7	46	20	12
8	42	21	9
9	38	22	8
10	34	23	7
11	30	24	6
12	28	25	5
13	26	26	4

The triangle height of the release layer in these strips is designed to be the same height. If the strip width does not affect the energy release rate in each strip, the

delamination is expected to be the same length. Figure 4.13 shows the delamination of these test strips. Figure 4.13 (c) shows the wider strips while (a) shows the narrower strips. By correlating the strip number and measuring the delaminated length, it is found that the delamination length is roughly the same until the strips reaches a width of 9um. When the strip gets narrower than 9um, the delamination length sharply reduces. This is probably due to the loss of the thin film stress when the strip gets narrow.

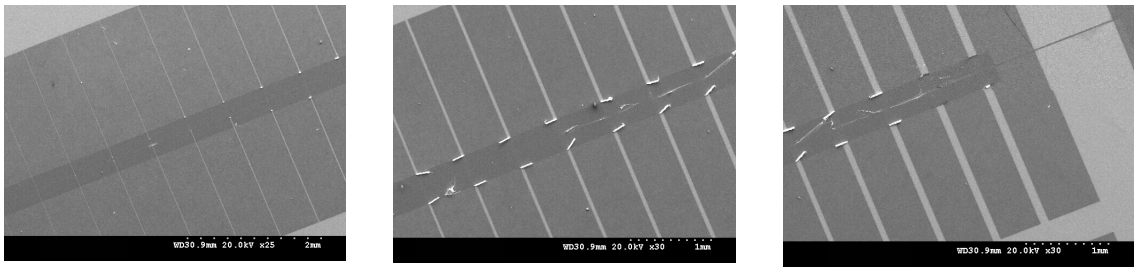

(a) (b) (c)

Figure 4.13 SEM images of delaminated strips with different widths

4.5.5 Effect of the Release Layer Thickness

The single strip decohesion test does not always yield good result. When the release layer is relatively thick, the delamination will not occur along the expected interface. Figure 4.13 shows an unsuccessful test in which the superlayer ruptures. In this test, the release layer, which is the gold, is around 100nm. When the release is thicker than the interface layer, a step will be generated along the interface, the delamination will occurs along this step and eventually rupture the superlayer and the interface layer. So a thin release layer should always be used.

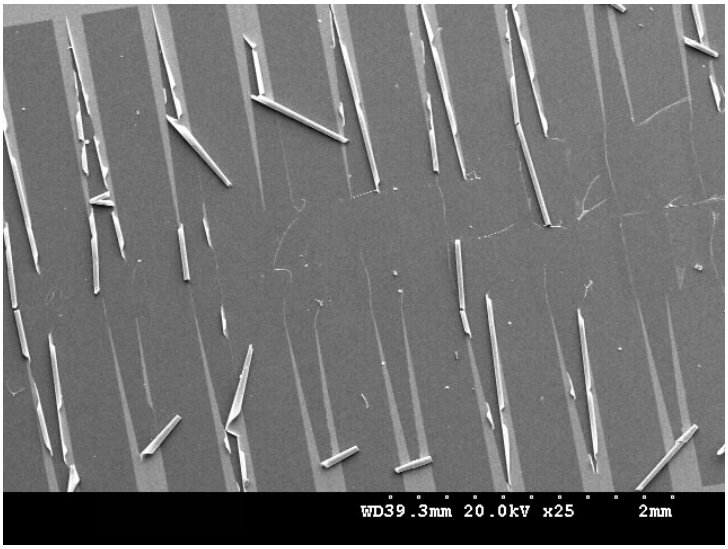

Figure 4.14 Superlayer/interface layer ruptures due to thick release layer

4.5.6 Release Layer Consisting of Discrete Shapes

As discussed in Chapter 3, some other kind of shapes such as discrete circles, discrete rectangles can also be used as long as these shapes can continuously or discretely vary the effective adhesion area along the delamination direction.

Figure 4.14 shows an optical image of the delaminated or fracture strips using discrete shapes as the release layer. As shown in Figure 4.14, most of the test strips do not curl up. One successful delamination is the test strip whose release layer has 8 rows of discrete shapes. Other test strips, which have less number of rows of discrete shapes in the release layer, do not delaminate. Rather, the superlayer and the interface layer in these test strips fracture or partially delaminate. Since the discrete adhesion regions are relatively easy to be peeled off and the delamination propagation can not go perpendicular to the cut simultaneously, the film strip can not curl up and therefore the drive force for delamination is lost. With multiple discrete adhesion regions, the delamination forced to go along the direction perpendicular to the cut.

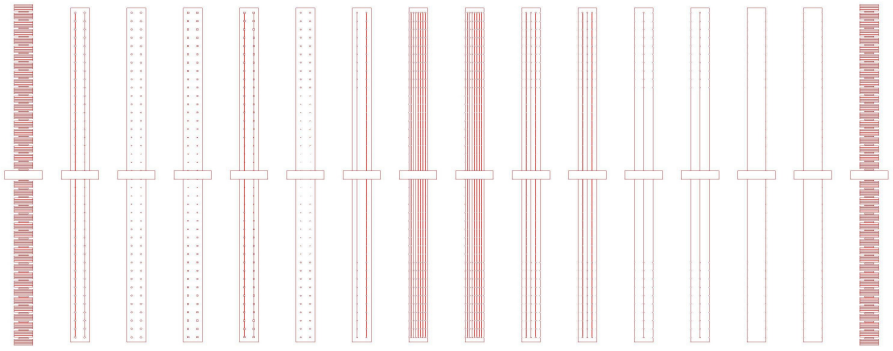

(a) Shape of the release layer

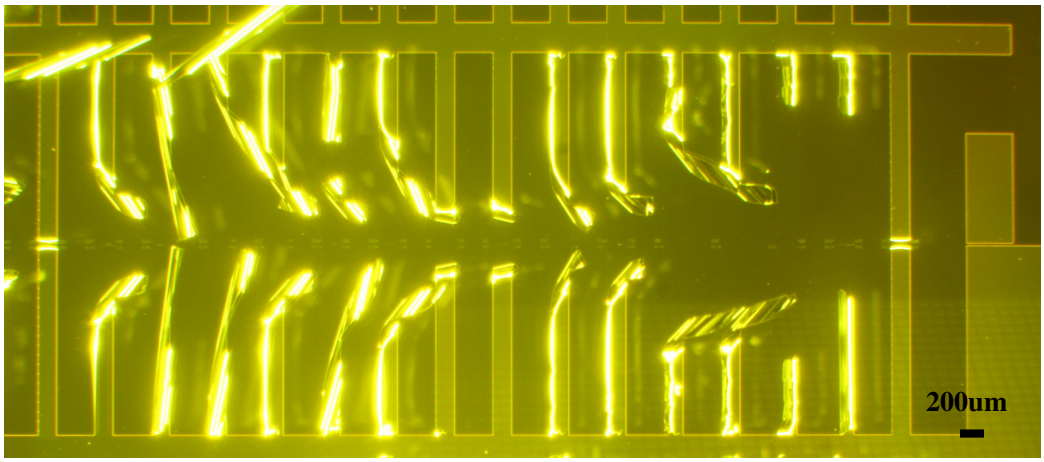

(b) Optical image of the delaminated strips

Figure 4.15 (a) Various shapes of the release layer containing discrete shapes (b) delaminated strips, corresponding to different release layer designs.

From this study, it confirms again that the film strip should be deformed in a certain way in order to delaminate the interface in the way a numerical solution is easy to be obtained. Accordingly, in a successful delamination test, the release layer should be designed in the way that could curl the film strip perpendicular to the cut. To do that, there should be sufficient adhesion along the strip side, or at least the adhesion area should be very to the strip side.

4.6 Effect of the Interface Layer Thickness

The effect of an interface layer thickness was investigated by the single strip decohesion test. In additional to the 100nm (nominal, actual 90nm) Ti tested, three different thicknesses were studied: 50 Å, 100 Å, and 200 Å.

The roughness of the bare Si wafer used in this study is less than 0.5nm. When a very thin layer Ti is deposited on the wafer, the interface between Ti and Si would be the same and this interface is independent of the interface layer thickness. Whereas the top of the interface layer with thicker Ti shows higher roughness. A rough interface between the interface layer (Ti) and the superlayer (Cr) is expected. Figure 4.16 shows a representative AFM image for a layer of 100Å Ti on the bare silicon wafer. Figure 4.17 and 4.18 show some representative AFM image for Ti film of 200Å and 50 Å respectively. For Ti of 50 Å, the AFM image tends to be unstable since the roughness of the thin film is very small.

Table 4.4 shows the roughness data of the Ti films. From the table, it can be shown that roughness of 1000 Å Ti is not significantly from the 200 Å Ti films.

The test results show that for 50 Å, there is massive delamination in the thin film strips. This could be due to the incomplete coverage of the Ti on Si. For 100Å and 200 Å Ti, the delamination results are shown in Table 4.5. It shows that thin Ti film does not necessarily make the interface weaker. The reason is due to the increased mode mixity. Also, to have better adhesion, the Ti film should be at least 100 Å.

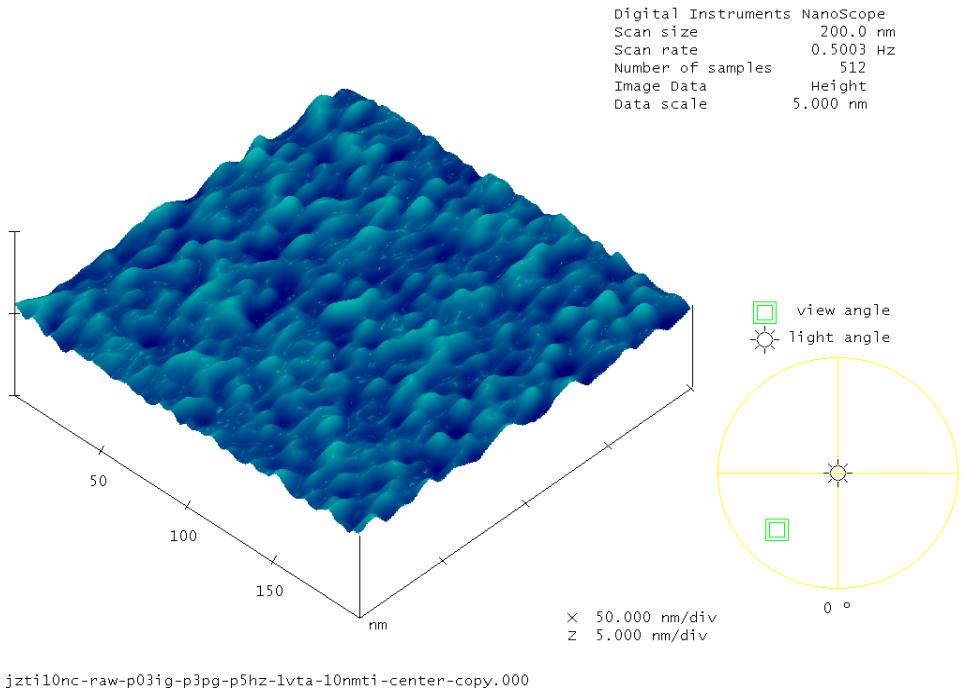

Figure 4.16 A representative AFM image for 100Å titanium on a bare silicon wafer

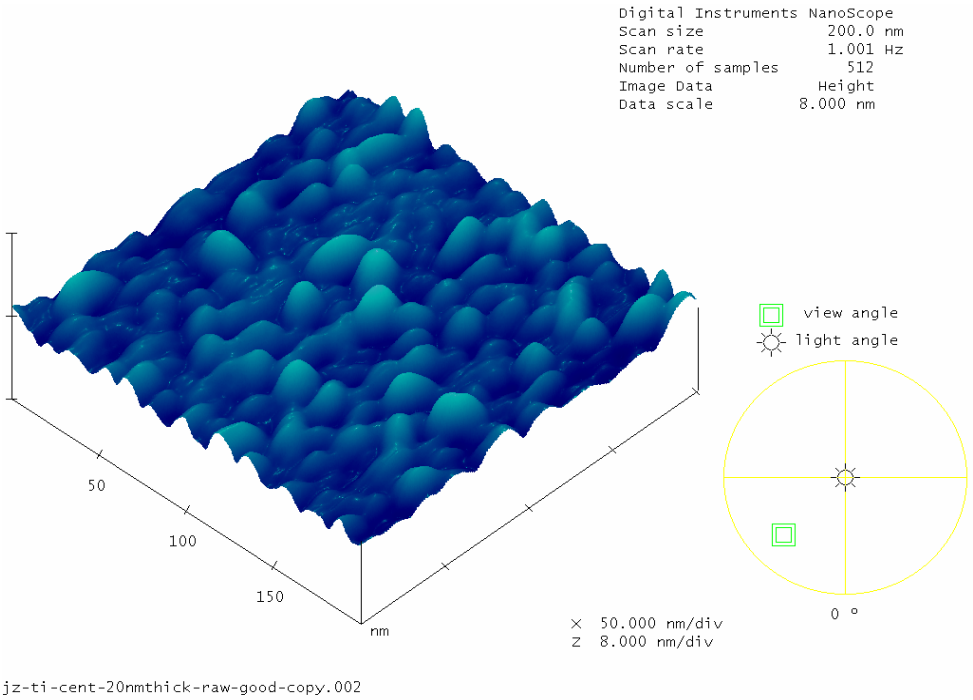

Figure 4.17 A representative AFM image for 200Å titanium on a bare silicon wafer

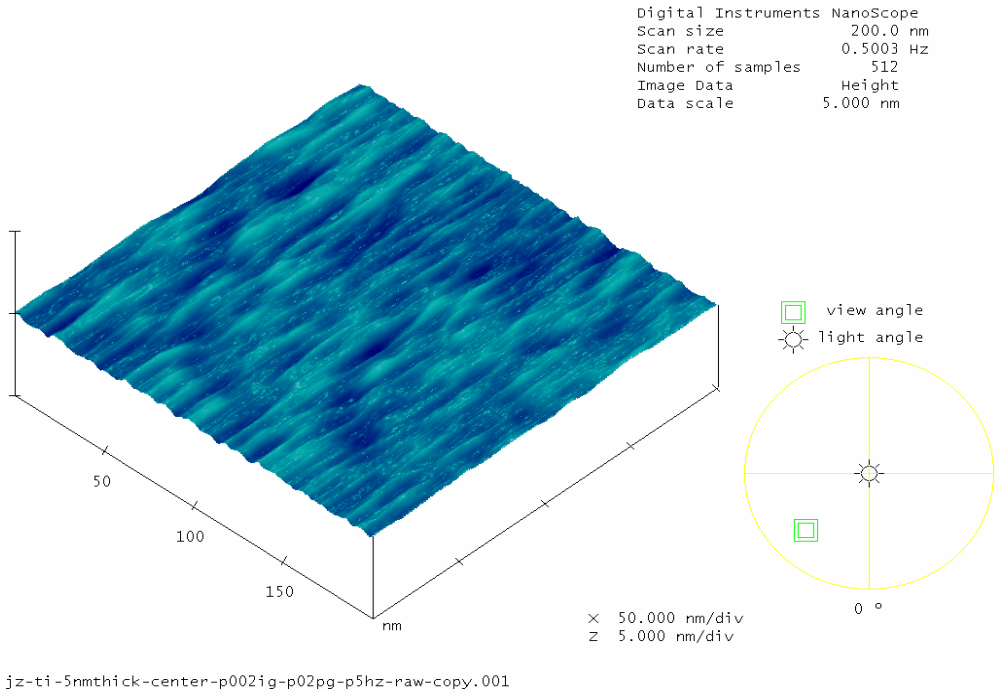

Figure 4.18 A representative AFM image for 50Å titanium on a bare silicon wafer

Table 4.4 Roughness of Ti films on bare Si wafer

Ti thickness (nm)	50Å	100Å	200Å	1000Å
Roughness(Ra, nm)	0.081	0.167	0.502	0.597
Z range (nm)	0.771	1.521	4.343	5.737
	unstable			

Table 4.5 Delamination of Ti/Si interface with thin Ti film

Ti thickness (Å)	Cr thickness (Å)	Steady ERR (J/m^2)	Delaminated length (μm)	Interfacial Fracture toughness G (J/m^2)	Mode mixity (°)
50	1500	0.754	>2000	Massive fail	
100	1500	0.754	235	6.26	45.5
200	1500	0.754	280	5.25	43.3
1000 (900)	1500	0.754	414	3.55	22.6

CHAPTER 5

ENERGY RELEASE RATE AND MODE MIXITY CALCULATION

5.1 Summary

This chapter presents the analytical solutions for the energy release rate and mode mixity of the single strip decohesion test. Finite element analysis was also performed to calculate the energy release rate and mode mixity.

5.2 Energy Release Rate

Figure 5.1 shows the schematic of the single strip decohesion test. The thickness of the superlayer and the interface layer are h_1 and h_2 respectively. Since the film stress diminishes as the interface decoheres, this energy release behavior is entirely controlled by elasticity. Two elements far ahead and far behind of the growing interfacial crack are chosen for the calculation. The width of the element is assumed to be Δa. The residual stress in the superlayer and the interface layer are σ_1 and σ_2 respectively. Assume the strain energy in element a and element b are U_a and U_b, then the energy release rate G_{ERR} then is

$$G_{ERR} = \frac{U_a - U_b}{\Delta a} \tag{5.1}$$

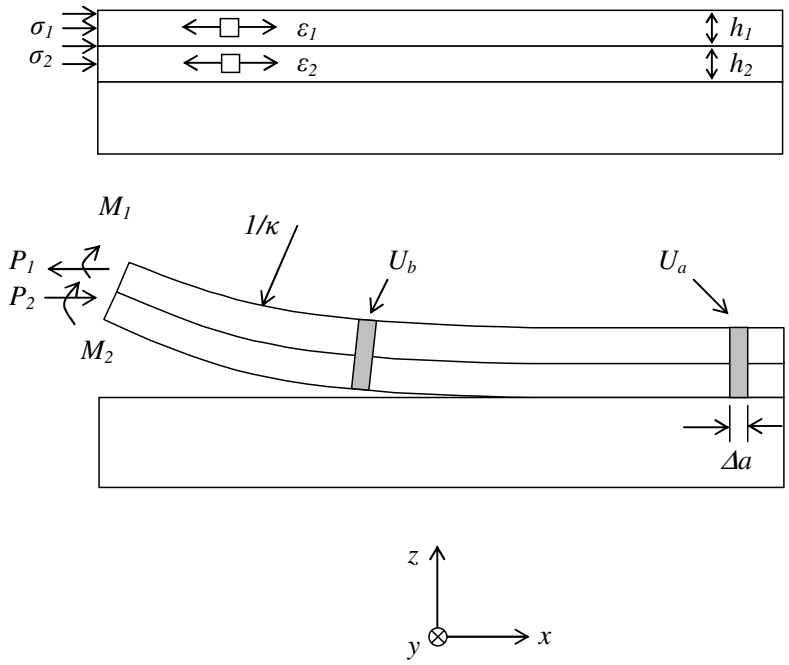

Figure 5.1 Schematic of the single strip decohesion test

In the single strip decohesion test, the width of the film is much larger the thickness of the film, so the element far ahead of the crack tip is in biaxial:

$$\sigma_{xx}^{i} = \sigma_{yy}^{i} = \sigma_i \tag{5.2a}$$

$$\sigma_{zz}^{i} = \tau_{xy}^{i} = \tau_{yz}^{i} = \tau_{xz}^{i} = 0 \tag{5.2b}$$

$$\varepsilon_i = \frac{\sigma_{xx}^{i} - v\sigma_{yy}^{i}}{E_i} = \frac{\sigma_i - v\sigma_i}{E_i} = \frac{\sigma_i}{E_i/(1-v)} = \frac{\sigma_i}{E_i'} \tag{5.2c}$$

$(i = 1, 2)$

σ_1 and σ_2 are the residual stresses in the two layers, while ε_1 and ε_2 are the corresponding residual strains. E_i' is the biaxial modulus for the thin film.

In a general three dimensional stress state, the elastic strain energy density can be calculated as follows:

$$u = \frac{1}{2}\left(\sigma_{xx}\varepsilon_{xx} + \sigma_{yy}\varepsilon_{yy} + \sigma_{zz}\varepsilon_{zz} + \tau_{xy}\gamma_{xy} + \tau_{yz}\gamma_{yz} + \tau_{zx}\gamma_{zx}\right) \tag{5.3}$$

The elastic strain energy density associated with each layer (i=1,2), per unit width, is:

$$\Delta U_a^i / (h_i \Delta a) = \frac{1}{2}\left(\sigma_{xx}\varepsilon_{xx} + \sigma_{yy}\varepsilon_{yy}\right) = \frac{1}{2}\left(\sigma_i \frac{\sigma_i}{E_i'} + \sigma_i \frac{\sigma_i}{E_i'}\right) = \frac{\sigma_i^2}{E_i'} \tag{5.4}$$

So for a bilayer thin film strip, the residual strain energy is:

$$U_a = \sum_i \Delta U_a^i = \sum_i \frac{\sigma_i^2 h_i \Delta a}{E_i'} = \left(\frac{\sigma_1^2 h_1}{E_1'} + \frac{\sigma_2^2 h_2}{E_2'}\right)\Delta a \tag{5.5}$$

When the super layer bears high tensile stress, the film bends upward after decohesion in an attempt to relax the strains. The resultant stresses in each layer can be related to the forces, P_i, moments, M_i and curvature, κ, defined in Figure 5.1, by:

$$\sigma_i(z) = P_i / h_i + z E_i' \kappa \tag{5.6a}$$

$$M_i / I_i = E_i' \kappa \tag{5.6b}$$

$$I_i = h_i^3 / 12 \tag{5.6c}$$

For the delaminated bi-layer,

$$\sum P_i = 0; \rightarrow \quad P_1 = P_2 = P \tag{5.7a}$$

$$\sum M_i = 0; \rightarrow \quad M_1 + M_2 = P\left(\frac{h_1 + h_2}{2}\right) \tag{5.7b}$$

Geometry requires that

$$M_1 = E_1' I_1 \kappa \tag{5.8a}$$

$$M_2 = E_2' I_2 \kappa \tag{5.8b}$$

Strain compatibility at the interface gives

$$-\varepsilon_1 + \frac{P_1}{E_1 h_1} + \frac{h_1 \kappa}{2} = -\varepsilon_2 - \frac{P_2}{E_2 h_2} - \frac{h_2 \kappa}{2} \tag{5.9}$$

From Equations 6.7 to Equation 6.9,

$$\kappa = \frac{6(h_1 + h_2)(\varepsilon_1 - \varepsilon_2)}{h_1^2\left(1 + \frac{E_1' h_1}{E_2' h_2}\right) + h_2^2\left(1 + \frac{E_2' h_2}{E_1' h_1}\right) + 3(h_1 + h_2)^2} \tag{5.10a}$$

$$M_i = E_i' I_i \kappa \tag{5.10b}$$

$$P = \left[\frac{E_1' h_1^3 + E_2' h_2^3}{6(h_1 + h_2)}\right]\kappa \tag{5.10c}$$

The elastic strain energy density in the delaminated region is:

$$U_b = \left\{ \sum_i \int_{-h_i/2}^{h_i/2} \frac{[\sigma_i(z)]^2}{E_i'} dz \right\} \Delta a = \left\{ \sum_i \left[\frac{P_i^2}{E_i' h_i} + \frac{12 M_i^2}{h_i^3} \right] \right\} \Delta a \tag{5.11}$$

The strain energy release rate is then (i=1,2):

$$G_{ERR} = \frac{U_a - U_b}{\Delta a} = \sum_i \frac{\sigma_i^2 h_i}{E_i'} - \sum_i \left[\frac{P_i^2}{E_i' h_i} + \frac{12 M_i^2}{h_i^3} \right] \tag{5.12}$$

Figure 5.2 shows the energy release rate for the Cr/Ti film strip calculation based on Equation 5.12. As shown in Figure 5.2, the energy release rate increases with the Cr superlayer thickness. This is also indicated by Equation 5.12.

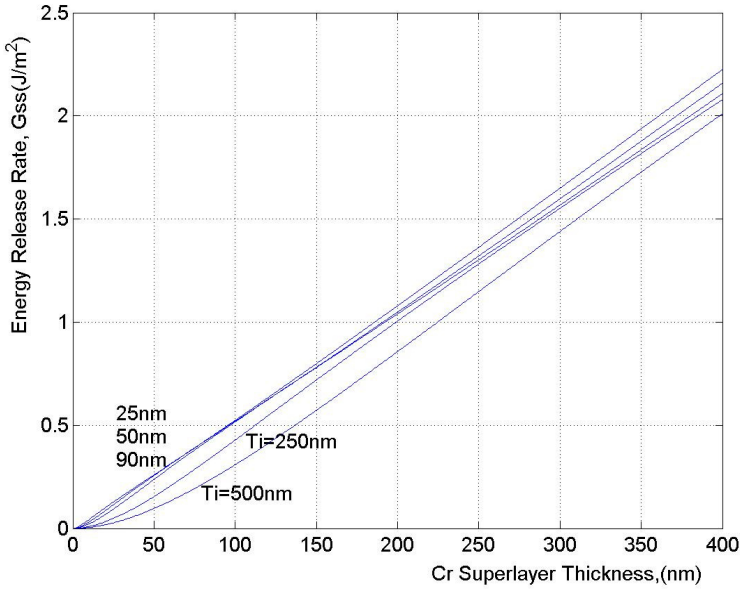

Figure 5.2 Energy release rate change with Cr superlayer thickness change for five different Ti thicknesses

Equation 5.12 applies when the interface layer with uniform width and uniform thickness is peeled from the substrate using a superlayer of uniform width, uniform thickness and uniform stress magnitude. However, in the proposed test, the contact width or the contact area of the interface film continues to increase due to the presence of the etchable release layer, and therefore, the energy release rate should be scaled accordingly.

Assume that the release layer extends to a length of L along the interface, as shown in Figure 3.4. For a particular combination of super layer thickness and stress, assume that the delamination arrests at a distance of a. It should be mentioned here test should be designed such that the delamination does not propagate past the release layer length, in other words, $a \leq L$. The energy release rate at the point where the delamination ceases to propagate is:

$$G_c = G_{ERR} \, L \big/ a \tag{5.13}$$

In which G_c is the critical energy release rate or the interfacial fracture toughness. G_{ERR} is the energy release rate calculated from Equation 5.12.

5.3 Energy Release Rate Calculation by Numerical Method

In addition to the analytical solution, a 3-dimentional finite element model is developed to simulate the crack propagation of this multilayer structure consisting of the substrate (Si), interface layer (Ti), and stressed superlayer (Cr). The thick substrate is modeled using linear solid elements. The interface layer and stressed superlayer are modeled using multilayered shell elements. The interface of the shell and solid elements are bonded using multipoint constraints (MPC) – these MPCs are also the primary

method of debonding the interface (i.e., grow the crack). The energy release rate is calculated by comparing the total elastic strain energy between two steps.

For the case with a single triangle release layer, a half symmetric model is used, as shown Figure 5.3.

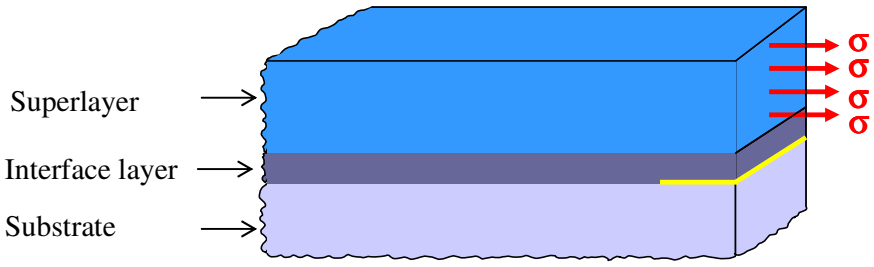

(a) 3D schematic of the test strip

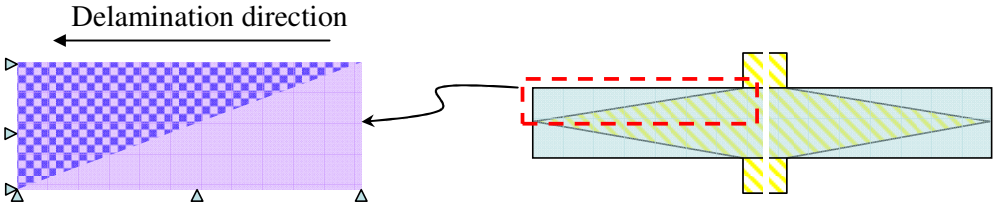

(b) Geometry used in the FEM

(c) Top view of the test strip

Figure 5.3 Geometry simplifications for finite element modeling

In the half symmetric model, the MPCs form the shape of a triangle. Figure 5.4 shows the layout of the MPCs in a test strip 150um long and 100um wide. In the simulation, the crack propagates in the step of every 10nm.

Figure 5.5 shows the interfacial crack propagation using MPCs. The interface layer is delaminated from the substrate. The release layer is not included in the model, and the function of the release layer is replaced by the MPC shapes, as shown in Figure 5.5. Delamination is enforced by incrementally releasing the MPCs. This method of

growing a crack has two advantages: 1) it allows the accrual of the large crack tip deformation, which would not be otherwise seen, 2) it allows for quick convergence of the large displacement given the high intrinsic stress loading. The detailed program for the MPC is in Appendix 5.1.

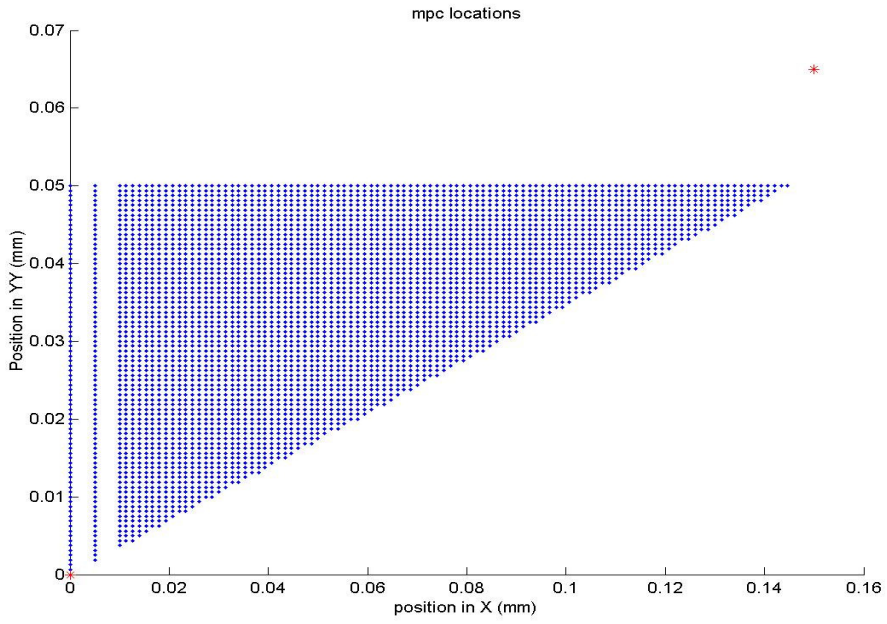

Figure 5.4 Multiple point constrains and the corresponding coordinates

As said, the MPC will release the bonding between the interface layer and the substrate step by step. By calculation the difference in elastic strain energy between two steps, the energy release rate can be calculated.

The comparison of the ERR from the analytical solution and from the FEM models are shown in Figure 5.6. From Figure 5.6, it can be concluded that the ERR by these two methods give roughly the same results. The difference between the analytical and the numerical analysis is due to the stress state assumption. In the analytical solution,

the stress in the superlayer and the interface layer is assumed to uniform biaxial stress, while in the numerical analysis, the biaxial stress state changes when the crack front moves.

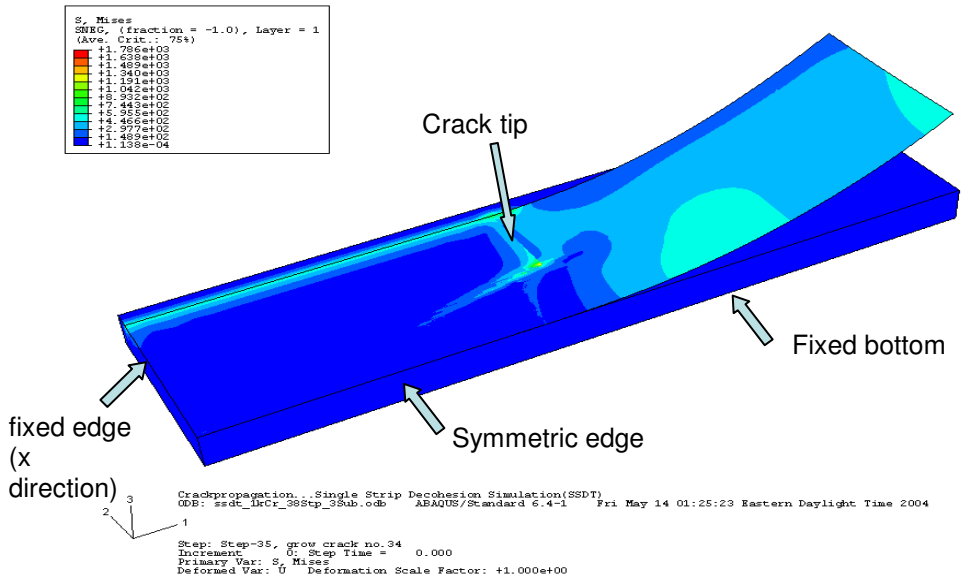

Figure 5.5 Interfacial crack propagation using MPCs for a 3 layer structure

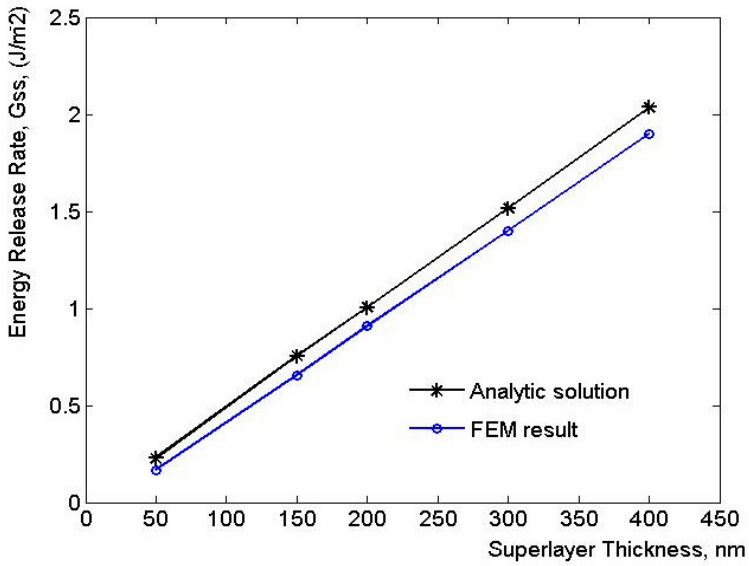

Figure 5.6 ERR for different superlayer thicknesses by analytical solution and finite element analysis

Also, from Figure 5.6, the energy release rate is mainly determined by the thickness of the superlayer (Cr), which is also indicated by the analytical solution.

When the release layer is in the form of multiple triangles, the MPC shape is changed accordingly, as shown in Figure 5.7.

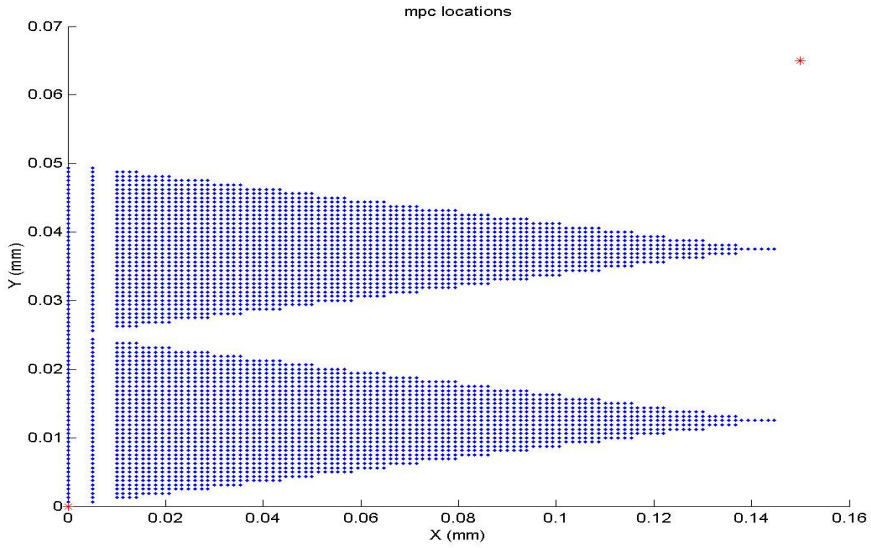

Figure 5.7 Multiple point constraint and the corresponding coordinates for a release layer with four triangles

When comparing to the release layer with a single triangle layer, there is literally no difference in the energy release rate. This also confirms the delamination test using multiple triangles as the release layer, which will be discussed in the next chapter. Strips with multiple triangle release layer delaminate to the same length compared to strips with a single triangle release layer.

Figure 5.8 shows the deformation of a strip containing multiple triangle release layers.

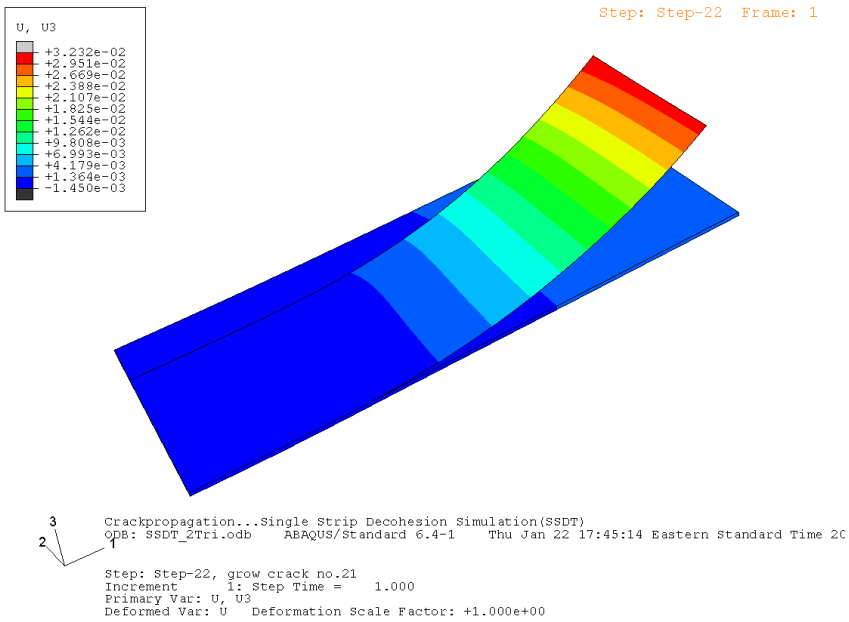

Figure 5.8 Delaminated strip containing multiple triangle release layer

5.4 Mode-mixity Calculation

The mode mixity can be calculated using the equation provided by Suo and Hutchison [82]:

$$\psi = \tan^{-1}\left[\frac{\lambda \sin \omega - \cos(\omega+\gamma)}{\lambda \cos \omega + \sin(\omega+\gamma)}\right] \tag{5.14}$$

where λ is a loading parameter and is a function of parameters such as load per unit thickness, moment per unit thickness, delaminating layer thickness; ω is a dimensionless scalar quantity which is a function of Dundur's parameters and the ratio of delaminating layer thickness to the substrate layer thickness; the angle γ is an angle

restricted to less than π/2. The theory for calculating of the mode mixity of a bilayer structure is attached in Appendix 5-2.

Different mode mixities can be achieved using different Ti and Cr thickness combinations. For Ti film of 90 nm thick, 50 nm thick superlayer (Cr) yields a phase angle less than 10°, while 600 nm Cr yields a phase angle of 43°. As shown in Figure 5.9, the mode mixity increases with the increase of Cr super thickness for a given thickness of Ti film, indicating increased shearing at the crack tip.

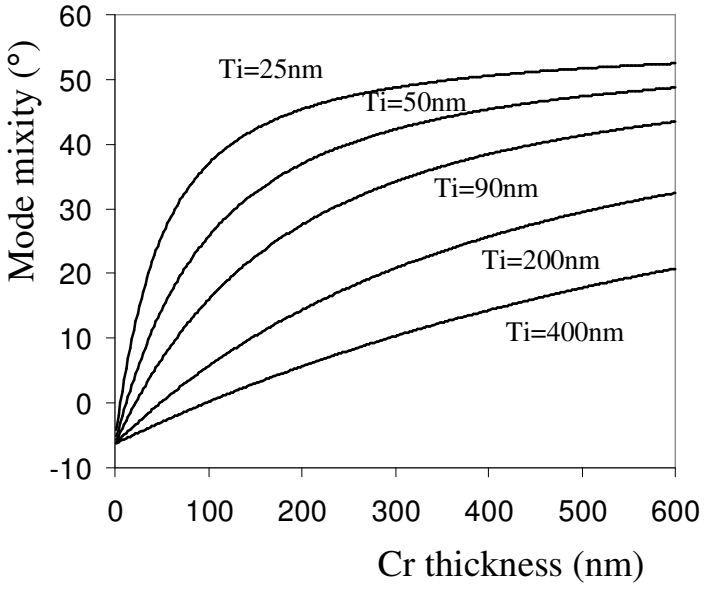

Figure 5.9 Variation in mode mixity angle with Cr superlayer thickness

5.5 Mode-mixity Calculation by Numerical Method

The mode mixity are also extracted using the Crack Surface Displacement (CSD) method [83]. The method is based on deriving fracture mechanics parameters from the relative displacements of the nodes along the crack surface that were initially coincident. The development of this method is as follows.

Equation (5.15) shows the relationship of behind the crack tip displacement to the complex stress intensity factor in interfacial fracture.

$$\Delta u_z + i\Delta u_x = \frac{1}{(1+2i\varepsilon)\cosh(\pi\varepsilon)} \frac{4Kr^{i\varepsilon}}{E^*} \left(\frac{2r}{\pi}\right)^{1/2} \tag{5.15}$$

Here, Δu_z and Δu_x are the displacements of once coincident points on the crack surface (x and z correspond to along the crack line and out of crack plane displacements, respectively), r is the distance from the crack tip, ε is the oscillation index, E^* is an effective modulus, and K is the complex stress intensity factor. Equation (5.16) shows the inherent coupling of the x and z displacements; this coupling complicates the decomposition of the energy release rate and the calculation of the mode mix. The solution of Equation (5.15) yields the relationships for the complex stress intensity factor (in terms of behind the crack tip displacements) and the mode mix.

$$\begin{aligned} |K| &= \frac{\sqrt{2\pi\left(1+4\varepsilon^2\right)\left(\Delta u_x^2 + \Delta u_z^2\right)} * \cosh(\pi\varepsilon)}{4h^{1/2}\left(r/h\right)^{1/2}} \\ \widehat{\Psi}^* &= \tan^{-1}\left(\frac{\Delta u_x}{\Delta u_z}\right) - \varepsilon \ln\left(\frac{r}{h}\right) + 2 * e \end{aligned} \tag{5.16}$$

In Equation (5.16), h is a characteristic specimen dimension and ψ^* is a mode mixity independent of length scale. In this form, Δu_x and Δu_z may now be substituted

with the FEM's output of change in displacement from once coincident nodes. Equation (5.17) gives the accompanying energy release rate.

$$G = \frac{|K|^2}{2E^* \cosh^2(\pi\varepsilon)} \tag{5.17}$$

ERR can be calculated between two steps in the analysis. Substituting ERR into Equation (5.17), will give the complex stress intensity factor. Using the determined complex stress intensity factor with Equation (5.16) will give the correct FEM evaluation nodes to determine the mode mix. Once the correct node is determined, the mode mixity can be calculated by Equation (5.16).

Figure 5.10 gives the comparison of mode mixity angles between the analytical solution and the finite element models for different superlayer thickness (Ti thickness was fixed at 90nm). For thinner Cr superlayer thickness, the difference is larger than thicker Cr superlayer thickness. The analytical results will be applied in this paper.

In the implementation of the Single Strip Decohesion Test, the release layer is etched away during the delamination propagation process. The delaminated thin film strips deform as if the release layer does not exist. The mode mixity is therefore assumed to be the same in these two cases. But the energy release rate for crack propagation will be different.

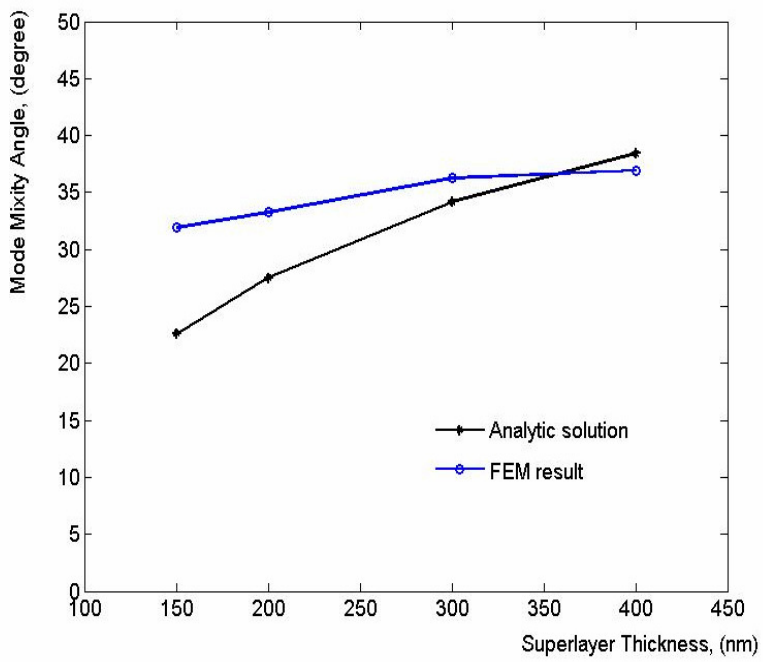

Figure 5.10 Mode mixity comparison between the analytical solution and the FEM model

5.6 Interfacial Fracture Toughness as a Function of the Mode Mixity

A phenomenological interface toughness law which reflects the strong mode dependence observed for some interfaces is [15]:

$$\Gamma_i(\psi) = \Gamma_i^1 \left\{1 + \tan^2\left[(1-\lambda)\psi\right]\right\} \qquad (5.17)$$

Where $\Gamma i\ (\psi\ )$ is the interface toughness and mode mix , $\Gamma_i^{\ 1}$ is the mode *I* toughness for $\psi = 0$, and λ is a parameter that adjusts the mode dependence. If $\lambda = 1$, there is no mode dependence. Representative values for many interfaces appear to lie in the range $\lambda \leq 0.3$ [84]. A least square curve fitting based on the data of Table 4.2, the relationship between Γ_i and ψ is:

$$\Gamma_i(\psi) = 3.37\left[1 + \tan^2(0.91\psi)\right] \tag{5.18}$$

The mode dependence λ is 0.09. The interfacial fracture toughness for Ti/Si interface for five mode mixities is plotted in Figure 5.11.

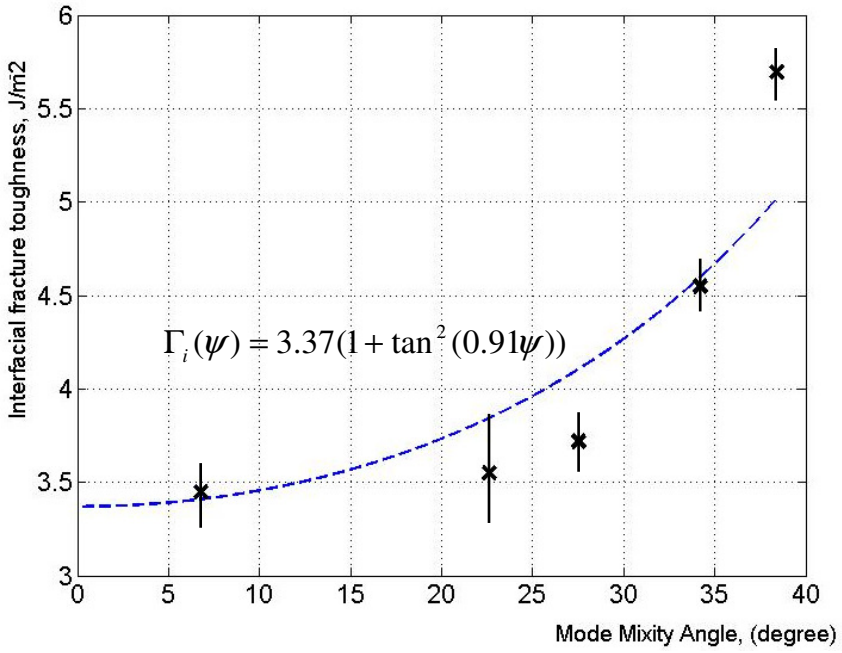

Figure 5.11 Interfacial fracture toughness as a function of mode mixity for Ti/Si interface

CHAPTER 6

APPROACH FOR INTERFACIAL FATIGUE MEASUREMENT

6.1 Summary

This chapter describes the approach for interfacial fatigue measurement. Experimental results will be presented in the next chapter.

6.2 Interfacial Fatigue Crack Growth Measurement and Deficiencies

As mentioned in chapter 1, existing literature is typically confined to monotonic loading in the interfacial delamination test, especially for nano scale and micro-scale thin films. This is partially due to the difficulty related to the fixture and application of cyclic loading for nano scale thin films. The monitoring of the delamination propagation under the cyclic loading is even more challenging. Therefore, there is a compelling and immediate need to develop techniques to study thin-film delamination propagation under cyclic loading.

In measuring the subcritical delamination, one measures the actual interfacial crack growth as a function of time or loading cycle. The crack growth rate is measured as a function of the applied delamination driving force. Under such cyclic loadings, the interface delamination propagation is dependent on ΔG (range of energy release rate), and the delamination propagation will occur even when the energy release rate is significantly lower than G_C.

6.3 Interfacial Crack Propagation Measurement Requirements

Given the shortcomings of the existing interfacial fracture toughness measurement tests discussed in chapter 1, one can say that an interfacial crack propagation test should meet the following criteria:

(a) The test sample should be prepared using the actual fabrication method to be able to create a representative interface;

(b) The test sample dimensions should be representative of the actual size used in the application; that is, the test should be able to handle micro-scale and/or nano scale thin film interfaces, as appropriate;

(c) The crack propagation should be captured very accurately; in other words, the crack length should be easily measurable, preferably at a resolution of few nanometers;

(d) The test method should simulate the actual usage stress conditions as closely as possible (both in sample preparation and crack development) and the test method should be able to cover a wide range of mode mixity;

(e) Deformations should be elastic since the physical problem demands an elastic solution;

(f) The test method should preferably lead to a mechanics-based analytical solution to extract fracture parameters;

(g) The test method should not involve extensive fixture and holding;

(h) The test method should be amenable to fatigue interfacial delamination propagation characterization; and

(i)The test should be easy to perform, repeatable, and efficient.

6.4 Proposed Thin Film Interfacial Fatigue Test

In this study, a new interfacial fatigue crack propagation characterization and monitoring test is proposed and implemented. This method uses a magnetically-actuated cantilever to drive the delamination along the interface of the cantilever and the substrate. As illustrated in Figure 6.1, a free-standing cantilever was fabricated on a substrate through standard microelectronic fabrication techniques such as photolithography and etching. A very thin layer of ferromagnetic material such as nickel, iron, or cobalt was sputtered on top of the cantilever at the tip region by physical vapor deposition. This whole set-up will then be placed in a magnetic field as illustrated in Figure 6.1a. When the external electromagnet is cyclically activated, the cantilever with the ferromagnetic magnetic material at the tip will deflect up and down, and such a cyclic motion will generate a non-contact cyclic loading at the interface of interest. The frequency of the fatigue load can be controlled by alternating frequency of the electromagnet, while the amplitude of the fatigue load can be controlled by the magnitude of the electromagnetic field.

To be able to monitor the interface crack propagation under magnetically-activated fatigue load, nano scale metal traces are used. Prior to the deposition and patterning of the cantilever, nano scale metal traces (e.g. 20nm wide on 20um long) was fabricated through electron-beam lithography and metal lift-off process on the substrate as illustrated in Figure 6.1. The nano scale metal traces form an array of parallel resistors and can be used to monitor the interfacial crack propagation at the metal cantilever/substrate interface through electrical resistance measurement. In other words, when the metal cantilever/substrate interface delaminates through a particular distance,

the physical connect between the cantilever and the nano metal trace is broken gradually, and therefore, the effective resistance of the array of parallel resistors increases. As the delamination propagates, more and more resistors are broken and the effective resistance continues to increase indicating the current location of the interfacial cracking. The resistance can be measured in-situ using the large probing pads (A and B). In the preliminary study, the cantilever is electrically conductive, while the substrate is non-conductive.

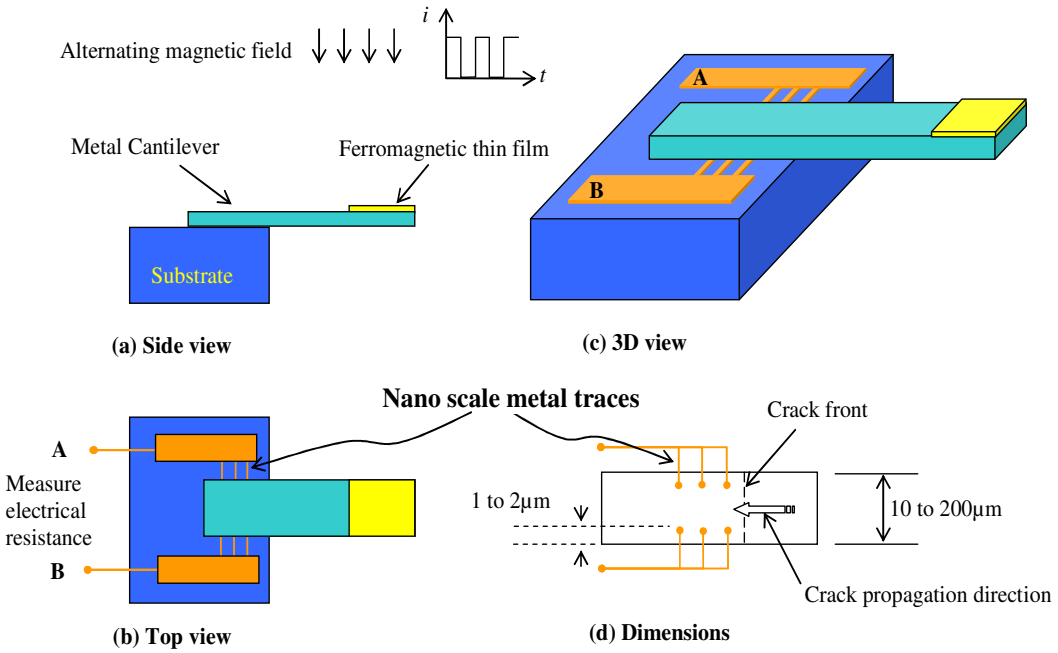

Figure 6.1 Schematic for interfacial fatigue test (interested interface: metal/substrate)

Another way to measure the crack propagation to measure the reflection angle of a laser light projected to the top of the cantilever. The interfacial crack propagation will affect the deflection of the cantilever. By measuring the reflection angle, the crack propagation can be measured, similar to the way that an atomic force microscope works.

But when the cantilever is less than 10um, focusing of the laser could be a problem. And therefore, this approach will not be pursued.

Only one cantilever is shown in Figure 6.1. However using clean-room fabrication techniques, hundreds cantilevers can be fabricated on the same substrate and can be simultaneously exposed to an external magnetic field covering the entire substrate. Also all of the electrical probe pads can be simultaneously in-situ monitored through an external data acquisition system, and thus the progression of delamination under each cantilever can be individually monitored. These hundreds of cantilevers will yield large amounts of interfacial crack propagation data using just one substrate. In addition to multiple cantilevers of identical dimensions, the cleanroom masking process will also permit the fabrication of arrays of cantilevers with different planar dimensions, and therefore, a wide range of test cases can be simultaneously studied through the proposed technique.

6.5 Fabrication of Nano Scale Metal Traces

As a first step, nano scale metal traces were fabricated on the substrate using electron beam lithography (EBL). E-Beam lithography is a process similar to photolithography, but uses an electron beam rather than UV light to expose resist. In photolithography the resolution is limited by the UV light wavelength, which must be much smaller than the feature size. This is not a problem for e-Beam lithography, since electron wavelength is only 0.2A to 0.5A 100 keV. Another advantage of e-Beam lithography is no physical mask needed, which eliminates costs and time delays associated with mask production. Furthermore patterns can be optimized and changed simply by using flexible CAD software.

As shown in Figure 6.2, a resist (ZEP 520A) is first applied on a substrate, and then patterned using the e-beam lithography tool (Figure 6.2c). The resist is then developed with ZED-N50 leaving nano scale patterns on the substrate, as shown in Figure 6.2d. Metal is then deposited on the entire substrate using an e-beam evaporator, as shown in Figure 6.2e. When the resist and metal is lifted-off with acetone, the substrate will have nano scale metal patterns as illustrated in Figure 6.2f.

The EBL system, JBX-9300FS™, features a 4nm diameter spot beam, vector scan, and a step-and-repeat stage, and is capable of varying the beam size widely. Its dynamic correction system eliminates defocusing resulting from beam deflection. The system has less than 20nm field stitching accuracy and less than 25nm overlay accuracy at 100kV. Metal traces narrower than 10nm can be fabricated using the EBL system that is available at Georgia Institute of Technology. This e-beam lithography tool is one of the most sophisticated instruments in Georgia Tech. How to use the tool to make high fidelity features is not the intention of this thesis, even though it takes significant amount efforts to fabricate these features. The detailed process to use the tool and the recipes to fabricate the feathers are attached in the Appendix 6-1.

6.6 Fabrication of the Free-Standing Cantilever

The fabrication process for the free-standing cantilever is shown in Figure 6.3. As seen, starting with the substrate with nano scale metal traces (Figure 6.3a), we will deposit the cantilever metal of desired thickness (Figure 6.3b). The deposition process will be similar to the process that is used in the actual application of the metal. Once the metal and electrical probing pads are patterned through photolithography (Figure 6.3c), another photoresist layer is applied and a window for ferromagnetic material deposition is

open (Figure 6.3d). Once the ferromagnetic material is deposited (Figure 6.3e), a final photolithography process (Figure 6.3f) is needed to etch the substrate so that the cantilever will be free-standing (Figure 6.3g). For the sake of simplicity, Figure 6.3 legend shows some example materials commonly used in microelectronics and other applications. As seen, the substrate is Si or Si with SiO_2 on top, the nano scale metal traces are Ti/Au, the cantilever is Cr, and the ferromagnetic material is Ni.

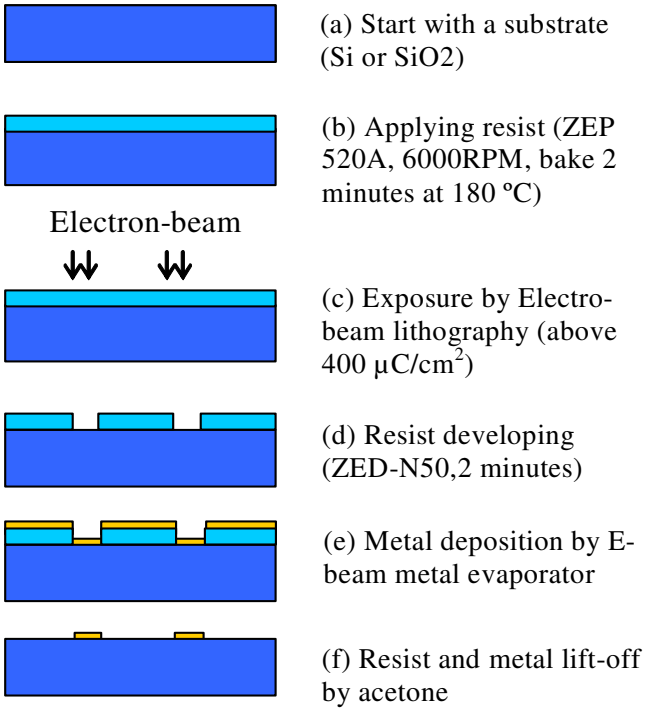

Figure 6.2 Fabrication process for nano scale metal traces using E-beam lithography

6.7 Deposition of Ferromagnetic Material

One unique aspect of the proposed test method is to apply a non-contact cyclic loading to the interface by magnetic actuation. Compared to electrostatic and piezoelectric actuation mechanism, electromagnetic field can be used to exert higher

force and at frequencies ranging through several orders of magnitude (as high as several hundred MHz in this application). The electromagnetic field can be kept at a significant distance away from the cantilevers, and this means that the specimen can be placed in an enclosed environment of desired temperature and humidity condition, and the magnetic field can be externally applied. The external magnetic field can be driven by common low-cost, low-voltage controllers [85]. By activating the external magnet cyclically, a cyclic pulling force can be generated on the cantilever, and therefore, the force application is simple.

After the cantilever is patterned and before the substrate is etched, the ferromagnetic material can be deposited through a mask on top of the cantilever at desired locations, as illustrated in Figures 6.3d and 6.3e. Thus, if the presence of the ferromagnetic material is desired only near the tip region of the cantilever, then the mask will have an opening near the tip region of the cantilever. If it is desired to have the magnetic actuation through the entire released length of the cantilever, then the mask will have such an appropriate opening, and therefore, a uniformly distributed force can be applied along the released length of the cantilever. It should be stated that using the masking process, on the same substrate it is also possible to have some of the cantilevers activated at the tip, while some others are activated through their entire released length.

6.8 In-Situ Nano scale Crack Propagation Monitoring

The interfacial delamination propagation was monitored through the nano scale metal traces on the substrate. As mentioned earlier, nano scale metal traces will be sandwiched between the cantilever metal and the supporting substrate, as shown in Figure 6.1d. Once the interfacial crack propagates, the connection between the metal

traces and the conductive cantilever metal will be broken. These nano scale metal traces are 20nm wide and 10 nm thick. With such a cross-section, the electrical resistance of, for example, Ti/Au traces will be 60 to 100kΩ over a length of 100 μm. As the interfacial crack propagation will be monitored through the change in electrical resistance as the parallel resistors are sequentially broken one by one, the absolute magnitude of resistance of each metal trace is provided here as a reference, and will not be explicitly required for monitoring the interface crack propagation. As long as the metal traces are uniform in dimension, the sequential breaking of the traces will provide relative resistance increase for crack monitoring purposes.

6.9 Energy Release Rate

Although the fatigue crack growth of an interfacial crack is different from the fatigue crack propagation in homogeneous materials, researchers still try to adopt models from classical fatigue crack analysis in which cohesive cracks are studied. Research on interfacial fatigue crack propagation is still in infancy, and there are only a handful of papers that address this [64, 70, 86-90].

As a first step, we will develop a relationship between the fatigue crack growth rate and the energy release rate range as described by Paris Law as:

$$da/dN = C(\Delta G)^m \tag{6.1}$$

Where da/dN is the fatigue crack growth rate per cycle, ΔG is the range of energy release rate for the fatigue cycle and C and m are constants to be experimentally determined. Through conducting experiments with a wide range of cantilever dimensions

and with the cantilever metal deposited through different processes, it is also possible to determine the dependency of C and m on such geometry and processing parameters.

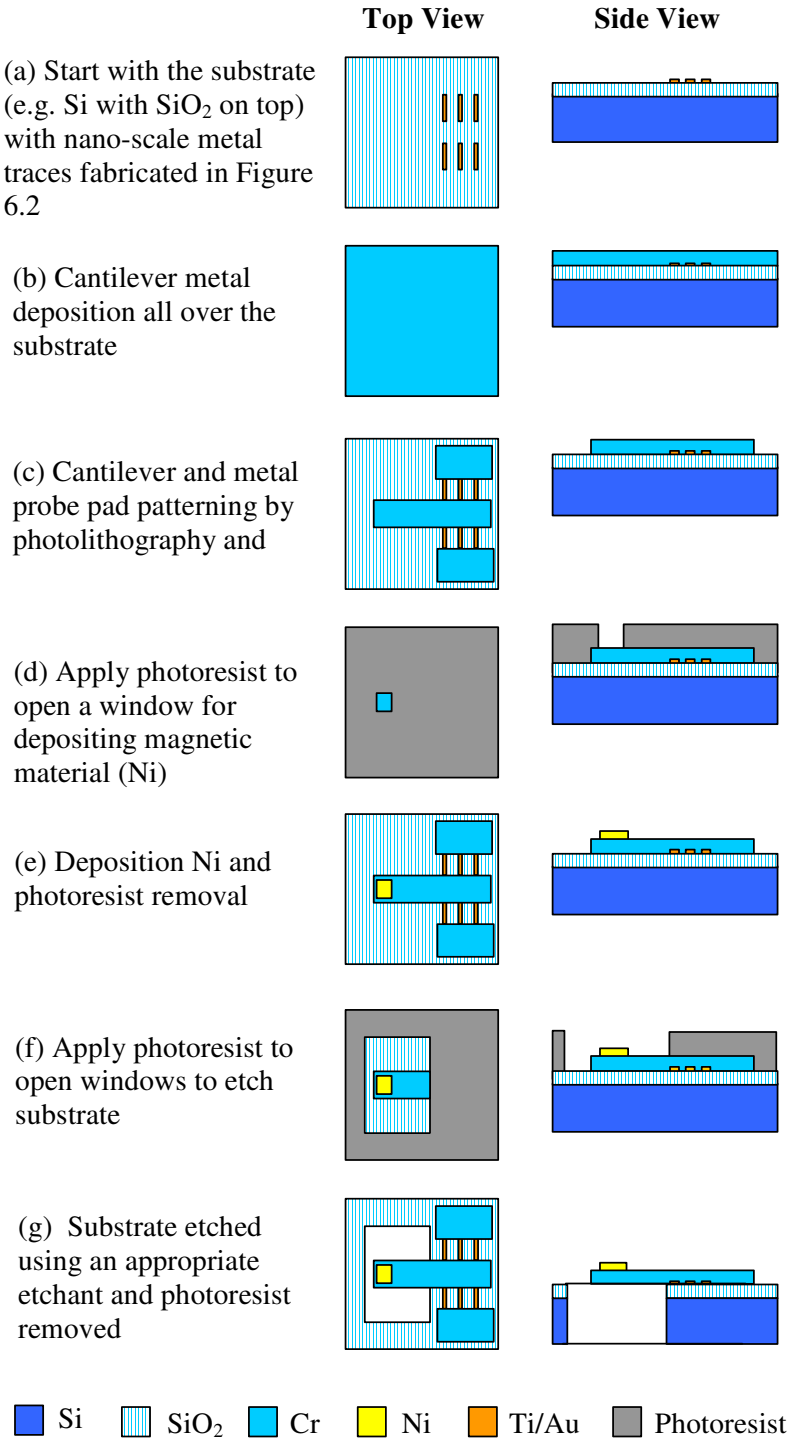

Figure 6.3 Experimental test vehicle fabrications

The energy release rate can be obtained either through analytical formulation or through finite-element modeling. For example, if all materials are assumed to be linear elastic, the energy balance of the structure can be expressed as:

$$\frac{dW}{da} = \frac{dU}{da} + \frac{d\Gamma}{da} = \frac{dU}{da} + BG \tag{6.2}$$

Where W is the work due to external loading, U is the strain energy, Γ is the fracture energy needed to drive the crack growth, a is the crack length, B is the width of the cantilever or the interface, and G is the energy release rate. Assuming no strain energy change for the substrate, one can determine the magnitude of G for a given magnetic force P applied at the tip of the cantilever as

$$G = \frac{1}{B}\frac{3P\delta}{2L} = \frac{1}{B}\frac{9EI_z}{2L^4}\delta^2 = \frac{1}{B}\frac{L^2}{2EI_z}P^2 = \frac{3}{8}\frac{t^2}{L^4}\delta^2 \tag{6.3}$$

Where δ is the deflection of the cantilever tip due to the application of P, L is the length of the cantilever, E is the modulus of elasticity of the cantilever material, and Iz is the area moment inertia of the cantilever. When the cantilever is flat without any magnetic actuation, the available energy for crack propagation is zero, and therefore, G from the above equation for the maximum P in a given fatigue cycle is the same as ΔG to be used in the Paris Law. It should be noted that the free or released length of the cantilever L will continue to increase as the crack propagates, and this increase in L can be incorporated in the analytical model, if needed.

CHAPTER 7

EXPERIMENTAL RESULTS ON INTERFACIAL FATIGUE TEST

7.1 Summary

This chapter presents the results of the interfacial fatigue test for micro contact springs. It starts with the fabrication and characterization of the nano-metal traces, followed by the fabrication and the characterization of the micro contact magnetic springs. Finally the test for the interfacial fatigue was performed and the results were analyzed. Figure 7.1 shows the outline of this chapter.

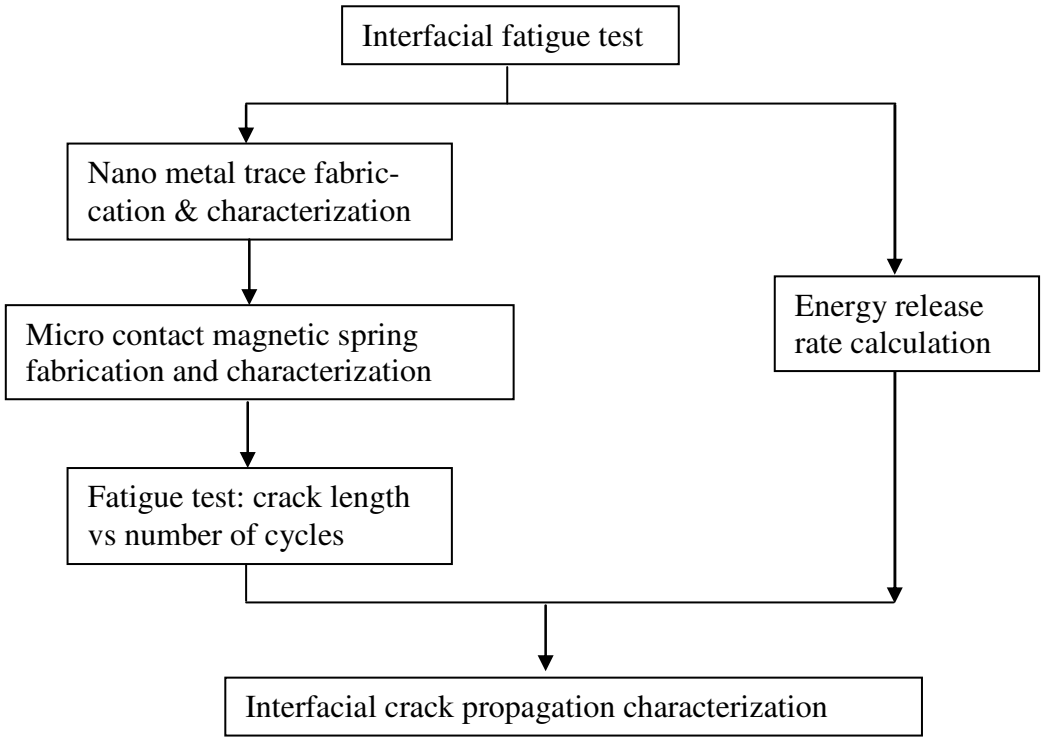

Figure 7.1 Outline of interfacial fatigue test for micro contact springs

7.2 Nano Metal Trace Fabrication and Characterization

7.2.1 Nano Metal Trace Fabrication

Based on the process described in chapter 6, nano scale metal traces were fabricated using JEOL JBX-9300FS, an E-beam lithography tool. Figure 7.2 shows the flowchart for the fabrication. Figure 7.3 highlights some major steps in the pattern preparations. The job deck file and the scheduled can be found in Appendix 7-1.

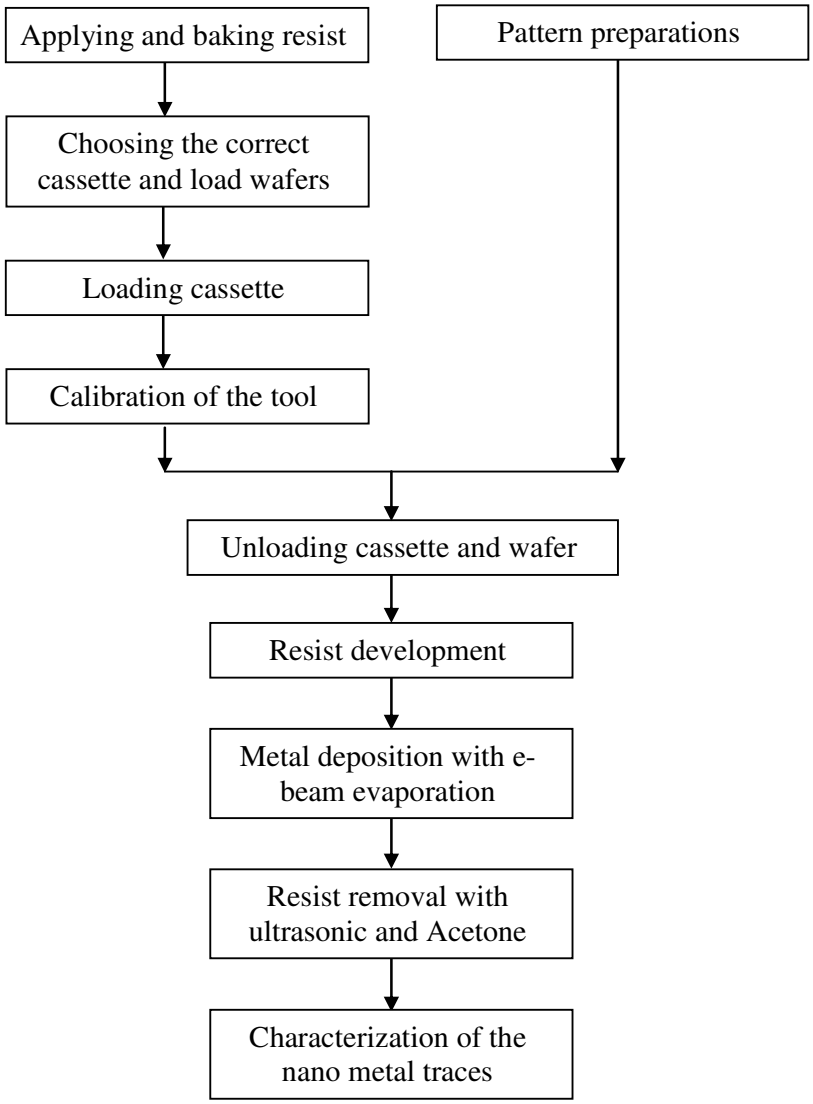

Figure 7.2 Flowchart for fabrication of the nano metal traces

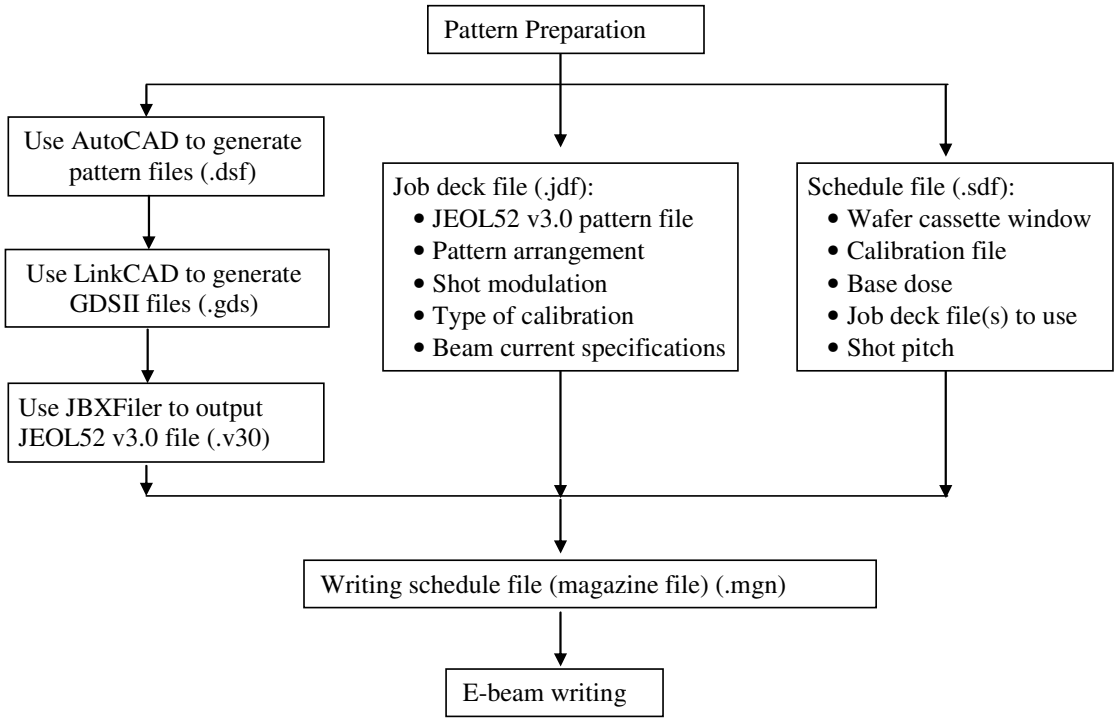

Figure 7.3 Pattern preparations for E-beam lithography

In this study, the fabrication process was optimized in terms of the exposure dose, the thickness of the resist, the feature size, etc. Different resists were used and ZEP520A by ZEON Corporation was found to yield the best results.

Figure 7.4 shows some fabricated Au traces that are 20nm nm wide and 20nm thick with a spacing of 400nm. The nano metal trace consists of 10nm thick Ti adhesion and 10nm thick Au. Both metal layers were deposited sequentially with electron beam evaporation followed by a lift-off process to obtain high-fidelity features. Figure 7.5 shows how these nano metal traces look like under the atomic force microscope. In Figure 7.5, the metal traces are 20nm thick, 50nm wide with 200nm pitch.

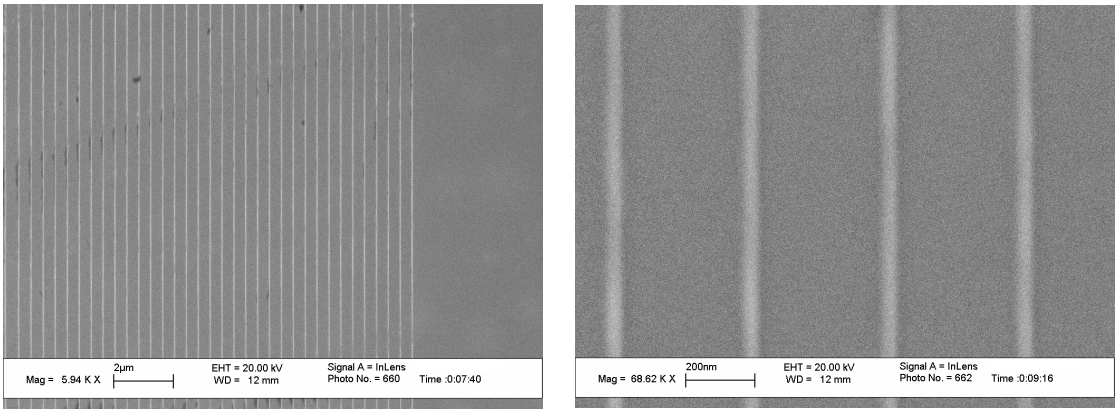

Figure 7.4 Ti/Au metal traces (20nm wide) fabricated with E-beam lithography

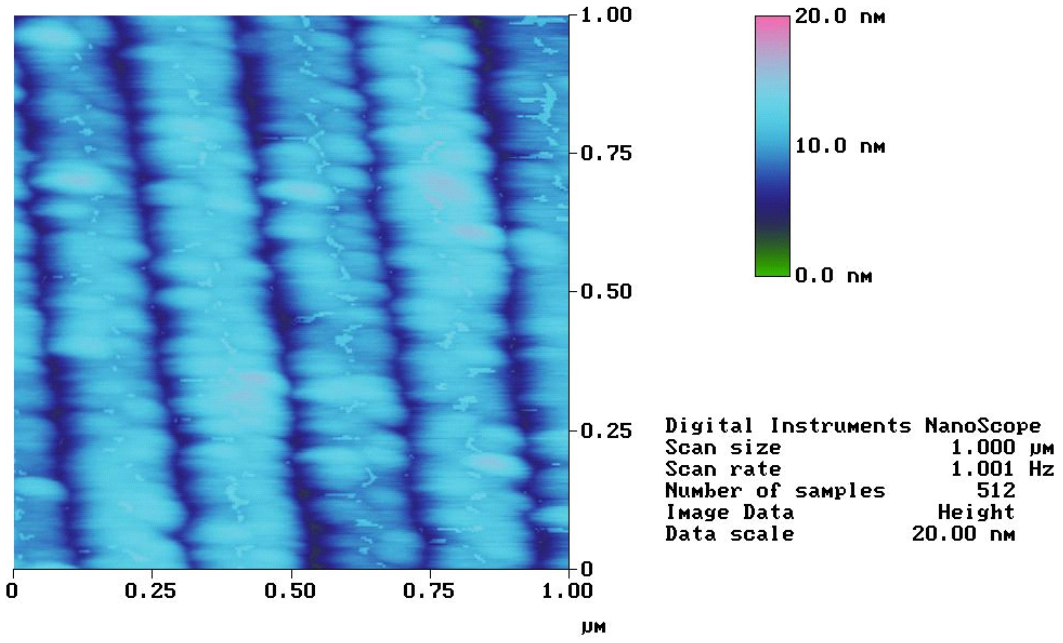

Figure 7.5 AFM image of Ti/Au metal traces (50nm wide, 200nm spacing) fabricated with E-beam lithography

Figure 7.6 shows a metal strip superimposed onto an array of nano scale metal traces. The large metal strip, 50um wide and 200nm thick, was patterned by the traditional photolithography and fabricated onto the substrate with nano metal traces. The advantage of doing so is to reduce the processing time using E-beam lithography.

Since E-beam lithography is not a batch process, exposing the area of a small metal pad will take tremendous amount of time. Besides, the thickness of the metal strip is limited by the thickness of the resist used in E-beam lithography, which usually is about 100nm thick. So a sequential processing of E-beam lithography followed by the traditional photolithography is used. The alignment between the nano metal traces and the large metal strip is enabled by fabricating some tiny fiducial with E-beam lithography. These fiducials will be used as the alignment marks during the photolithography process. Usually these fiducials consist of very fine lines, 20um wide and 1000um long. It does not take very long time to expose lines at this dimension while the feature is large enough to be used as an alignment mark.

Figure 7.6(b) shows that the overlapping between the metal strip and nano metal traces is about 2 to 3um. Compared to the width of the metal strip, which is 50um to few hundreds micrometers, the overlapping is considered to be relatively small and therefore would have minor effect to change the interface integrity of the metal strip and the substrate. If the metal strip is peeled off or released from the substrate by some external force to become a free standing structure or cantilever, the nano traces can detect the interfacial crack propagation between the metal and the substrate.

7.2.2 Electrical Resistance Characterization of Nano Metal Traces

Electrical resistance characterization was performed to check the uniformity and continuity of these nano metal traces. To do this, eight pairs of metal probe pads were fabricated such that the electrical resistance measurement can be done for eight resistors in parallel, seven resistors in parallel, six in parallel, and all the way down to a single resistor, as illustrated in Figure 7.7. If the resistance of a single nano scale resistor is R,

then the effective resistance of the *n* resistors in parallel will be *R/n* if all of the traces are identical in shape.

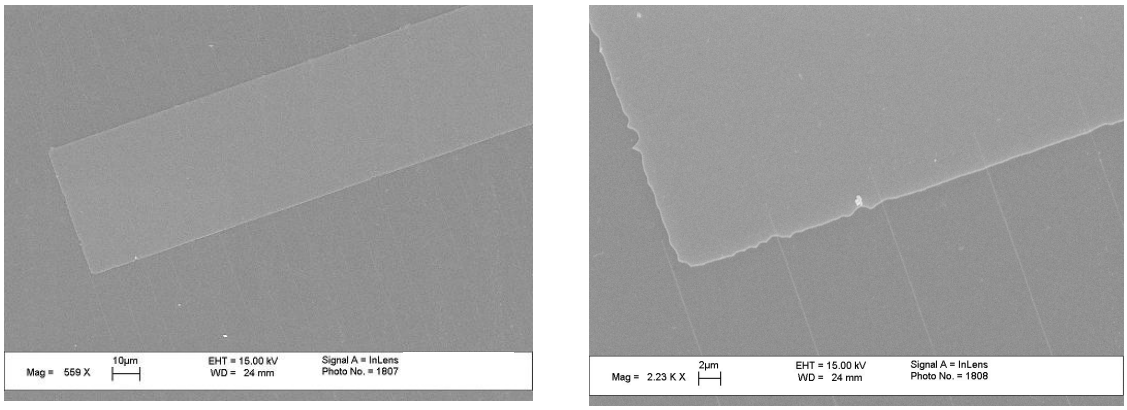

(a) (b)

Figure 7.6 Nano Au traces (20um wide) forming a centipede pattern with a 50µm wide metal strip in the center

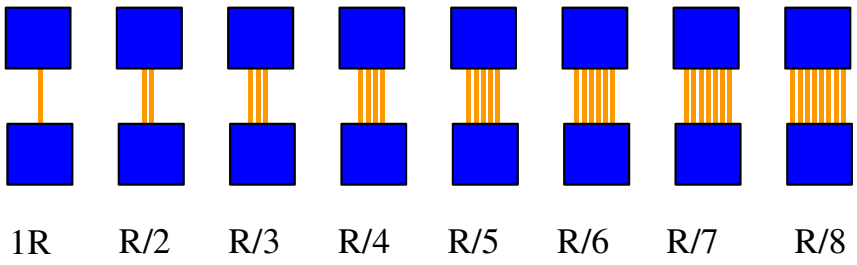

Figure 7.7 Schematic of resistance characterization for nano scale metal traces. Each pair of metal pads connects 1 to 8 nano traces.

Figure 7.8 shows one portion of the photo mask used to fabricate the metal pads with conventional photolithography. The mask is designed in the way that the metal pads can be superimposed onto those prior fabricated nano metal traces (or wires).

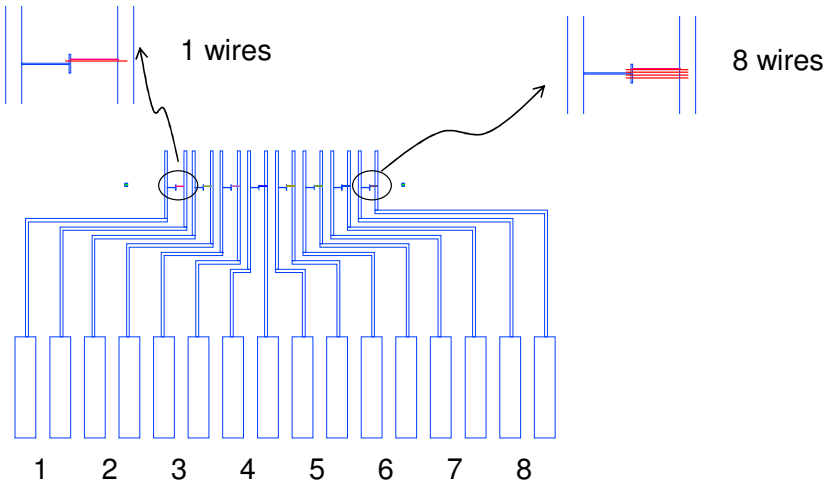

Figure 7.8 Photolithography mask used for electrical resistance characterization

Figure 7.9 shows some SEM images for this kind of characterization. The nano metal traces are connected to large metal strips fabricated with photolithography.

Table 7.1 shows the measured electrical resistance of Ti/Au nano metal traces (40nm wide, 20 nm thick and 500 μm long). As seen, the resistance of one trace is about 105.1 KΩ, and the effective resistance approximately scales down as *R/n* as more and more parallel resistors are included in the array.

Table 7.2 shows the measured electrical resistivity of the Au and Ti thin film used in the same process to fabricate these nano metal traces. The resistivity was measured with the Signatone® four point probe on wafers with 20nm Au or Ti thin film. Based on the measured resistivity of Au and Ti films, the electrical resistance of the nano metal traces can be calculated. Figure 7.10 shows the comparison between the measured value and the calculated value using electrical resistivity. Considering the variation during the

fabrication process, the metal traces show a good uniformity and should be able to serve the purpose of the interfacial fatigue testing.

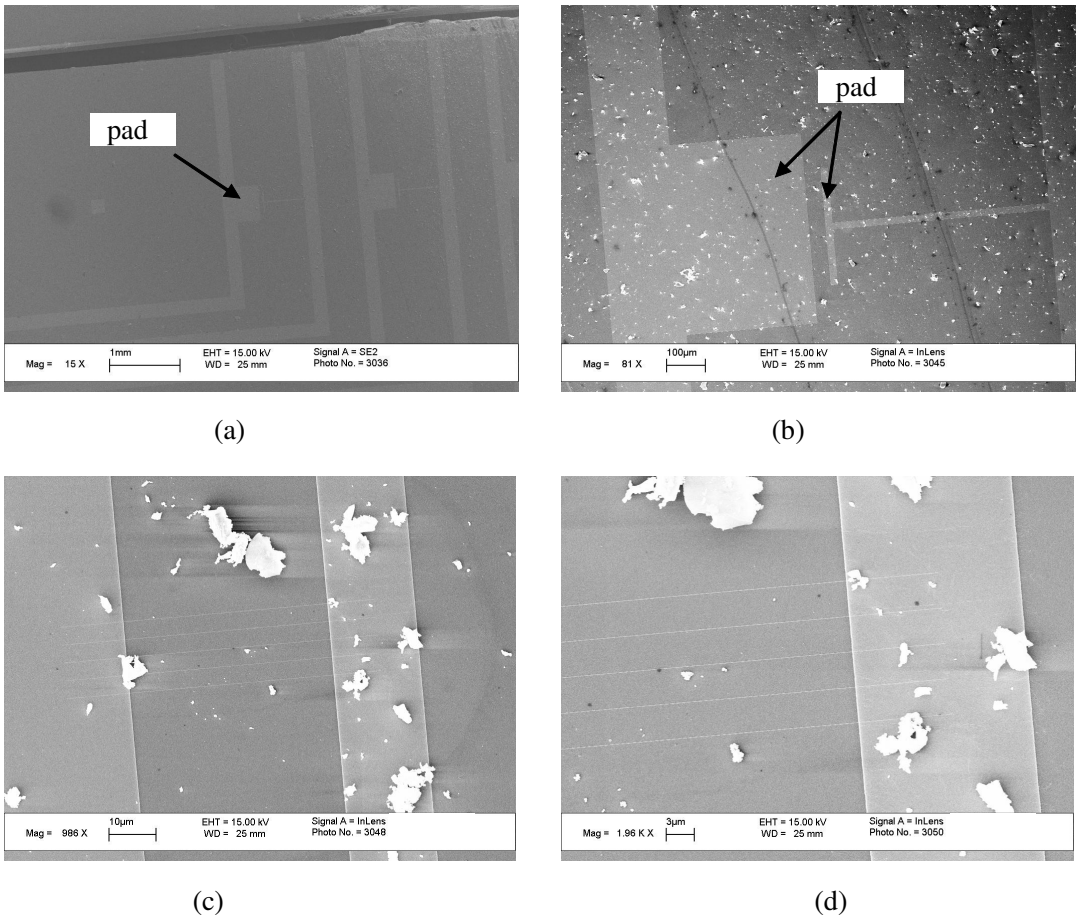

Figure 7.9 Nano metal traces between two large metal pads for electrical resistance characterization. Particles are from the dicing of the silicon substrate. (a)&(b): low magnification metal pad and nano metal traces, (c)&(d): high magnification metal pad and nano metal traces.

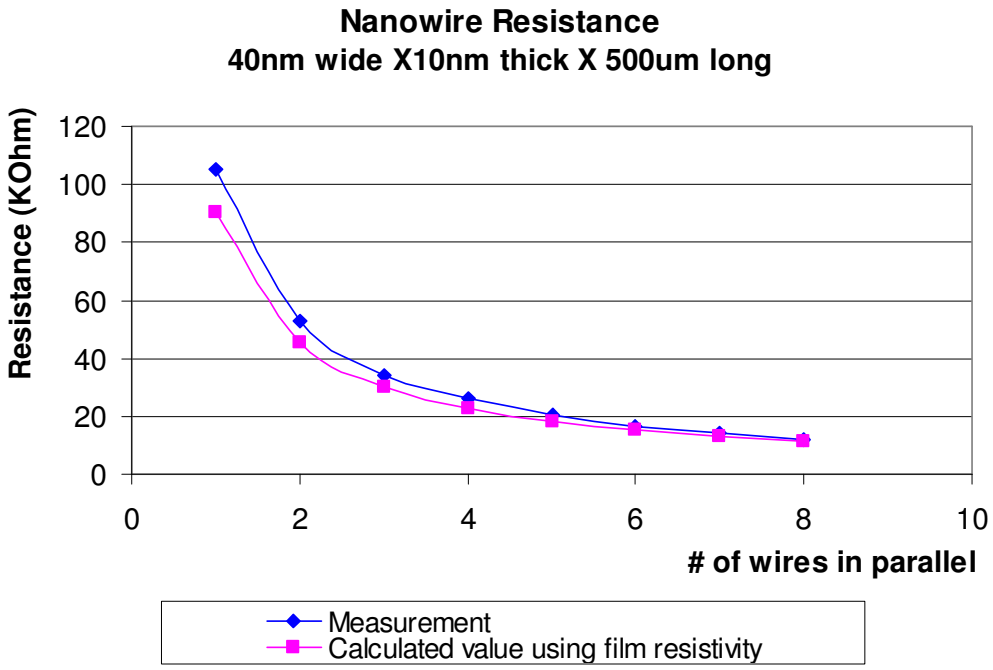

Figure 7.10 Electrical resistance comparisons between measurement and calculated value

It should be mentioned that the resistance of these traces is greater than the calculated resistance using bulk resistivity of Au and Ti. The reason is that the resistivity of nano scale traces is two to three times greater than their bulk resistivity. As mentioned earlier, the absolute resistance is not of concern in this work, rather the increase in resistance (as each of the resistors is broken during the fatigue interface crack propagation) is of interest in this work. As long as the electrical resistance of all nano metal traces is uniform, the relative resistance change of these nano metal trace array can be measured. Table 7.1 and Figure 7.10 show that the electrical resistance of the nano metal trace is very uniform. Therefore, these nano metal traces could be used for detection of the interfacial crack propagation.

Table 7.1 Resistance measurement of the nano metal traces

Test #	# of traces in parallel	Measured resistance (KΩ)	Expected resistance
1	1	105.1	R (single resistor)
2	2	52.9	Approximately equal to R/2
3	3	34.25	Approximately equal to R/3
4	4	26.05	…
5	5	20.37	…
6	6	16.48	…
7	7	14.12	…
8	8	12.11	Approximately equal to R/8

Table 7.2 Resistivity of 20nm thick Ti and Au film (unit: ohm-cm)

Measurement	#1	#2	#2	Average
Ti (20nm thick)	1.0822E-03	1.0821E-03	1.0819E-03	1.0821E-03
Au (20nm thick)	7.2840E-06	7.3063E-06	7.3091E-06	7.2998E-06

7.3 Micro Contact Magnetic Spring Fabrication and Characterization

7.3.1 Micro Contact Magnetic Spring Fabrication

Based on the process described in the last chapter, a micro contact spring structure was fabricated. Figure 7.11 shows an unreleased micro contact spring with a magnetic material at the tip region. Photolithography and etching were used for patterning the micro contact spring, probe pads, and the ferromagnetic region. The nano scale metal trace array is sandwiched between the micro contact spring and the substrate. Figure 7.12 shows the magnetic material could be in discrete shapes. Figure 7.12 shows that there is a lot of freedom to control the shape of the magnetic material, and therefore the force applied to the cantilever.

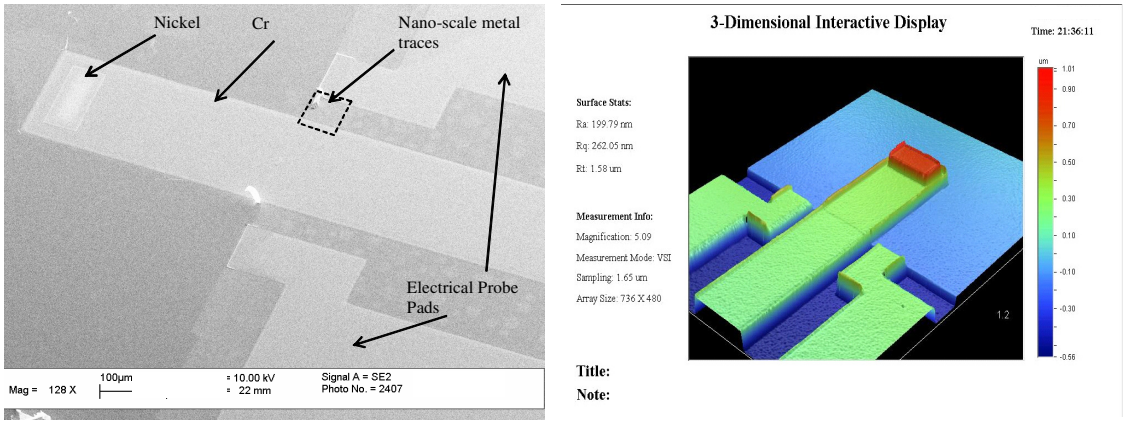

(a) (b)

Figure 7.11 (a) SEM image of Micro contact spring with ferromagnetic material deposited on the tip region, (b) 3D images taken by Wyko® profilometer

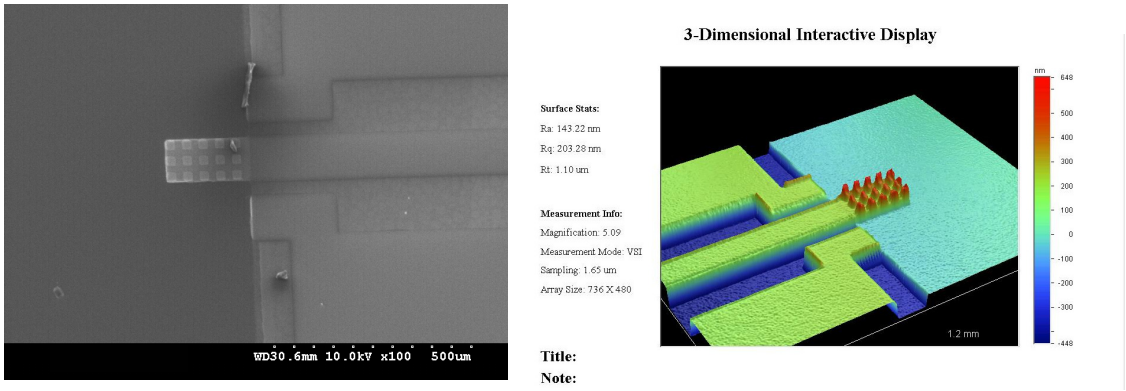

(a) (b)

Figure 7.12 (a) SEM image of Micro contact spring with ferromagnetic material deposited with discrete shapes, (b) 3D images taken by Wyko® profilometer

During the fabrication of the micro contact springs, the etching of the Si underneath the spring takes long time and eventually affected the interfacial integrity of the spring metal and the substrate. To eliminate this problem, the Si etching is avoided. SiO2, which is used for the purpose of Si etching, is no longer needed. The interface in the fatigue test is the same to the interfaces used in the monotonic test. To release the

spring, a superlayer used in the decohesion test is deposited on top of the cantilever. This superlayer will release the cantilever metal from the substrate and forms a free-standing structure as shown in Figure 7.13. Also shown in Figure 7.13 is the nano metal traces that superimposed by the metal pad and the unreleased portion of the micro contact spring. These nano metal traces are connected to another large metal pad, called test pad to enable the electrical resistance measurement of the nano metal trace array.

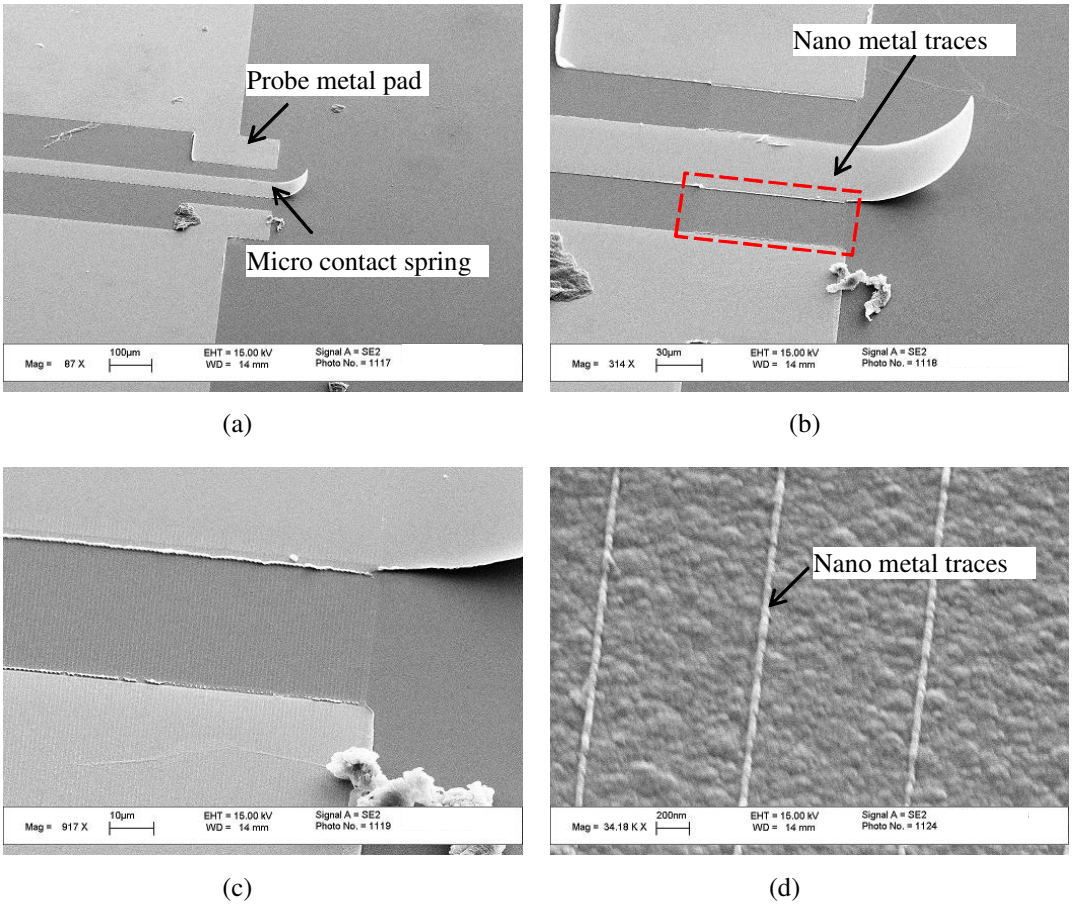

(a) (b)

(c) (d)

Figure 7.13 Released metal strips by using stressed superlayer deposited on top. (Nano metal traces are also fabricated). (a)&(b) released micro contact spring (low magnification), (c)&(d) high magnification of the nano metal traces.

In Figure 7.13, both sides of the metal strip are connected with nano trace arrays. The purpose of doing this is to try to measure the crack propagation along both sides of the metal strip. Figure 7.14 shows more of similar features but with different dimensions.

7.3.2 Micro Contact Spring Deflection Characterization

The purpose of the deflection characterization is to find out how much the cantilever deflects under certain load. In this study, the external load is applied by the magnetic field. Based on the deflection, the stress applied to the crack tip can be calculated as show in the last chapter. The characterization was done by using a Wyko® profilometer in the cleanroom. The Wyko® profilometer is essentially a white light interferometer which can measure surface heights up to 2mm with a resolution as small as 3nm. Figure 7.14 shows the image of a 20um wide and 40um long released metal strip by this profilometer.

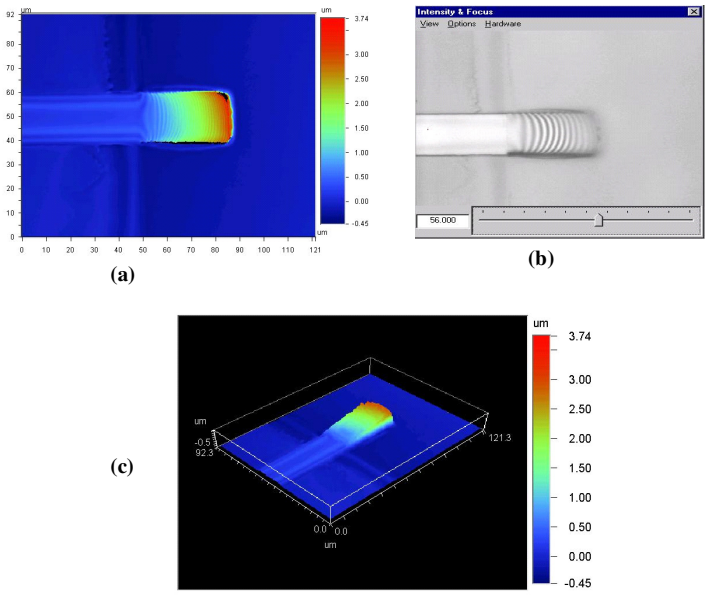

Figure 7.14 (a) 2D image of the released micro contact spring (b) screen capture of the fringes reflecting the height of the release strip, (c) 3D image of the released spring.

Figure 7.15 shows the schematic of this measurement. In Figure 7.15, the intensity of the magnetic field was changed by changing the current applied to the electromagnet. With the magnetic field changed, the deflection of the micro spring can be measured by the profilometer. The electronic magnet could either be on top of the micro contact spring or below the micro contact spring, generating a lifting or compression force to the springs.

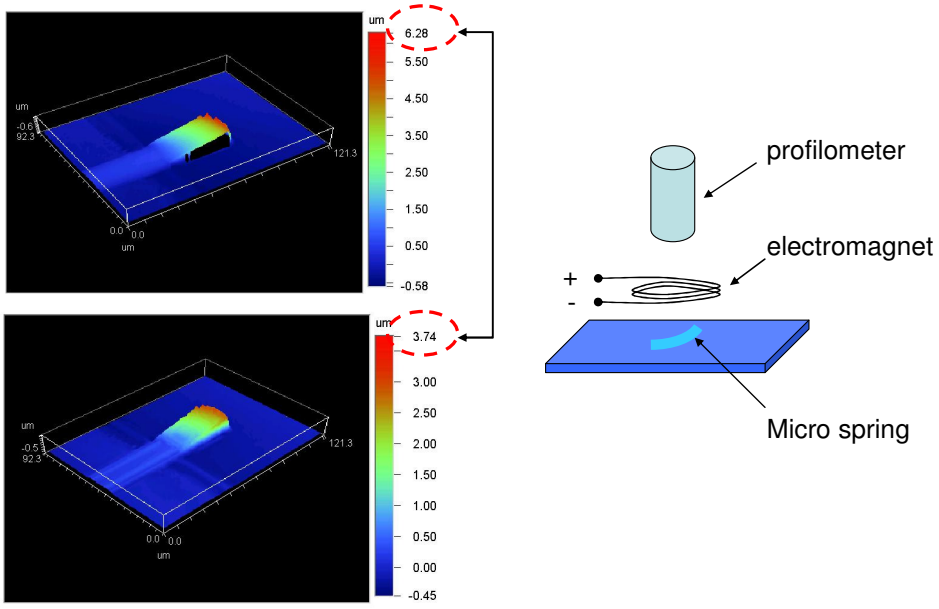

Figure 7.15 Deflection measurement with a Wyko® profilometer

To generate a strong magnetic field, a large current is needed to drive the magnet. Usually a function generator can not output a large current used for this purpose. A simple large current function generator is designed as shown in Figure 7.16. The input source is from a traditional function generator.

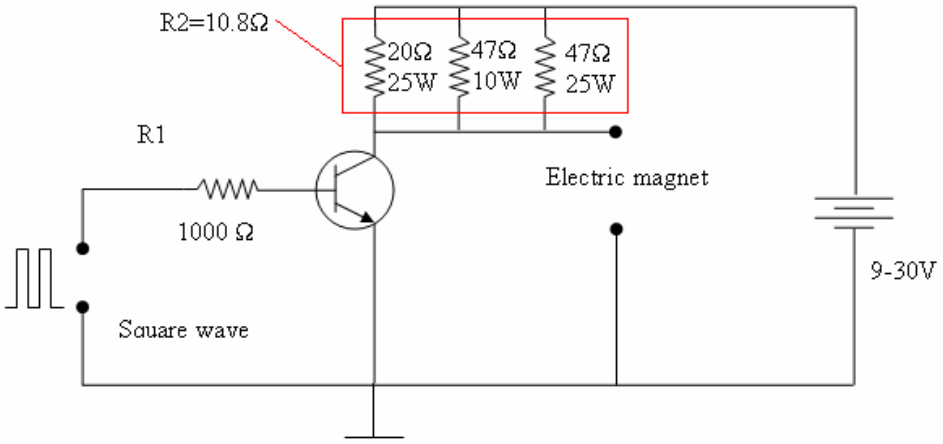

Figure 7.16 Circuitry used to drive the electric magnet.

Figure 7.17 shows the deflection of one micro spring as a function of applied current. It was shown that the deflection is proportional to the applied current. In this measurement the spring is 20um wide and 40um long.

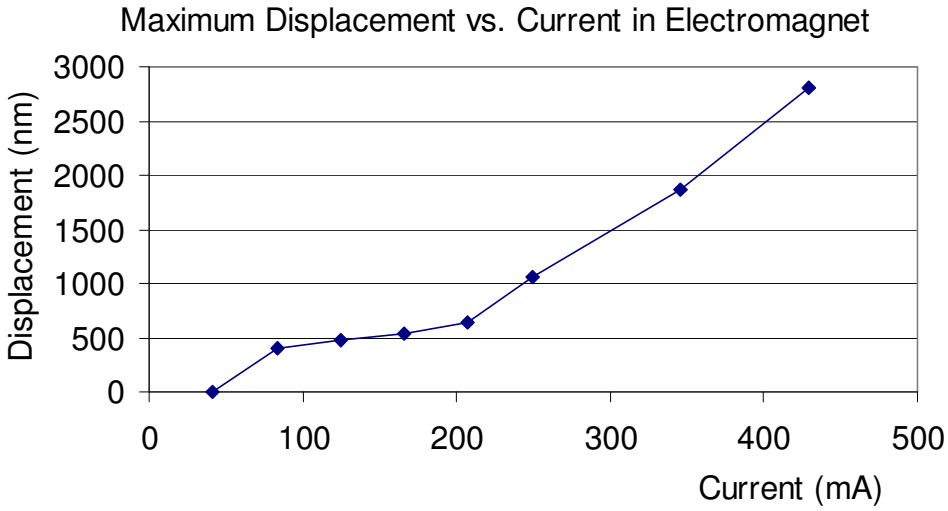

Figure 7.17 Spring deflection as a function of applied current in the electro magnet

7.4 Interfacial Fatigue Test

So far, the nano-wire and micro-spring were fabricated and characterized. The fatigue tests were then performed in the same way that the micro springs were characterized. The frequency of the magnetic field is fixed at 1 Hertz. The electrical resistance of the nano metal traces was measured with some DAQ system available in the CASPaR lab. The DAQ system was used for solder ball resistance measurement in other projects and was very reliable.

Figure 7.18 shows the resistance change of the nano metal trace array in one sample in which the loading frequency is 0.5Hz. The resistance is constant up to 12,000 cycles.

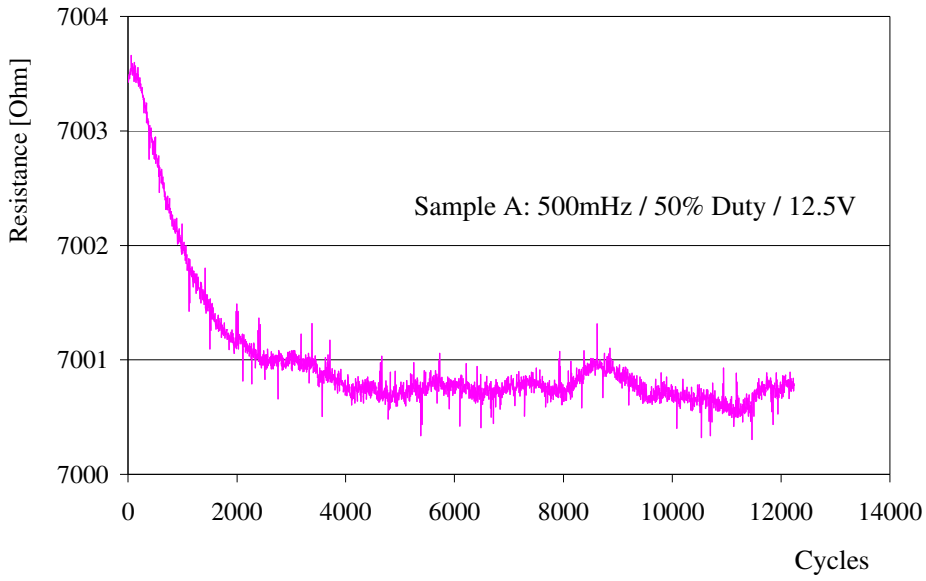

Figure 7.18 Electrical resistance changes versus number of cycle in loading

The samples were investigated and found out that the external loading does not delaminate the interface between the spring and the substrate, rather breaks the spring

itself. As shown in Figure 7.19, the micro spring was broken and the nano metal traces were kept intact. In this kind of material combination, the micro contact springs show very good interfacial integrity.

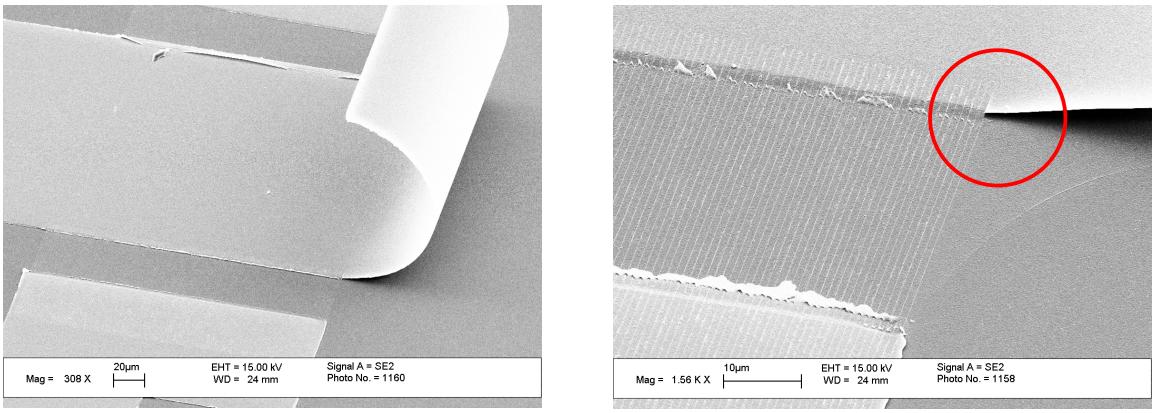

(a) (b)

Figure 7.19 Thin film cracking at the end of the micro spring

Figure 7.20 shows the resistance change of the nano metal trace array in another sample in which the loading frequency is 0.5Hz. The resistance is constant up to 270,000 cycles. Testing on other samples shows similar results.

Cannon et al. [59] did observe for metal/ceramic interfaces that the magnitude of the energy release rate to cause fatigue crack propagation (FCP) at the interface was approximately 6x less than the interfacial fracture toughness. Based on the results of the application of the SSDT to a Ti/Si interface, this means that the energy release rate required to propagate a crack along Ti/Si interface could be around 0.5 to 1 J/m^2.

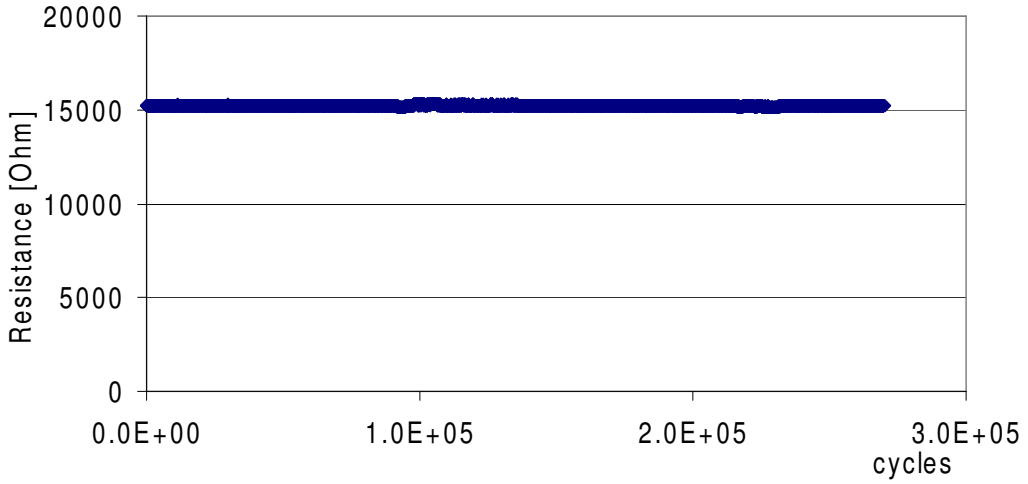

Figure 7.20 Electrical resistance changes versus number of cycles

Based on Equation 6.3, the magnitude of G for a given magnetic force P applied at the tip of the cantilever as

$$G = \frac{1}{B}\frac{3P\delta}{2L} = \frac{1}{B}\frac{9EI_z}{2L^4}\delta^2 = \frac{1}{B}\frac{L^2}{2EI_z}P^2 = \frac{3}{8}\frac{t^2}{L^4}\delta^2 \qquad (7.1)$$

Thicker and shorter springs (given the same displacement) will yield more energy release rate to drive interfacial delamination. While making the spring longer will significantly decreases the energy release.

The energy release rates for the spring tested were calculated in Table 7.3. Most of the values are much less than the G needed, suggesting that FCP would not occur in a Ti/Si interface given these loadings and geometries. In Table 7.3, the springs are compressed 100% percent, i.e., the spring was compressed to the substrate. If the springs were compressed partially, the energy release rate will be even smaller.

Most of the test cases yield an energy release rate too small to drive the fatigue crack propagation. From table 7.3, it does show that the energy release rate can be increased by increasing the thickness of the micro contact spring (case 4, 5, 6). While increasing the length of the length and the deflection do not necessarily help. This suggests that in future testing, the spring thickness should be increased in order to facilitate the interfacial fracture.

Table 7.3 Energy release rate for different cases

Case	L, length	T, thickness	Max. deflection, δ	Energy release rate, G
	um	um	um	J/m^2
1	40	0.2	10	0.033
2	40	0.2	20	0.131
3	80	0.2	40	0.033
4	40	0.3	10	0.101
5	40	0.4	10	0.262
6	40	0.5	10	0.511

Figure 7.21 shows some SEM images of different springs after the fatigue test. Again, there is very minor or no delamination along the interface.

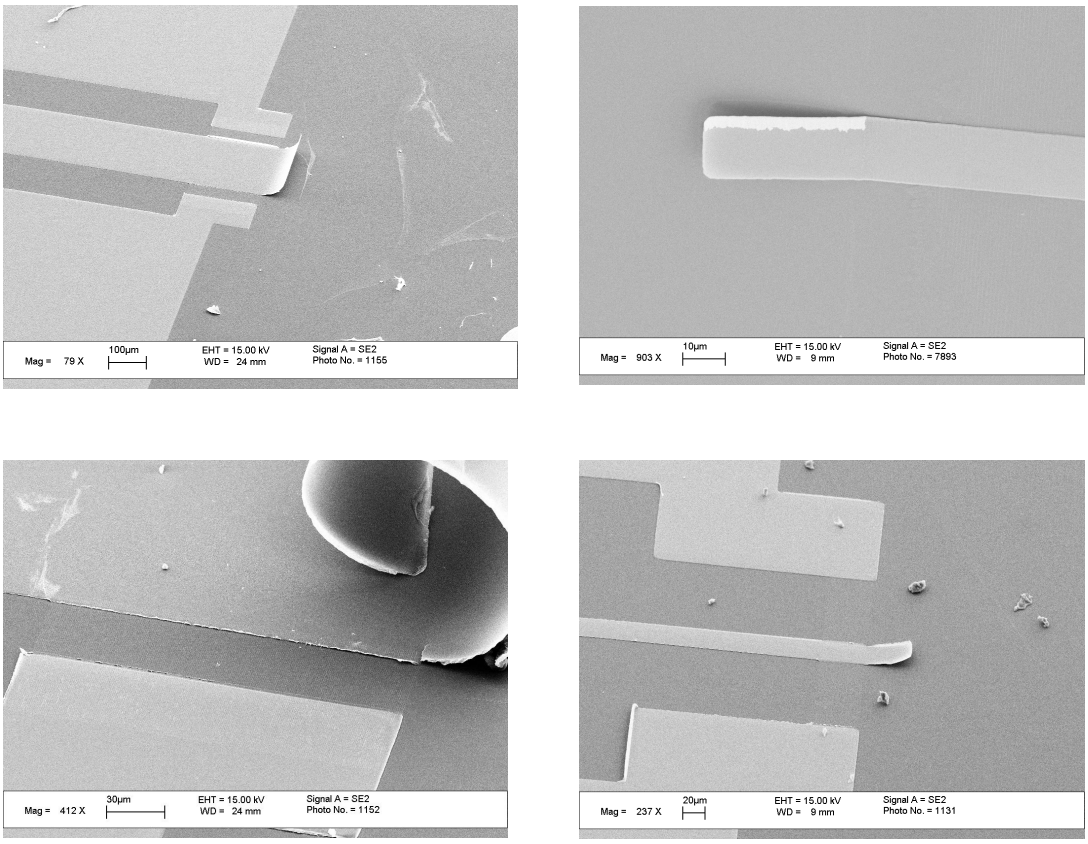

Figure 7.21 Different micro contact springs after the fatigue testing

7.5 Learning from the Interfacial Fatigue Test and Its Implication to the Application of Micro Contact Spring Techniques

Two major applications of micro-contact springs are wafer level probing and flip chip on board (FCOB) chip-to-next-level interconnection. Both applications expose the micro-contact springs to the same failure mechanism – cyclic fatigue. In this section, the observation of the interfacial fatigue test in this study will be correlated to these two applications.

7.5.1 Micro-contact springs in Wafer-level Probing

Semiconductors go through many testing processes during their production. One of such processes is the testing of circuits in chips, which is an extremely important process for ensuring the product performance and quality. This process also makes up a large portion of production cost. Wafer level probing is used to test the functionality and perform burn-in of dies on a wafer prior to packaging. The path for semiconductor manufacturers is to reduce the cost of burn-in by moving burn-in back to the wafer level and off the board. This approach becomes more cost effective, as at-speed testing becomes feasible at the wafer level.

Micro-contact spring based probe cards not only facilitate the wafer level probing capability but also enable the cost of creating micro-contact spring based probe cards. Inexpensive burn-in devices fabricated from micro-contact springs would reduce the cost of test, allow a more comprehensive verification of know good die (KGD), and ultimately reduce the cost of packaging through higher yields. Micro-contact spring probe cards contain arrays of released springs, where their release tip location interfaces the die pads of the die under testing.

7.5.2 Micro-contact Springs in Chip-to-next Level Packaging

Micro-contact springs as chip-to-next-level interconnects have the potential to enable the development of computer architectures with wider busses and to allow the design of chips with more flexible contact placement. Further, they allow higher frequency operation and lower cross talk by permitting signal lines to have adjacent ground lines in close proximity (PARC, MMS, and GIT, 1999).

The compliance of the micro-contact spring is the basis of its expected high reliability. To take full advantage of this capability is to create a package without the use of solder or underfill. This type of package is called a free-air package. Figure 7.22 shows a schematic of a free-air package. The package is formed by compressing released springs to some predetermined height. Then while under compression a compliant constraint is placed around the periphery of the package. Within the package is an inert environment where the micro-contact springs "slide" and compress during bending or compression of the package.

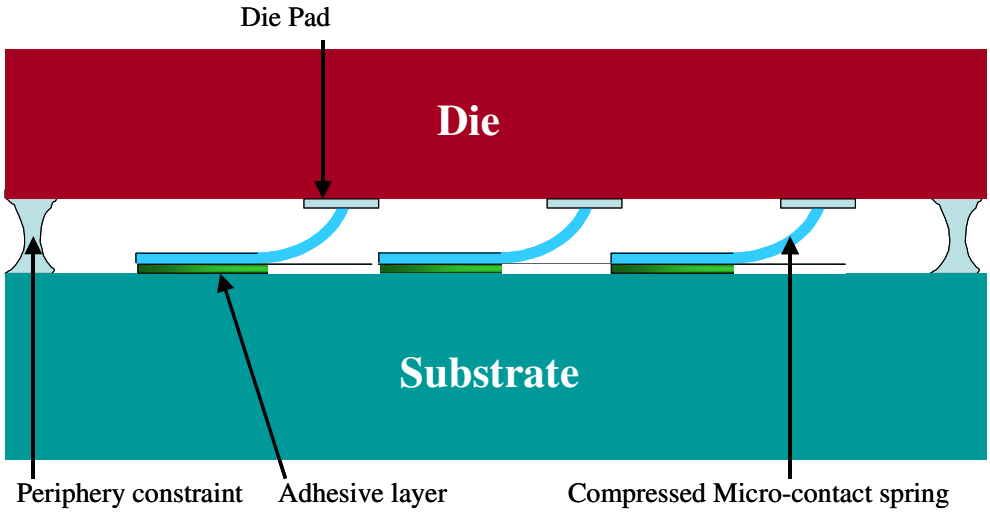

Figure 7.22 Schematic of a "Free-air" micro-contact spring package [91]

7.5.3 Cyclic Failure in Packaging and Probing

From the interfacial fatigue test, it can be learned that thin and long micro contact spring should survive more number of cycles than thick or short micro contact springs if interfacial fracture is the weakest link the whole structure. At the same time, thin and long micro contact springs generally have a high tendency to crack in the film itself than thick ones. Depending on the application, there exists an optimized thickness in the

micro contact spring that neither the interfacial failure nor the cohesive failure should come much earlier than the other.

Table 7.4 shows the energy release rate for long micro contact springs used in probing applications, in which the spring is about 0.5 to 1.5um thick. It shows that the length of the spring has a significant effect to the energy release rate of the spring. The longer the spring, the smaller the energy release rate. Even with a very large deflection of 50um for 1.5um thick spring, the energy release is about 0.5 J/m2. This indicates the micro contact spring with this dimension and deflection will have infinite life.

Table 7.4 Energy release rate for long springs

Case	L, length	T, thickness	Max. deflection, δ	Energy release rate, G
	um	um	um	J/m^2
1	40	0.2	10	0.033
2	200	0.2	10	0.0001
3	200	0.2	50	0.0013
4	200	0.5	50	0.0204
5	200	1	50	0.1635
6	200	1.5	50	0.5517

Ahmad [92-94] used a KLA-1007 wafer prober to cycle micro-contact springs through probing cycles. Resistance was monitored during the cycling to detect failures. Each probe card contains about 30 – 40 micro-springs. Contact was established between the springs and a bare 6-inch wafer plated with copper and aluminum. The failure

criterion is if the single spring resistance exceeded 1 Ω. Initially 80% of the springs failed due to cohesive fracture at the spring tip – this was due to a design flaw. Figure 7.23 shows the performance of the surviving springs. At approximately 69000 cycles a failure occurs – Ahmad reports this failure as a macroscopic failure under the spring. The remaining springs last past 100000 cycles. Ahmad's test indicates similar prediction based on the fatigue test.

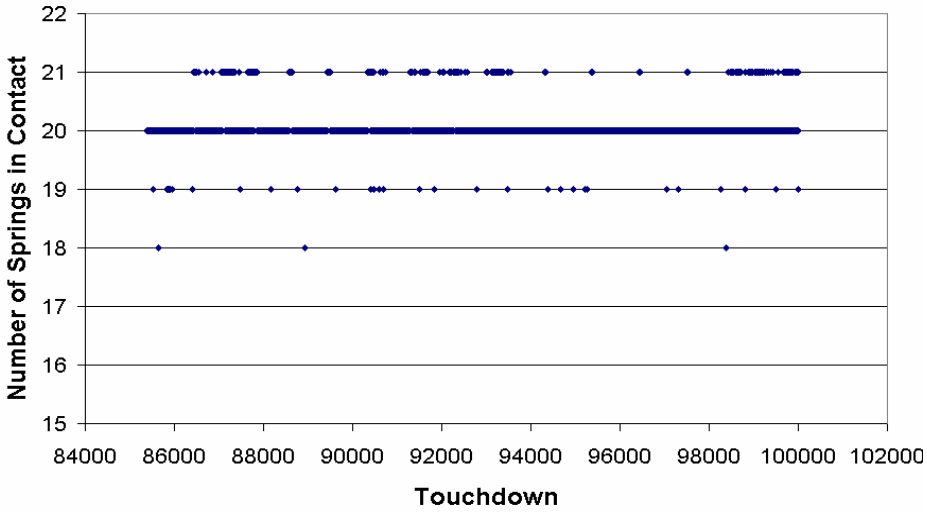

Figure 7.23 Number of springs in contact versus cycles (touchdowns)

CHAPTER 8

SUMMARY AND CONTRIBUTIONS

8.1 Summary

- The superlayer technique with release layer is a fixtureless test technique for measuring the interfacial fracture toughness of thin film structures. This technique has been demonstrated on Ti/Si interface.
- The Single Strip Decohesion Test (SSDT) developed in this study can capture a wide range of mode mixities by changing film thickness or the film stress. The test shows that the interfacial fracture toughness increases with mode mixity.
- The SSDT has been demonstrated for a wide range of release layer geometries.
- The SSDT is amenable to data reduction through analytical and numerical techniques
- For Ti/Si interfaces, the interface fracture toughness approaches the bonding energy between Ti and Si atoms when the mode mixity approaches zero. There is only minor inelastic deformation, if there is any, in the single strip decohesion test. The energy leverage for inelastic deformation is very small in SSDT.

- To have a successful delamination under monotonic load, the release layer in SSDT should be designed in a way that could force the delamination propagate perpendicular to the cut.
- In order for the delamination to propagate perpendicular to the cut, there must be some adhesion in the strip edge to constrain the force release. In this way, the delamination driving force will not be lost and the superlayer/interface layer would go perpendicular to the cut, in which an analytical solution can be easily obtained.
- The width of the thin film strip has negligible effect to the decohesion result. When the film strip width approaches to as narrow as 9um, the interfacial delamination driving force decreases sharply. This is not believed to be the limitation of the SSDT test since this width could be smaller with better lithography tool.
- In a successful decohesion test, the release layer should be as thin as possible, but should be thick enough to generate a continuous layer to cover the substrate. If the release layer is too thin, the superlayer/interface layer tends to delaminate along a step side wall due to the formation of the release layer.
- The Ti interface layer should be at least 100Å to have a good bonding between Ti/Si. Thin Ti does not necessary generate weak interface if the mode mixity of the Ti/Si interface is high.
- For the interfacial fatigue characterization, external magnetic actuation is demonstrated to study fatigue delamination.

- In the interfacial fatigue test, it was shown that Ti and Cr layers can withstand thousands of cycles without delamination. The test results have been applied to study the reliability of thin-film structures for probing and packaging applications
- Thickness and length in the micro contact spring have a significant effect to the interfacial reliability under cyclic loadings. Thin and long springs usually generate a smaller driving force for interfacial fracture than thick and short ones.

8.2 Contribution

- An innovative fixtureless superlayer based experimental technique was developed to measure interfacial fracture toughness of nano scale thin films used in micro contact spring technology. By using etchable release layers with varying width, the proposed method can measure interfacial fracture toughness using one strip. The proposed method is applicable to a wide range of mode mix and is repeatable. The data reduction is easy and the interface studied will reflect the actual interface with identical processing conditions.
- A fixtureless non-contact method for testing the interfacial crack propagation has been developed. The idea of monitoring interfacial crack propagation by nano metal traces was proposed and implemented. This can be used to study crack propagation in other applications. The idea of apply non-contact force to micro scale structure with sputter magnetic materials was proposed and implemented.

- Results from the interfacial fatigue test were used to study interfacial delamination of micro-contact thin film structures for probing and packaging applications

8.3 Future Work

- After the decohesion test was done and the sample was removed from the etchant, the delaminated film strip usually was pulled back to substrate by surface tension force of the water. So the thin film sticks back to the substrate and make the visual inspection difficult. Method to overcome this is to dip the samples in isopropyl and dry the sample in a Tousimis^{TM} super critical dryer which is available in the cleanroom.
- In the implementation of the interfacial fatigue test, a stronger or thicker cantilever structure is needed. Thicker magnetic material is needed to generate large bending force.
- Ferromagnetic material with different patterns can be deposited to the tip of the cantilever or micro springs to create combinations of pull/twist.
- The fatigue test can be applied on multiple material stacks to identify the weakest interface.
- Interfacial characterization in thermal/humidity chambers.

APPENDIX 4-1 DELAMINATED TEST STRIPS

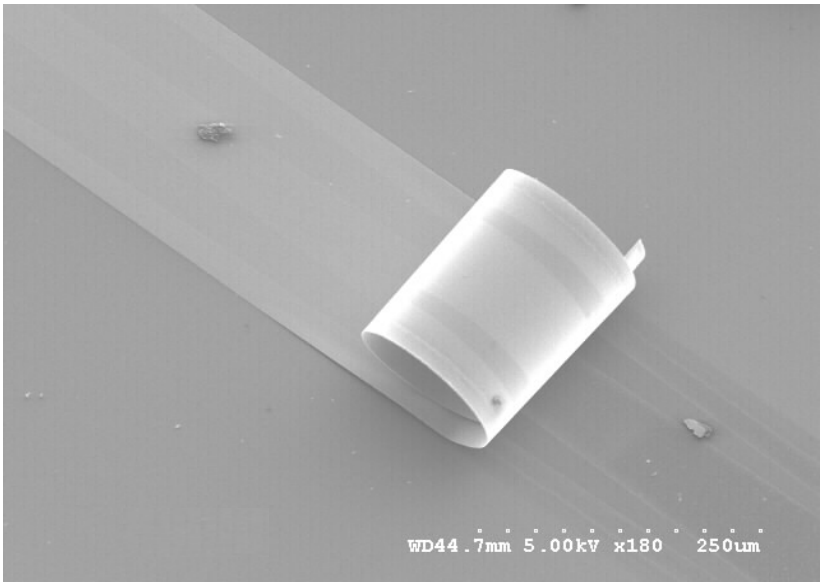

Figure A4-1 Delaminated thin film strip with two triangle release layer (half area)

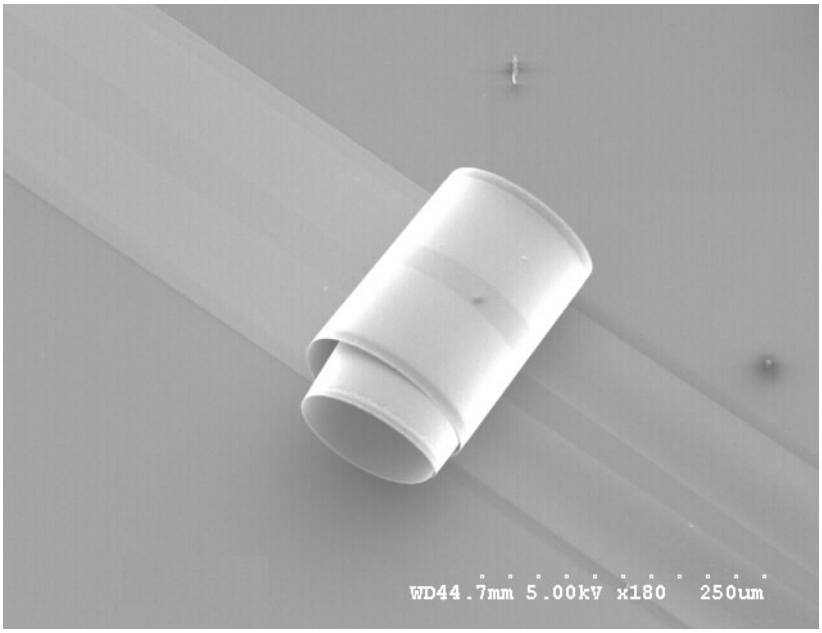

Figure A4-2 Delaminated strip with two triangle release layer

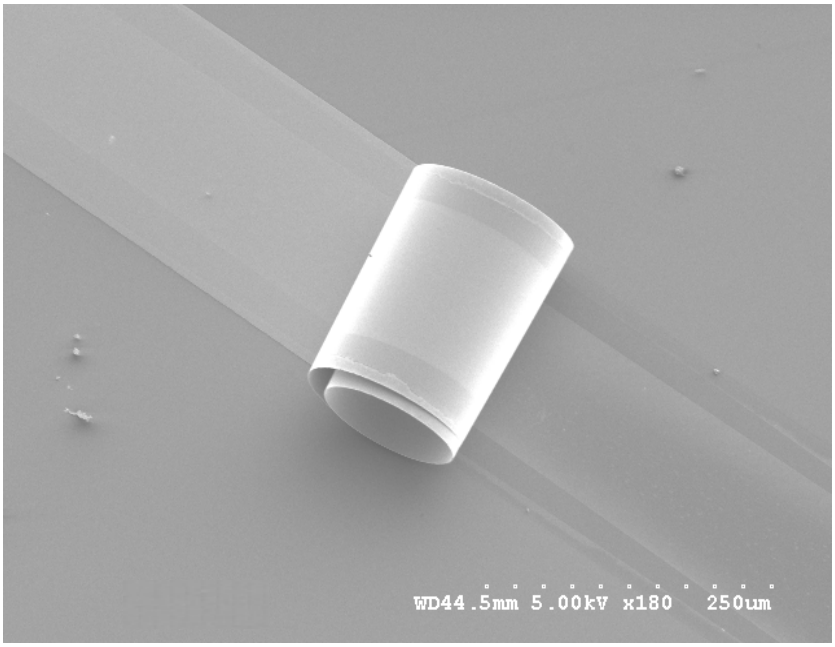

Figure A4-3 Delaminated strip with one triangle release layer (half area)

APPENDIX 4-2 DETAILED RECIPE FOR SINGLE STRIP DECOHESION TEST PROCESS

Stage 1: Pre-cleanroom Activities

1. Identify the materials that will be used for the Interface Layer and Super Layer
2. Use the Matlab program "modemixity_func.m" to determine the combination of the Interface Layer thickness and Super Layer thickness to give the desired mode mix and energy release rate.

Stage 2: Non-adhesive layer

For a titanium interface layer material, gold must be used as the non-adhesive layer since no material is known, which titanium does not adhere to.

1. Substrate Clean (standard clean):
    a) Spray with Trichloroethylene
    b) Spray with Acetone
    c) Spray with Isopropyl
    d) Rinse with DI water
    e) Bake at 110 C for 10 minutes or until wafers are completely dry
2. Deposit the release layer (Gold)
    a) Place the wafers in the Unifilm sputter chamber (if using >2 wafers, place them on planets 1, 3, and 5)
    b) Deposit Au using calibration file Au-DC1-3-A

c) The thickness of the Au layer depends on the thickness of interface layer – the Au thickness should be about 10x thinner than the interface layer.

d) Remove the wafers from the Unifilm – be careful to not scratch the surface since the gold is very thin and does not adhere strongly.

3. Substrate clean: standard clean

4. Spin photoresist, Shipley SU1813

a) Program setting: 500 RPM, 100 RPM/s, 5 seconds; 3000 RPM, 500 RPM/s, 45 seconds

b) Soft bake at 110 for 1 minute

5. Expose using MA-6 and release layer mask

a) Settings: Vacuum contact, 50 um gap, 9 second exposure, channel 2 (405 nm)

6. Develop using Microposit 319 (typically takes less than 1 minute)

a) Check under yellow light microscope to ensure that the photoresist has been developed (i.e., photoresist is removed from areas that were exposed).

b) Rinse under DI water

7. Hard bake for 5 minutes at 120 C

8. Let cool for 2 minutes

9. Prepare Au etchant solution

a) Using a deep acid-resistant tub (enough to hold one wafer)

b) Use Transene^{TM} Gold Etchant (iodine complex; potassium iodide)

c) Dilute approximately 100:1 with DI. The key here is to create a VERY dilute solution that attacks the gold very slowly.

d) Record the time to etch

10. Prepare water bath

a) Using a deep acid-resistant tub (enough to hold one wafer)

11. Etch wafers in Au etchant solution

a) Exact time is unknown – visually examine to see when features begin to clearly appear. Check under yellow light microscope to be sure process is complete.

12. Rinse in water bath. Rinsing under the DI tap may cause the features to peel off.

13. Remove SU1813 using Microposit™ 1165 Remover.

14. Rinse in water bath.

15. While wet bake at 110 C for 10 minutes

Stage 3: Interface Layer and Super Layer

1. Prepare stress calibration wafer

2. Pre profile: Take x and y profiles (KLA profilometer) on a clean bare wafer

3. Substrate clean all the wafers (Release layer ones and bare one) using a standard clean

4. Deposit the Interface Layer (titanium) and Super Layer (Chrome)

a) Place up to two wafers in the Unifilm sputter chamber (if using 2 wafers, place them on planets 1 and 3)

b) Place the stress calibration wafer on planet 5

c) Deposit Ti using calibration file Ti-DC1-5-D with a thickness hi and at a pressure of 3 mTorr (current calibration gives a stress of 0 MPa at this pressure)

d) Deposit Cr using calibration file Cr-DC1-4-E with a thickness of hs and at a pressure of 3 mTorr (current calibration gives a stress of 1540 MPa at this pressure)

e) Remove the wafers from the Unifilm

5. Substrate clean: standard clean

6. Post profile. Profile the stress calibration wafer as in step 3.2 and calculate the residual stress

7. Spin photoresist on wafers using Shipley SU1813

a) Program setting: 500 RPM, 100 RPM/s, 5 seconds; 3000 RPM, 500 RPM/s, 45 seconds

b) Soft bake at 110 for 1 minute

8. Expose using MA-6 and Interface Layer Mask

a) Settings: Vacuum contact, 50 um gap, 9 second exposure, channel 2 (405 nm)

9. Develop using Microposit 319 (typically takes less than 1 minute)

a) Check under yellow light microscope to ensure that the photoresist has been developed (i.e., photoresist is removed from areas that were exposed).

b) Rinse under DI water

10. Hard bake for 5 minutes at 120 C

11. Let cool for 2 minutes

12. Prepare Cr etch solution

    a) Using a deep acid-resistant tub (enough to hold one wafer)

    b) Use Chromium™ Photomask Etchant undiluted

    c) This etches at approximately 24 A/s

13. Prepare Ti etch solution

    a) Using a deep acid-resistant tub (enough to hold one wafer)

    b) Use Transene™ Titanium Etchant diluted 100:1 small dropper

14. Etch wafers in Cr etchant solution

    a) Time to etch is roughly based on 24 A/s. Wafer will turn black and then return to its normal color once the etch finishes

    b) Record the time to etch as tcr

15. Rinse under DI water and dry using a nitrogen gun

16. Etch wafers in Ti etchant solution

    a) Time to etch is roughly based about 2 minutes per 0.3 um. Wafer will turn black and then a white gas will come off locations where Ti is etched. When reaction finishes, Ti etch is finished

    b) Record the time to etch as tti

17. Rinse under DI water and dry using a nitrogen gun

18. Check under yellow light microscope to confirm etch is finished.

19. Remove SU1813 using Microposit 1165 Remover.

20. Rinse under DI water

21. While wet, bake at 110 C for 10 minutes

Stage 4: Crack Initiation

1. Substrate clean all the Interface/Super layer wafers (the stress calibration wafer may be put aside)
2. Spin photoresist on wafers using Shipley SU1813
    a) Program setting: 500 RPM, 100 RPM/s, 5 seconds; 3000 RPM, 500 RPM/s, 45 seconds
    b) Soft bake at 110 for 1 minute
3. Expose using MA-6 and Crack Initiation Mask
    a) Settings: Vacuum contact, 50 um gap, 9 second exposure, channel 2 (405 nm)
4. Develop using Microposit 319 (typically takes less than 1 minute)
    a) Check under yellow light microscope to ensure that the photoresist has been developed (i.e, photoresist is removed from areas that were exposed).
    b) Rinse under DI water
5. Hard bake for 5 minutes at 120 C
6. Let cool for 2 minutes
7. Dice the wafer into the 8 samples
8. Carefully wash each sample under DI water to remove debris during dicing
9. Prepare Cr etch solution
    a) Use a small, deep acid-resistant dish (enough for one sample)
    b) Use Chromium Photomask Etchant (available in the cleanroom for free) undiluted

c) This etches at approximately 24 A/s

10. Prepare Ti etch solution

    a) Use a small, deep acid-resistant dish (enough for one sample)

    b) Use Transene Titanium Etchant diluted 100:1 small dropper

11. Prepare Au etchant solution

    a) Use a small, deep acid-resistant dish (enough for one sample)

    b) Use Transene Gold Etchant (iodine complex; potassium iodide)

    c) Dilute approximately 100:1 with DI. This is a guess – the key here is to create a VERY dilute solution that attacks the gold very slowly.

12. Pour Microposit 1165 Remover into a small glass Petri dish

13. Etch wafers in Cr etchant solution for a time

14. Rinse under DI water and dry using a nitrogen gun

15. Etch wafers in Ti etchant solution for a time

16. Rinse under DI water and dry using a nitrogen gun

17. Etch wafers in Au etchant solution for a time

18. Rinse under DI water and dry using a nitrogen gun

19. Check under yellow light microscope to confirm etch is finished.

20. With glass dish with Microposit 1165 under a yellow light microscope, place the sample in the solution.

21. Wait for sometime as the resist is dissolved, observe any delamination that occurs.

22. Take microscope photographs of the delamination and record the results

23. Clean (either under very gentle DI water or in a DI water bath)

24. Bake sample at 110 for 10 minutes

25. Take SEM pictures of the delamination length and measure the curvature of the delaminate strips (if applicable)

Stage 5: Post Test Activities

1. Calculate the energy release rate

2. Average the G for all test strips.

APPENDIX 5-1 MPC USER SUBROUTINE

```
      SUBROUTINE MPC(UE,A,JDOF,MDOF,N,JTYPE,X,U,UINIT,MAXDOF,
     * LMPC,KSTEP,KINC,TIME,NT,NF,TEMP,FIELD,LTRAN,TRAN)
C
      INCLUDE 'ABA_PARAM.INC'
C
      DIMENSION UE(MDOF),A(MDOF,MDOF,N),JDOF(MDOF,N),X(6,N),
     * U(MAXDOF,N),UINIT(MAXDOF,N),TIME(2),TEMP(NT,N),
     * FIELD(NF,NT,N),LTRAN(N),TRAN(3,3,N)
C     INTRINSIC ABS,SQRT
      DOUBLE PRECISION NODEX, COMPX
C
      IF(JTYPE.EQ.1) THEN
                IF(KSTEP.LT.11) THEN
                        COMPX=(40.E-3)-(KSTEP-1)*0.5E-3
                ELSE
                        COMPX=(35.E-3)-(KSTEP-11)*0.5E-3
                ENDIF
C


                IF(X(1,2).GT.COMPX) THEN
                LMPC=0.
                ELSE
```

```
            UE(1)=U(1,2)
            UE(2)=U(2,2)
            UE(3)=U(3,2)
            A(1,1,1)=1.
            A(2,2,1)=1.
            A(3,3,1)=1.
            A(1,1,2)=-1.
            A(2,2,2)=-1.
            A(3,3,2)=-1.
            JDOF(1,1)=1
            JDOF(2,1)=2
            JDOF(3,1)=3
            JDOF(1,2)=1
            JDOF(2,2)=2
            JDOF(3,2)=3
        ENDIF
    ENDIF
        RETURN
    END
```

APPENDIX 5-2 CRACK IN A BILAYER

The theory for calculating the mode mixity is attached in this section. In this study, the analytical solution for calculating the mode mixity is based on this method.

Suo and Hutchinson [82] have presented a general solution for a crack between two elastic layers under a given edge loading. They use superposition to reduce the problem and the energy release rate is given in terms of force P and moment M (Figure A5-2).

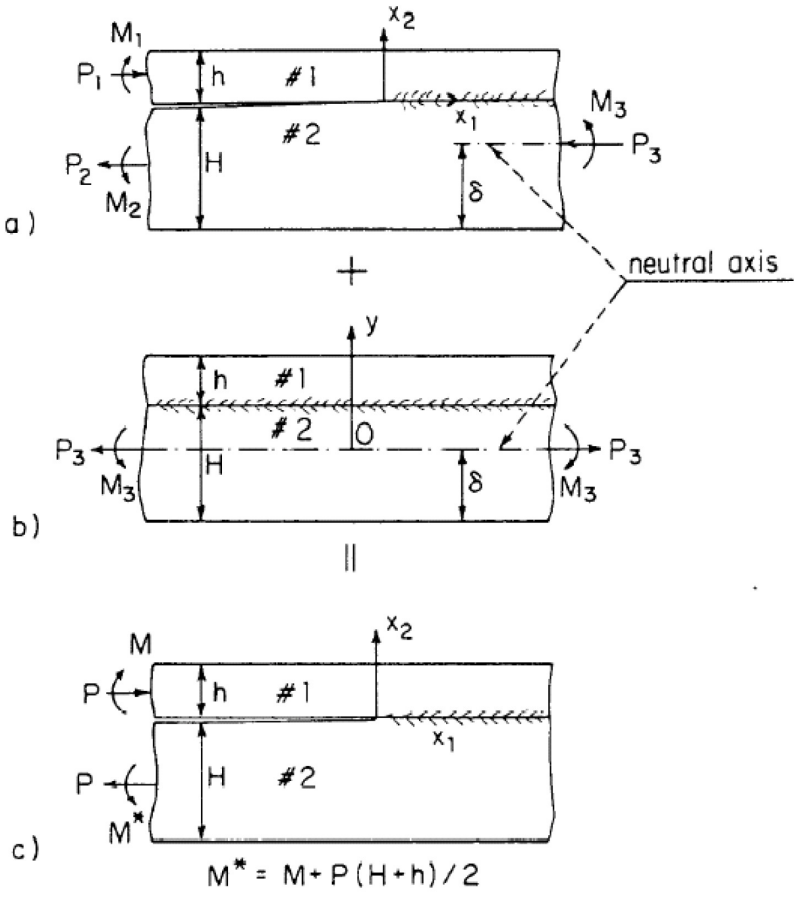

Figure A5-2 Crack between Two Elastic Layers – Superposition [82]

The case of the residually stressed thin film on a substrate is exactly equivalent to the following load combinations shown in Figure A5-2.1a.

$$P_1 = P_3 = \sigma^T h$$

$$M_3 = \sigma^T h\left(H - \delta + \frac{h}{2} \right)$$

$$M_1 = 0$$

Therefore,

$$P = \sigma^T h\left[1 - C_1 - C_2\left(\frac{1}{\eta} - \Delta + \frac{1}{2} \right) \right]$$

$$M = -\sigma^T h^2 C_3\left(\frac{1}{\eta} - \Delta + \frac{1}{2} \right)$$

Where

$\sigma^T = \dfrac{8\Delta\alpha\Delta T}{C_1}$ is the misfit stress between the two layers

$\Delta\alpha$ is the difference in CTE between the two layers

ΔT is the uniform temperature change

$$C_1 = \frac{\Sigma}{A_0}$$

$$C_2 = \frac{\Sigma}{I_0}\left(\frac{1}{\eta} - \Delta + \frac{1}{2} \right)$$

$$C3 = \frac{\Sigma}{12 I_0}$$

$$A_0 = \frac{1}{\eta} + \Sigma$$

$$I_0 = \frac{1}{3}\left\{\Sigma\left[3\left(\Delta - \frac{1}{\eta}\right)^2 - 3\left(\Delta - \frac{1}{\eta}\right) + 1\right] + 3\frac{\Delta}{\eta}\left(\Delta - \frac{1}{\eta}\right) + \frac{1}{\eta^3}\right\}$$

$$\frac{\delta}{h} = \Delta = \frac{1 + 2\Sigma\eta + \Sigma\eta^2}{2\eta(1 + \Sigma\eta)}$$

$$\Sigma = \frac{1+\alpha}{1-\alpha}$$

$$\eta = \frac{h}{H}$$

h = thickness of the thin film

H = thickness of the substrate

Dundurs' numbers are:

$$\alpha = \frac{\Gamma(\kappa_2 + 1) - (\kappa_1 + 1)}{\Gamma(\kappa_2 + 1) + (\kappa_1 + 1)}$$

$$\beta = \frac{\Gamma(\kappa_2 - 1) - (\kappa_1 - 1)}{\Gamma(\kappa_2 + 1) + (\kappa_1 + 1)}$$

The oscillation index is

$$\varepsilon = \frac{1}{2\pi}\ln\frac{1-\beta}{1+\beta}$$

$$c_1 = \frac{\kappa_1 + 1}{\mu_1}$$

$$c_2 = \frac{\kappa_2 + 1}{\mu_2}$$

$$\Gamma = \frac{\mu_1}{\mu_2}$$

$\kappa_i = 3 - 4\upsilon_i$ for plane strain

$\kappa_i = \frac{3-\upsilon_i}{1+\upsilon_i}$ for plane stress

μ_i and ν_i are the shear modulus and Poisson's ratio of the respective layers.

The energy release rate can be computed by taking the difference of the energy stored in the structure far ahead and far behind the crack tip.

$$G_{ERR} = \frac{c_1}{16}\left[\frac{P^2}{Ah} + \frac{M^2}{Ih^3} + 2\frac{PM}{h^2\sqrt{AI}}\sin\gamma\right]$$

where

$$A = \frac{1}{1+\Sigma\left(4\eta + 6\eta^2 + 3\eta^3\right)}$$

$$I = \frac{1}{12\left(1+\Sigma\eta^3\right)}$$

and $\sin\gamma = 6\Sigma\eta^2)(1+\eta)\sqrt{AI}$

The mode mixity is given by

$$\psi = \tan^{-1}\left[\frac{\lambda\sin\omega - \cos(\omega+\lambda)}{\lambda\cos\omega - \sin(\omega+\lambda)}\right]$$

where $\lambda = \frac{Ph}{M}\sqrt{\frac{I}{A}}$

and ω is a function of α, β and η

Suo and Hutchinson have published values of ω for various combination of α, β and η. In all the cases encountered, ω varied between 55° and -53°.

APPENDIX 6-1 DETAILED RECIPE AND PROCESS FOR INTERFACIAL FATIGUE TEST

Stage 1: Nano metal traces fabrication

1. The nano metal traces can be fabricated on a bare silicon wafer or on a wafer coated with SiO2, in which the Unaxis PECVD^{TM} is needed.
2. Use Unaxis PECVD^{TM} to deposit a thin layer of SiO_2. The recipe is called "std_ox.prc", a standard program to deposit a uniform layer of SiO_2. It takes about 17 minutes to deposit 1um SiO2. In this test, 1um SiO_2 is sufficient to protect Si.
3. Chose the resist of ZEP520A for the Nanolithography patterning. The spin speed is 6000RPM and ramp rate is 1000RPM. The spin time is 60 seconds.
4. Expose ZEP520A using EBL and develop according to the recipes and procedure in Appendix 6-2.
5. Use the E-beam evaporation tool to deposit Cr for 25nm @ 1A/s (depending on the composition of the nano metal traces, the metal could be Cr, Au or Ti or the combination of Cr/Au or Ti/Au.
6. Acetone lift-off.
7. Ultrasonic for 10 minutes with Microposit 1165 Remover
8. Use DI wafer to clean the wafers and use N2 to dry them.
9. Oven dehydration for 3 minutes at 110C.

Stage 2: Release region deposition

10. In this step, the region used to release the micro contact spring is fabricated. Use photo resist of AZ5214. AZ5214 is negative when after flood exposure. Spin AZ5214 at 1000RPM with 250RPM ramp rate for 10 seconds, 3000RPM with 500RPM ramp rate, for 40 seconds.
11. Alignment with Karl Suss TSA MA6 Mask Aligner. The alignment marker on the wafer is very faint. It might be difficult to find the marker. In that case, focus first.
12. Exposure with channel I, use hard contact, 20um gap, 27 seconds at 5mW/cm^2, (total ~135mJ). Sometimes the exposure does should be verified or measured first.
13. Post back 1.5min at 115C. Cool down to room temperature before flood exposure on the mask aligner.
14. Use DI wafer to clean the wafers and use N2 to dry them.
15. Flood exposure. This step is critical to transform the positive resist of AZ5214 to become a negative photo resist. Use Channel 1 for 2 min. First to put no mask on the mask holder. When first come to the machine, leave the mask holder aside, click Enter (to toggle vacuum), then click “Change Mask”, and then hit “Enter” again, you may go back and forth until neither “Enter” nor “Change Mask” flashes. Put the wafer on the stage, and click “Lamp Test”, located on the upper right panel). When done, use oven dehydration for 3 minutes at 110C.
16. Develop AZ5214 using AZ400K developer. AZ400K should first be diluted with water (AZ400K: H2O = 1:4). The developing time is 40-60 seconds. You

can see the release layer change during developing. Over develop 20 more seconds to fully clean the target region.

17. DI water rinsing, use N2 gun to dry.
18. Hard baking in oven, 2 minutes at 120C.
19. E-beam evaporation, 10nm Ti/30nm Au at 1A/S for both.
20. Acetone lift-off, put in Acetone for a few minutes, then put in ultrasonic bath until the photoresist is gone.
21. DI wafer, N2, 3-5 minutes in oven at 110C

Stage 3: Micro-contact spring deposition and release

22. Use a negative photoresist (NR9-8000P) to fabricate the micro contact springs. The spinning details are 1000RPM at 250RPM ramp rate for 10 seconds, and then 5000RPM at 500RPM ramp rate, for 50 seconds. Since the NR9-8000P is very viscous, a high spinning speed is needed. Use tape to secure the textwipe because of the high spinning speed.
23. Post baking for 5 minutes at 110C.
24. Alignment with MA6 mask aligner.
25. Expose with Channel-I, hard contact, 20um gap, 30 seconds at 5mW/cm^2, (total about 150mJ).
26. Post back 3 min at 75C. This post baking is critical for this negative photo resist.
27. Always use clean RD6 developer for developing. After developing, pour the RD6 into sink. Use new RD6 for the second wafer, otherwise the developing time will be far way off from the known time. It could be as long as 3 minutes.

28. Always use clean RD6 developer for developing. After developing, pour the RD6 into sink. Use new RD6 for the second wafer, otherwise the developing time will be far way off from the known time. It could be as long as 3 minutes.
29. Develop using RD6, the developing time is about 20-60 seconds. Real time varies based on the amount of RD6 in the container. Observe the pattern evolution to determine the correct time. Over develop it for about 20 seconds. Under-development is bad for later lift-off. Metal will peel off if residue is left. Over-development for 20 seconds is beneficial.
30. DI water rinsing, and use N2 to dry the pattern.
31. Hard baking in oven for 2 minutes at 110C.
32. Use Unifilm Sputterer to deposit the spring metal. The procedure is the same to the fabrication procedure used in the monotonic thin film testing.
32. After the deposition of metal, use Acetone to lift-off the clean the photo resist.
33. Put in directly gold etchant (diluted by H_2O, about 1:20 = Au etchant: H_2O) to release the springs.
34. Dip the sample into a container with DI water to remove the Acetone. Don't use DI to rinse the wafer otherwise the springs would be damaged. And transfer the wafer carefully to a container with Alcohol (IPA, Methanol, or Ethanol).
35. Use the Tousimis™ Supercritical Dryer to dry the samples. Carefully and quickly transfer the wafer(s) from the wafer container into the dryer process chamber. For best results, minimize any exposure time to air. Use the Supercritical dryer is important. This will eliminate any damage due to surface

tension of the DI water or fluid flowing to the micro contact springs during the conventional drying process.

Stage 4: Micro contact spring calibration

36. Use Wyko™ profilometer to calibrate the deflection of the micro contact spring. The procedure is discussed in Chapter 6.

Stage 5: Micro contact spring fatigue test

37. Use date acquisition system to perform the test.

APPENDIX 7-1 JOB DECK AND SCHEDULE FILE USED IN E-BEAM LITHOGRAPHY

The instructions which determine how the pattern is applied to a wafer or other writing substrate, is determined by two files: the Job Deck file (.jdf) and the Schedule file (.sdf).

The job deck file and the schedule file are attached here. The detailed explanations of the commands, please see check the equipment manual.

The job deck file used to pattern the nano metal traces is:

```
;-----------------------------------------------------
 JOB/W  'JZHENG',4          ; piece cassette
;-----------------------------------------------------
        PATH DEVIN
              ARRAY   ( -35000,2,40000 )/( 36000,2,40000 )
                        ASSIGN  P(1) -> ((*,*),SHOT1))
              AEND
;-----------------------layer 0
        PEND


;-----------------------------------------------------

;       Layer Definition

;-----------------------------------------------------

        LAYER   1

        P( 1 )  'jzheng.v30'

        SPPRM 4.0,,,,1.0,1

        STDCUR  2; current is 2nA


SHOT1: MODULAT ((0,0),(1,100),(2,300),(3,500),(4,700),(5,1500),
-(6,2000),(7,2500),(8,3000)


END
```

Schedule file used in patterning the nano metal traces is:

```
**************************************************
MAGAZIN 'JZHENG'
#1
%4A
JDF 'JZHENG',1
ACC 100
CALPRM '100kv_100pa_jeol'
DEFMODE2
RESIST 200
SHOT,A2
OFFSET (0,0)
END 1
****************************************
```

REFERENCES

1. Fork, D., et al., *Stress engineered metal interconnects.* Proceedings 2001 HD International Conference on High-Density Interconnect and System s Packaging, 2001. **4428**: p. 195-200.

2. Volinsky, A.A., J.B. Vella, and W.W. Gerberich, *Fracture toughness, adhesion and mechanical properties of low-K dielectric thin films measured by nanoindentation.* Thin Solid Films, 2003. **429**(1-2): p. 201.

3. Pocius, A.V., *Adhesion and adhesives technology: An introduction*. 1997, New York: Hanser.

4. Lane, M., *Interface fracture.* Annual Review of Materials Research, 2003. **33**: p. 29.

5. Furuya, A., N. Hosoi, and Y. Ohshita, *Evaluation of Cu adhesive energy on barrier metals by means of contact-angle measurement.* J. Appl. Phys., 1995. **78**(10): p. 5989.

6. Lipkina, D.M., D.R. Clarke, and A.G. Evans, *Effect of interfacial carbon on adhesion and toughness of gold–sapphire interfaces.* Acta Materialia, 1998. **46**(13): p. 4835-4850.

7. Gennes, P.G.d., *Wetting: statics and dynamics.* Rev. Mod. Phys., 1985. **57**: p. 827 - 863.

8. Lee, C.-Y. and K.-L. Lin, *Wetting kinetics and the interfacial interaction behavior between electroless Ni-Cu-P and molten solder.* Japanese Journal of Applied Physics, Part 1: Regular Papers & Short Notes & Review Papers, 1994. **33**(5A): p. 2684-2688.

9. Reimanis, I.E., et al., *Effects of plasticity on the crack propagation resistance of a metal/ceramic interface.* Acta Metallurgica et Materialia, 1990. **38**(12): p. 2645-2652.

10. Reimanis, J.E., B.J. Dalgleish, and A.G. Evans, *Fracture resistance of a model metal/ceramic interface.* Acta Metallurgica et Materialia, 1991. **39**(12): p. 3133.

11. Evans, A.G., et al., *Fracture energy of bimaterial interfaces.* Metallurgical Transactions A (Physical Metallurgy and Materials Science), 1990. **21A**(9): p. 2419.

12. Jokl, M.L., V. Vitek, and C.J. McMahon, Jr., *Microscopic theory of brittle fracture in deformable solids: a relation between ideal work to fracture and plastic work.* Acta Metallurgica, 1980. **28**(11): p. 1479-1488.

13. Wang, J.S. and Z. Suo, *Experimental determination of interfacial toughness curves using Brazil-nut-sandwiches.* Acta Metallurgica, 1990. **38**(7): p. 1279.

14. Cao, H.C. and A.G. Evans, *Experimental study of the fracture resistance of bimaterial interfaces.* Mechanics of Materials, 1989. **7**(4): p. 295.

15. Hutchinson, J.W. and Z. Suo, *Mixed Mode Cracking in Layered Materials.* Advances in Applied Mechanics, 1992. **29**: p. 63-191.

16. Liechti, K.M. and Y.S. Chai, *Asymmetric shielding in interfacial fracture under inplane shear.* J. Appl. Mech., 1992. **59**: p. 295–304.

17. Williams, M.L., *The stresses around a fault or crack in dissimilar media.* Bulletin of the Seismological Society of America, 1959. **49**: p. 199-204.

18. Dundurs, J., *Edge-bonded Dissimilar Orthogonal Elastic Wedges.* Journal of Applied Mechanics Reviews, 1969. **36**: p. 650-652.

19. Charalambides, M., et al., *On the Analysis of Mixed-Mode Fracture.* International Journal of Fracture, 1992. **54**: p. 269-291.

20. Rice, J.R., *Elastic fracture mechanics concepts for interfacial cracks.* Journal of Applied Mechanics, Transactions ASME, 1988. **55**(1): p. 98.

21. Sih, G.C. and J.R. Rice, *Bending of plates of dissimilar materials with cracks.* American Society of Mechanical Engineers -- Transactions -- Journal of Applied Mechanics, 1964. **31**(3): p. 477.

22. Shih, C.F., *Cracks on Bimaterial Interfaces: Elasticity and Plasticity Aspects.* Materials Science and Engineering, 1991. **A143**: p. 77-90.

23. Hutchinson, J.W., M.E. Mear, and J.R. Rice, *Crack Paralleling an Interface Between Dissimilar Materials.* Journal of Applied Mechanics, Transactions ASME, 1987. **54**(4): p. 828.

24. Malyshev, B.M. and R.L. Salganik, *The Strength of Adhesive Joints Using the Theory of Cracks.* International Journal of Fracture, 1984. **26**(4): p. 261.

25. Akisanya, A.R. and N.A. Fleck, *Edge cracking and decohesion of thin films.* International Journal of Solids and Structures, 1994. **31**(23): p. 3175.

26. Akisanya, A.R. and N.A. Fleck, *Interfacial cracking from the free-edge of a long bi-material strip.* International Journal of Solids and Structures, 1997. **34**(13): p. 1645.

27. Evans, A.G. and J.W. Hutchinson, *Effects of non-planarity on the mixed mode fracture resistance of bimaterial interfaces.* Acta Metallurgica, 1989. **37**(3): p. 909.

28. Hu, M.S. and A.G. Evans, *Cracking and decohesion of thin films on ductile substrates.* Acta Metallurgica, 1989. **37**(3): p. 917.

29. Thouless, M.D., *Fracture mechanics for thin-film adhesion.* IBM Journal of Research and Development, 1994. **38**(4): p. 367.

30. Thouless, M.D., *Some mechanics for the adhesion of thin films.* Thin Solid Films, 1989. **181**: p. 397.

31. Bagchi, A., et al., *A New procedure for measuring the decohesion energy for thin ductile film on substrates.* Journal of Materials Research, 1994. **9**(7): p. 1734-1741.

32. Bagchi, A. and A.G. Evans, *Measurement of the debonded energy for thin metallization lines on dielectrics.* Thin Solid Films, 1996. **286**: p. 203-212.

33. Kinbara, A., et al., *Evaluation of adhesion strength of Ti films on Si(100) by the internal stress method.* Thin Solid Films, 1998. **317**(1-2): p. 165-168.

34. Zhuk, A.V., A.G. Evans, and J.W. Hutchinson, *The adhesion energy between polymer thin films and self-assembled monoloayers.* J. Mater.Sci., 1998. **13**: p. 3555-3564.

35. Xu, G., M.Y. He, and D.R. Clarke, *Effect of moisture on the fracture energy of TiN/SiO2 interfaces in multi-layer thin films.* Acta Materialia, 1999. **47**(15-16): p. 4131-4141.

36. Lacombe, R., *Adhesion Measurement Methods: Theory and Practice*. 2006: CRC Press.

37. Farris, R.J. and J.L. Goldfarb, *Experimental partitioning of the mechanical energy expended during peel testing.* Journal of Adhesion Science and Technology, 1993. **7**(8 pt 1): p. 853-868.

38. Sickfeld, J., *Pull-Off Test, an Internationally Standardized Method for Adhesion. Testing-Assessment of the Relevance of Test Results*, in *Adhesion Aspects of Polymeric Coatings*, K.L. Mittal, Editor. 1983, Plenum Press: New York p. 543.

39. Drory, M.D. and J.W. Hutchinson, *Measurement of the adhesion of a brittle film on a ductile substrate by indentation.* Proceedings of the Royal Society of London, Series A (Mathematical, Physical and Engineering Sciences), 1996. **452**(1953): p. 2319-41.

40. Evans, A.G. and J.W. Hutchinson, *On the mechanics of delamination and spalling in compressed films.* International Journal of Solids and Structures, 1984. **20**(5): p. 455-66.

41. Kriese, M.D., N.R. Moody, and W.W. Gerberich. *Adhesion assessment of copper thin films*. 1997. San Francisco, CA, USA: MRS, Warrendale, PA, USA.

42. Marshall, D.B. and A.G. Evans, *Measurement of adherence of residually stressed thin films by indentation. I. Mechanics of interface delamination.* Journal of Applied Physics, 1984. **56**(10): p. 2632-8.

43. Rosenfeld, L.G., et al., *Use of the microindentation technique for determining interfacial fracture energy.* Journal of Applied Physics, 1990. **67**(7): p. 3291-6.

44. Tsui, T.Y. and Y.-C. Joo, *Measuring thin film fracture toughness using the indentation sinking-in effect and focused ion beam.* Materials Research Society Symposium - Proceedings, 2000. **594**: p. 389.

45. Tsui, T.Y., C.A. Ross, and G.M. Pharr. *Effects of adhesion on the measurement of thin film mechanical properties by nanoindentation*. 1997. San Francisco, CA, USA: MRS, Warrendale, PA, USA.

46. Boer, M.P.D. and W.W. Gerberich, *Microwedge indentation of the thin film fine line—I. Mechanics.* Acta Materialia, 1996. **44**(8): p. 3169-3175.

47. Boer, M.P.D. and W.W. Gerberich, *Microwedge indentation of the thin film fine line—II. Experiment.* Acta Materialia, 1996. **44**(8): p. 3177-3187.

48. Volinsky, A.A., N.R. Moody, and W.W. Gerberich, *Interfacial toughness measurements for thin films on substrates.* Acta Materialia, 2002. **50**(3): p. 441.

49. Dannenberg, H., *Measurement of Adhesion by a Blister Method.* J. Appl. Polym. Sci., 1961. **5**(14): p. 125-134.

50. Lai, Y.H. and D.A. Dillard, *A study of the fracture efficiency parameter of. blister tests for films and coatings*, in *Adhesion measuremnet of Films and Coatings*, K.L. Mittal, Editor. 1995: Utrecht, the Netherlands. p. 231.

51. Allen, M.G. and S.D. Senturia. *Microfabricated Structures for the Measurement of Adhesion and Mechanical Properties of Polymer of Polymer Films*. 1987. Denver, CO, USA: ACS, Washington, DC, USA.

52. Allen, M.G. and S.D. Senturia. *Aspects of adhesion measurement of thin polyimide films*. 1988. Ellenville, NY, USA: Publ by Soc of Plastics Engineers, Brookfield Center, CT, USA.

53. Dillard, D.A. and Y. Bao, *The Peninsula Blister Test: A High and Constant Strain Energy Release Rate Fracture Specimen for Adhesives.* The Journal of Adhesion, 1991. **32**: p. 253 – 271.

54. Charalambides, P.G., et al., *A test specimen for determining the fracture resistance of bimaterial interfaces.* Journal of Applied Mechanics, Transactions ASME, 1989. **56**(1): p. 77.

55. Ma, Q., et al. *Quantitative measurement of interface fracture energy in multi-layer thin film structures*. 1995. San Francisco, CA, USA: Materials Research Society, Pittsburgh, PA, USA.

56. Kanninen, M.F., *An Augmented Double Cantilever Beam Model for Studying Crack Propagation and Arrest.* International Journal of Fracture, 1973. **9**: p. 83-92.

57. Dauskardt, R.H., et al., *Adhesion and Debonding of Multi-Layer Thin Film Structures.* Engineering Fracture Mechanics, 1998. **61**(1): p. 141-162.

58. Modi, M.B. and S.K. Sitaraman, *Interfacial fracture toughness measurement for thin film interfaces.* Engineering Fracture Mechanics, 2004. **71**(9-10): p. 1219.

59. Cannon, R.M., et al., *Cyclic fatigue-crack propagation along ceramic/metal interfaces.* Acta Metallurgica et Materialia, 1991. **39**(9): p. 2145.

60. Gaudette, F.G., S. Suresh, and A.G. Evans, *Effects of sulfur on the fatigue and fracture resistance of interfaces between gamma-Ni(Cr) and alpha-Al2O3.* Metallurgical and Materials Transactions A: Physical Metallurgy and Materials Science, 2000. **31**(8): p. 1977.

61. McNaney, J.M., R.M. Cannon, and R.O. Ritchie, *Fracture and fatigue-crack growth along aluminum-alumina interfaces.* Acta Materialia, 1996. **44**(12): p. 4713.

62. Shaw, M.C., et al., *Fatigue crack growth and stress redistribution at interfaces.* Acta Metallurgica et Materialia, 1994. **42**(12): p. 4091.

63. Ritter, J.E., W. Grayeski, and T.J. Lardner, *Cyclic fatigue - crack growth along polymer/glass interfaces.* Polymer Engineering and Science, 1996. **36**(18): p. 2382.

64. Ritter, J.E., et al., *Fatigue crack propagation at polymer adhesive interfaces.* Journal of Adhesion, 1997. **63**(4): p. 265.

65. Yao, D. and J.K. Shang, *Effect of cooling rate on interfacial fatigue-crack growth in Sn-Pb solder joints.* IEEE Transactions on Components, Packaging, and Manufacturing Technology Part B: Advanced Packaging, 1996. **19**(1): p. 154.

66. Yao, D., Z. Zhang, and J.K. Shang. *Experimental technique for studying mixed-mode crack growth in solder joints*. 1995. San Francisco, CA, USA: ASME, New York, NY, USA.

67. Curley, A.J., et al., *Fatigue and durability behaviour of automotive adhesives. Part III: Predicting the service life.* Journal of Adhesion, 1998. **66**(1-4): p. 39.

68. Dessureault, M. and J.K. Spelt, *Observations of fatigue crack initiation and propagation in an epoxy adhesive.* International Journal of Adhesion and Adhesives, 1997. **17**(3): p. 183.

69. Guzek, J., H. Azimi, and S. Suresh, *Fatigue crack propagation along polymer-metal interfaces in microelectronic packages.* IEEE Transactions on Components, Packaging, and Manufacturing Technology Part A, 1997. **20**(4): p. 496.

70. Kook, S.Y., et al., *Adhesion and reliability of polymer/inorganic interfaces.* Journal of Electronic Packaging, Transactions of the ASME, 1998. **120**(4): p. 328.

71. Xie, W., H. Hu, and S.K. Sitaraman. *Determining interfacial delamination propagation of ViaLux [trademark] 81/ copper interface in multelayered System-On-Package (SOP) integrated substrates*. 2001. Kauai, Hi, United States: American Society of Mechanical Engineers.

72. Zhang, Z. and J.K. Shang, *Subcritical crack growth at bimaterial interfaces: Part III. Shear-enhanced fatigue crack growth resistance at polymer/metal interface.* Metallurgical and Materials Transactions A: Physical Metallurgy and Materials Science, 1996. **27A**(1): p. 221.

73. Shang, J.K. *Interfacial Fatigue-Crack Growth in Layered Materials*. in *Proc. 6th Int. Fatigue Congr.* 1996. Berlin, Germany.

74. Yao, D. and J.K. Shang. *Effect of load-mix on fatigue crack growth in Sn-Pb solder joint*. 1995. San Francisco, CA, USA: ASME, New York, NY, USA.

75. Yeon, S.-C., et al. *Measurement of micro-tensile properties for hard coating material TIN*. 2004. Jeju Island, South Korea: Trans Tech Publications Ltd, Zurich-Ueticon, CH-8707, Switzerland.

76. Hoffman, D.W. and J.A. Thornton, *Internal stresses in Cr, Mo, Ta, and Pt films deposited by sputtering from a planar magnetron source* Journal of Vacuum Science and Technology B: Microelectronics and Nanometer Structures, 1981. **20**(3): p. 355-358.

77. Windischmann, H., *Intrinsic stress in sputter-deposited thin films.* Critical Reviews in Solid State & Materials Sciences, 1992. **17**(6): p. 547.

78. Stoney, G., *The Tension of Metallic Films Deposited by Electrolysis.* Proceedings of the Royal Society of London, 1909(A 82): p. 172-175.

79. Cannon, R.M., et al., *Microstructural and Chemical Components of Ceramic-Metal Interfacial Fracture Energies.* Mat. Res. Soc. Symp., 1986. **72**: p. 121-126.

80. Pearson, R.A. and T.B. Lloyd, *On Relating Thermodynamic Work of Adhesion to Interfacial Fracture Toughness.* Material Research Society Symposium Proceedings, 1997. **445**: p. 247-257.

81. Modi, M., *Fracture in stress engineered, high density, thin film interconnects*, in *The Woodruff School of Mechanical Engineering*. 1992, Georgia Insitute of Technology: Atlanta, USA.

82. Suo, Z. and J.W. Hutchinson, *Interface crack between two elastic layers.* International Journal of Fracture, 1990. **43**(1): p. 1-18.

83. Matos, P.P.L., et al., *Method for calculating stress intensities in bimaterial fracture.* International Journal of Fracture, 1989. **40**(4): p. 235.

84. Hutchinson, J.W., *Delamination of compressed films on curved substrates.* Journal of the Mechanics and Physics of Solids, 2001. **49**: p. 1847-1864.

85. Madou, M., *Fundamentals of Microfabrication*. 1997, Boca Raton, FL: CRC Press.

86. Xie, W. and S.K. Sitaraman, *Investigation of Interfacial Delamination of a Copper-Epoxy Interface under Monotonic and Cyclic Loading: Experimental Characterization.* IEEE Transactions on Advanced Packaging, 2003. **26**(4): p. 447-452.

87. Cheng, Z., et al., *Underfill delamination analysis of flip chip on low cost board.* Proceedings of the International Electronic Materials and Packaging, 2001: p. 280-285.

88. Gurumurthy, C.K., et al., *A thermo-mechanical approach for fatigue testing of polymer bimaterial interfaces.* Transactions of the ASME. Journal of Electronic Packaging, 1998. **120**(4): p. 372-378.

89. Nagarajan, K. and R.H. Dauskardt, *Adhesion and reliability of underfill/substrate interfaces in flipchip BGA packages: metrology and characterization.* 7th Annual 2002 Proceedings. Pan Pacific Microelectronics Symposium, , 2002: p. 251-259.

90. Xie, W. and S.K. Sitaraman, *Investigation of Interfacial Delamination of a Copper-Epoxy Interface under Monotonic and Cyclic Loading: Modeling and Evaluation.* IEEE Transactions on Advanced Packaging, 2003. **26**(4): p. 441-446.

91. Ma, L., et al. *Compliant cantilevered spring interconnects for flip-chip packaging*. 2001. Orlando, FL: Institute of Electrical and Electronics Engineers Inc.

92. Ahmad, M. and S.K. Sitaraman. *Contact Modeling of Flexible Micro-Spring Interconnects for High Performance Probing*. 2001. Kauai, Hi, United States: American Society of Mechanical Engineers.

93. Ahmad, M. and S.K. Sitaraman, *Study of Mechanical Behavior of Compliant Micro-Springs for Next Generation Probing Applications.* Journal of Electronic Packaging, Transactions of the ASME, 2002. **124**(4): p. 411.

94. Ahmad, M. and S.K. Sitaraman, *Study of coupled thermal electric behavior of compliant micro-spring interconnects for next generation probing applications.* IEEE Transactions on Components and Packaging Technologies, 2003. **26**(2): p. 407.

VITA

Jiantao Zheng was born in Shandong, China in 1973. He received his Bachelor Degree in Mechanical Engineering with honors from Tsinghua University, Beijing, China in 1997. He also has a minor Bachelor Degree in Industrial Engineering from Tsinghua. In 2000, he was granted his Master Degree in Management Science and Engineering from Tsinghua University. He subsequently moved to Atlanta, Georgia to pursue his Doctor Degree in Mechanical Engineering in Georgia Institute of Technology. He worked as a Graduate Research Assistant for several projects, including MEMS/sensor fabrication and characterization, thin film interfacial delamination, micro and nano scale structure design and characterization. In 2005, he interned at Intel in Chandler, Arizona for 6 months. In 2006, He started to work full time for IBM in the area of mechanical testing and modeling for organic packaging. He is currently a Staff Engineer in the Systems and Technology Division of IBM in East Fishkill, New York.